Università degli Studi di Napoli Federico II

Facoltà di Ingegneria

Dipartimento di Ingegneria dei
Materiali e della Produzione

Dottorato di ricerca in

Ingegneria dei Materiali e delle Strutture

XXI° ciclo

Transport in nanomaterials: from macroscopic permeability studies towards single molecule evidence

Coordinatore
PROF. D. ACIERNO

Candidata
ILARIA DE SANTO

Tutor
PROF. P.A. NETTI

ANNO ACCADEMICO 2007 - 2008

Transport in nanomaterials: from macroscopic permeability studies towards single molecule evidence

Thesis outline

CHAPTER 1

Introduction

Nanomaterials are receiving an increasing scientific and technological interest lately. The boost of nanotechnology driven by the discovering of carbon nanotubes and their numerous applications has focused many efforts in the development of nanodevices and in the exploiting of their properties. The possibility to apply techniques primarily related to the semiconductors industry not only to the development of electronic chips but to nanomaterials devoted to the life science has generated a world of applications for such new nanomaterials, just to name a few, single molecule sequencing, drug delivery devices, biosensors, macromolecule separation devices[1]. The unique property in these materials is the presence of organizational features on the spatial scale of 1 to 300 nm. The presence of pores or channels on the nanomentric range allows a diverse interaction between molecules and material walls or surfaces which has been demonstrated to have interesting features. In fact, whenever the size of the device matches with molecule's dimensions or anyway, probe dimensions, generally a deviation from all classic relationships occurs. This happens because the material can interact with the molecule itself, single molecules or few molecules, giving rise to a discrepancy with the continuum behaviors. This has been shown in many cases.

For example in micro/nanofluidic there is a break down of the continuum assumption whenever the length scale of the flow field becomes close to the size of the molecules of the liquid. For instance the intrinsic viscosity dramatically changes from its typical values when the size of the channel and the size of the flowing molecule become comparable. It was shown that when the channel size is smaller than ten molecular diameters the fluid looses its fluid-like structure and behaves like a ordered solid crystal rearranging into a discrete number of ordered layers[2], with an apparent viscosity as high as 10^5 times the regular one, and a molecular timescale 10^{10} times slower than typical.[3] Couple of years later a rich pattern of heterogeneous molecular mobility in a confined thin layer of fluid was

demonstrated, which discarded the hypothesis of solidification induced by confinement[4]. Anyway an increase in viscosity was also shown for water during nanochannels filling, where channel height is several times higher than water dimension[5].

In another field of applications, the ability of nanomaterials to interact with molecules opened up the possibility to manipulate macromolecules such as DNA to perform DNA separation and sequencing and the performance of such devices is related to the conformation of the polymer in response to collisions or field gradients. A macromolecules confined in a channel with characteristic dimensions of the same order or less than the radius of gyration of the molecule was demonstrated to have an equilibrium configuration which is diverse from the bulk one and depends on the size of confinement[6-7]. Therefore conformational features are affected by confinement. On the other hand also dynamical properties strictly depend on geometrical confinement The influence of confinement on macromolecules relaxation was shown for instance in linear force extension experiments of the entropic recoil of DNA in slit confinement[8-9]. As a result of the competition between a stretching rate and the polymer relaxation, the deformation of the polymer affects the ability of the devices to properly sequence macromolecules. A confined relaxing chain was best described by two time constants in linear extension regime, whereas a bulk recoiling molecule is described by only a single time constant. The onset of a second recoiling regime was attributed to the presence of boundaries which prevent at a certain point a further extent in the blob size across the chain.

Among dynamic properties, transport properties of molecules, in terms of diffusivity are indeed affected by confinement. Fick's laws for diffusion were demonstrated to fail in many experimental cases. Though usually adequate to describe mass exchange within a thin membrane, in the case of size proximity of membrane's pore and molecule's diameter a non-Fickian behavior was demonstrated[10-11]. Micromachined membranes with rectangular pores nanometric only in one direction, and as small as 7 nm, were used for the controlled release of therapeutic drugs such as Interferon, BSA and Lysozyme. The possibility to use nanotechnology to manufacture such a devise with this kind of topological features was initially investigated with the aim to isolate pancreatic islet cells, and reduce the immune response. The membranes were designed in this way to accomplish the exchange route between the islet cells and the external environment, as to allow small molecules and nutrients (water, carbon dioxide and glucose) to permeate the membrane whereas preventing the bigger molecules derived from an immune response such as immunoglobulin from getting in[12-13]. In fact the advantages of nonoporous

materials include, for example, the possibility to vary the pore size and to ‘‘finetune’’ the material for certain drug molecules by chemical modification of the surface. Nanomaterials have many interesting properties considering drug delivery applications. The small size of the pores (2–50 nm) confines the space of a drug and engages the effects of surface interactions of the drug molecules and the pore wall. Depending on the size and the surface chemistry of the pores, increased dissolution rate or sustained release of a drug can be obtained[14]. Experimental diffusion studies showed for the reported nanomaterials an increasing deviation from Fick’s law in the release profile with the increasing in the ratio molecule size to membrane height. Such a deviation eventually corresponded to a zero order release kinetic, meaning that mass flux within the pore was constant for a certain extant.

Which is the reason why such a deviation might occur has not been clarified yet. Of course if a molecule is confined in a molecular small 3D cage its mean square displacement can be as high as the cage dimension. Therefore interesting is to investigate how and why 1D or 2D confinements induce deviation from Brownian motion. The presence of obstacles that obstructs molecular motion by an excluded volume interaction was demonstrated to cause anomalous diffusion which is factorized as an exponent smaller than one (one in the case of normal diffusion) that stretches the time dependence of the mean square displacement [15]. Anomalous diffusion was shown in intracellular diffusion motion, in diffusion in zeolites and in mesoporous materials. The limit of 1D confinement on the other hand, corresponds theoretically to the single file diffusion mechanism where no mutual passage of particles is possible. In this case at long times the mean square displacement is proportional to the square root of time[16-18].

Being concerned about the application of nanomaterials to the development of drug delivery devices, it is therefore of fundamental importance the understanding of how the nanostructure might change drug molecule diffusion properties within the device.

In this thesis work we wanted to address this topic with the aim to investigate how confinement may affect molecular diffusion properties. Attempts of doing so have been performed mainly on a macroscopic scale. While a macroscopic observation can give readily engineering information about the material in use, it can not unravel the microscopic dynamics. For this reason we developed our work starting from macroscopic permeability observations of hindered diffusion in nanoporous silicon membranes and diverged our experimental efforts to the investigation of single molecule behavior under confinement.

Willing to investigate molecular physical properties on the nanoscale, there is the need to overcome the drawback of nano dimensions, therefore classical microscopy can not be used. Though nanoscopy has already been proved, it is still somehow not affordable [19-20]. A possibility to study the nanoscale is to perform Fluorescence Correlation Spectroscopy (FCS), a well established technique widely used for measuring macromolecules properties and interactions both in vitro and in vivo; it measures fluorescence intensity fluctuations due to Brownian motion of few fluorochrome molecules in an illuminated volume smaller then a femtonliter. Through a time correlation analysis of the intensity fluctuations, molecular hydrodynamic properties of single molecules are then accessible [21]. Though usually applied to bulk measurements or to cellular environment investigations [22-23], it has also been used as a tool for velocity measurements in microfluidics and recently it has been demonstrated as a detection tool for molecular motion in micrometric and submicrometric structures [24-26]. We conducted FCS measurements of small molecules such as dyes, Dextrans or PEGs in glass nanoslits as small as 10 nm in height.

Starting from single molecule observations we also wanted to develop a mesoscopic dynamic model using Dissipative Particle Dynamics (DPD). The molecular model once validated could be used to predict the macroscopic behavior in terms of physically meaningful parameters that represent the actual dynamics of the system at a nanoscopic level, becoming a meaningful tool to the design of nanodevices for drug delivery applications.

References

1. Han J., Craighead H.G." Separation of long DNA molecules in microfabricated entropic trap array", *Science*, **288**,1026 (2000)
2. Israelachvili, J. N., "Intermolecular and surfaces forces" *Academic Press*, (1992)
3. Gee M.L, McGuiggan P.M., Israelachvili, J. N, Homola H M, "Liquidlike to solidlike transitions of molecularly thin films under shear" *Journal of Chemical Physics* **93** 3 (1990)
4. Mukhopadhyay A., Zhao J., Bae S. C., Granik S., " Contrasting Friction and Diffusion in Molecularly Thin Confined Films", *Physical Review Letters*, **89**, 13, 136103, (2002)
5. Tas N. R., Haneveld J., Jansen H. V., Elwenspoek M., van den Berg A., " Capillary filling speed of water in nanochannels" *Applied physics letters*, **8**, 15, 3274, (2004)
6. de Gennes, P.G., "Scaling concepts in polymer physics", Cornell University Press, Ithaca, New York. (1979)
7. Balducci A., Hsieh C. C, Doyle P.S., "Relaxation of stretched DNA in slitlike Confinement" *Physical Review Letters*, **99**, 23, 238102, (2007)
8. Tengenfeldt J. O., Prinz C., Cao H., Chou S., Reisner W., Riehn R., Wang Y. M., Cox E. C., Sturm J. C., Silberzan P., Austin R. H., "The dynamics of genomic-length DNA molecules in 100 nm channels" *PNAS,* **101**, 30, 10979 (2004)
9. Brochard, F& de Gennes, P.G, " Dynamics of confined polymer chains" *Journal of Chemical Physics*, **67**, 52, 56 (1977)
10. Martin F., Walczack, R., Boioraski A., Cohen M., West T., Cosentino C., Ferrari M., "Tailoring width of microfabricated nanochannels to solute size can be used to control diffusion kinetics" *Journal of controlled release* **102**, 123, (2005)
11. Cosentino C., Amato F., Walczak R., Boiaraski A., Ferrari M., "Dynamic Model of Biomolecular Diffusion Through Two-Dimensional Nanochannels" *Journal Physical Chemistry B*, **109**, 7358 (2005)
12. Desai T.A., Chu W. H., Tu J. K, Baettie G. M., Hayek A.,Ferrari M., "Microfabricated immunoisolating biocapsules" *Biotechnology and Bioengineering*, **57**, 118, (1998)
13. Desai T.A., Hansford D., Ferrari M." Characterization of micromachined silicon membranes for immunoisolation and bioseparation" *Journal of Membrane Science*, **159**, 221, (1999)

14. A. Salonen, A. M. Kaukonen, J. Hirvonen, V.-P. Letho, ”Mesoporous Silicon in Drug Delivery Applications” *JOURNAL OF PHARMACEUTICAL SCIENCES*, **97**, 2, (2008)
15. Saxton M. J.,” Anomalous diffusion due to obstacles: a Monte Carlo study “ *Biophysical Journal*, **66**, 394 (1994)
16. Lutz C., Kollmann M., Bechinger C.,” Single file diffusion of Colloids in One dimensional Channel”, *Physical Review Letters*, **93**, 2, 26001, (2004)
17. Chou C. Y., Eng B. C., Robert M.,“One dimensional diffusion of colloids in polymer solution” *The journal of chemical physics* **124**, 044902 (2006)
18. Mathé J., Di Meglio JM, Tinland B., “ Diffusion of latex and DNA chains in 2D confined media” *Journal of Colloid and interface science*, **322**, 315 (2008)
19. Hell SW” Toward fluorescence nanoscopy “ *Nature Biotechnology*, **21**,11, 1347,(2003)
20. Hell S.,W., Wichmann J, “Breaking the diffraction resolution limit by stimulated – emission-depletion fluorescence microscopy”, *Optics Letters*, **19**, 11, 780 (1994)
21. Elson E. L., Magde D” Fluorescence correlation spectroscopy I, Conceptual basis and theory” *Biopolymers* **13**, 1 (1974)
22. Schwille, P., U. Haupts, S. Maiti, and W. W. Webb. “Molecular dynamics in living cells observed by fluorescence correlation spectroscopy with one- and two-photon excitation”. *Biophysical Journal.* **77**:2251–2265. (1999)
23. Wachsmuth M., Waldeck W., Langowski J., “Anomalous diffusion of fluorescent probes inside living cell nuclei investigated by spatially resolved fluorescence correlation spectroscopy“, *Journal of Molecular Biology*, **298**, 677, (2000)
24. Pappaert K, Biesemans J., Clicq D., Vankrunkelsven S., Desmet G.,” Measurements of diffusion coefficients in 1-D micro- and nanochannels using shear-driven flows”, *Lab on a Chip,* **5**, 1104-1110, (2005)
25. Gosh M., Blom H., Holm J., Heino T., Rigler R., “ Hydrodinamic flow profiling in microchannel structures by single molecule fluorescence correlation spectroscopy” *Analytical Chemistry* **72**, 3260, (2000)
26. Lenne P. F., Colombo D., Giovanni H., Rigneault “Flow Profiles and Directionality in Microcapillaries measured by Fluorescence Correlation Spectroscopy “ *Single molecules* , **3** , 4 , 194 (2002)

CHAPTER 2

Diffusion

Diffusion processes have been studied for more than 180 years. Interesting to note, there are two main approaches for studying diffusion fundamentals: either a macroscopic approach which starts from the observation and explanation of the phenomenological behavior and ends up with their mathematical solution, established by Adolf Fick, or a microscopic approach, according to the random walk theory initiated by work of Brown, and Maxwell and pursued by Einstein. During the time these two approaches have been developed in parallel and nowadays the macroscopic treatment is more in use for engineers purposes whereas the microscopic approach is rather used by physicists.

The macroscopic approach summarized by Fick's laws have been successfully applied also to predict the diffusion kinetics of molecules through thin semi permeable membranes. Nevertheless, experiments have shown that, as the size of the membrane pores approaches the molecular hydrodynamic radius, unexpected effects, which cause substantial deviations from kinetics predicted by Fick's laws, can occur.

Justified by the interest in understanding motion on the nanoscale, we have to follow both treatments. We must have an atomistic and microscopic comprehension in order to derive macroscopic engineering solutions for the diverse already mentioned applications.

Macroscopic approach

Historical note:

In 1855 Fick was an anatomy demonstrator in Zurich, studying biophysical coherences in the human body, when he proposed his quantitative laws of diffusion. He focused on topics such as air mixing in lungs, hydrodynamics of blood circulation and the work of the heart as well as the mechanics of muscular contraction. Fick realized the analogy between diffusion and Fourier's law of heat conduction as well as Ohm's law of electricity, which is described by the same mathematical formalism. Fick combined the approach given by Fourier with the conservation of matter and ended up with the partial derivative equation of the second degree commonly known as Fick's first law[1]. To verify the equation, Fick connected two reservoirs, one with pure water and one with salt water by tubes of different length. He recapitulated that “the amount of salt was determined, which diffused out of the terminal section of the tube, in measured spaces of time, and which therefore also, in the same time, passed through any section of the cylindrical tube".

Diffusion on the macroscopic scale is in fact driven by chemical potential caused by a concentration gradient, which has to be balanced due to entropic reasons. As Fick derived, the particle flux J is proportional to the diffusion coefficient D and the concentration gradient ∇C:

$$J = -D\nabla C \tag{1}$$

The continuity equation for mass conservation in eq. 2 is applied

$$\frac{\partial C}{\partial t} = -\nabla J \tag{2}$$

which leads to Fick's law of diffusion:

$$\frac{\partial C}{\partial t} = \nabla(D\nabla C) \tag{3}$$

that under the assumption of isotropic diffusion can be written as:

$$\frac{\partial C}{\partial t} = D\nabla^2 C \tag{4}$$

Consequence of eq. 4 is that the flux has a maximum at the place with the highest difference in concentration, and that the concentration does not change with time at the place with the highest flux. The power of this approach lies in the fact that it allows to predict the distribution of concentrations at any given time, just by knowing the initial concentrations and boundary conditions that define the diffusing system.

If the problem is spherically symmetric the flux is radial and we can write:

$$\frac{\partial C}{\partial t} = D\frac{1}{r^2}\frac{\partial}{\partial r}\left(r^2\frac{\partial c}{\partial r}\right) \tag{5}$$

If we consider as initial boundary conditions an initial number of particles equal to N all in position r=0 at time t=0, we can compute the following solution:

$$C(r,t) = \frac{N}{(4\pi Dt)^{3/2}}e^{-r^2/4Dt} \tag{6}$$

Eq. 6 represents clearly a 3D Gaussian distribution.

The relation presented for the mass flux J is valid as long as no external forces are applied to the particle. In presence of an external potential *U(r)* a force $F = -\nabla U$ is acting. For laminar diffusion, velocity is given by $\nu = F/\zeta$. The friction coefficient ζ depends on viscosity η and shape of particles. For spherical objects with radius R in liquids, Stokes defines ζ as:

$$\zeta = 6\pi\eta R \tag{7}$$

The directed velocity causes an additional flux J = cν which enhances Fick's first law to:

$$J = -D\nabla C - \frac{C}{\zeta}\nabla U \tag{8}$$

From equation 8., at equilibrium, which means zero flux, is possible to recall the microscopic theory, and impose Boltzmann distribution for concentration:

$$D\nabla e^{\frac{(-U(r))}{KT}} = \frac{1}{\zeta}e^{\frac{(-U(r))}{KT}}\nabla U \tag{9}$$

After computing we can derive the follow eq.:

$$\frac{D}{KT}e^{\frac{(-U(r))}{KT}}\nabla U = \frac{1}{\zeta}e^{\frac{(-U(r))}{KT}}\nabla U \tag{10}$$

Which leads to the Einstein relation:

$$\frac{D}{KT} = \frac{1}{\zeta} \tag{11}$$

This fundamental equation matches the diffusion coefficient as a macroscopic parameter to all microscopic properties. In particular for a spherical rigid particle we can compute:

$$\frac{D}{KT} = \frac{1}{6\pi\eta R} \tag{12}$$

Equation 12 is commonly known as Stokes-Einstein relationship.

Microscopic approach

Historical note

Robert Brown was investigating organic and inorganic powder suspensions using microscopy in 1827 when he found an unexpected motion of micron-sized particles. In contrast to all prior scientists he thought the origin of these motion was a physical force[2]. But he needed Thomas Graham work first and Maxwell's as well to discover the Brownian motion. In fact, the inventor of dialysis, Graham, started his research in 1828 on gas diffusion and determined that gases diffused spontaneously, mutually and equally through each other. He also noticed that diffusion in liquids was three order of magnitudes smaller than in gases. Graham performed the first quantitative experiments on diffusion, which is particularly remarkable because the notion of a coefficient of diffusion was not yet established until 1855 by Fick [1]. Later on in 1867 Maxwell calculated the diffusion coefficient for CO_2 in air, recalling Graham's experimental data from 1828. Almost eighty years after Brown finally discovered the "Brownian Motion". The close relationship between Brownian motion and diffusion was discovered and put into a mathematical formalism by Albert Einstein[3] in 1905. Einstein recognized that the characteristic value to describe particle diffusion was the mean square displacement in a defined time and not the averaged velocity of the particle. Einstein proposed the fundamental relation between the macroscopic particle quantity and the microscopic one, by relating the diffusion coefficient with the mean square displacement. In the following period, the analysis of "random walk"' trajectories as obtained from observing the Brownian motion of small particles in liquids was carried out. In 1913, Jean-Baptiste Perrin were able to verify Einstein's equation by experiments[4]. Perrin claimed that if it was possible to plot positions of particles in the trajectory in a hundred times smaller time interval, the shape of the linear trajectory segments would take also a polygonal shape as complicated as the whole trajectory, and so on. Interestingly, Perrin described with these assumptions the behavior of a fractal line, half of a century before Benoit Mandelbrot published his work "Fractal Geometry of Nature"[5].

In the Einstein treatment of the random walk model for diffusion, the motion of a molecule consists of periods of undisturbed motion interrupted by sudden changes of direction when it collides with another molecule. The collisions affects in general the speed of the molecule but its average speed remains constant as long as the temperature is fixed. The random walk model assumes that the time between collisions is a constant τ,

the direction of motion is completely randomized by a collision, thus molecules have no memory of the past, and molecule speed v stays constant. Therefore the distance d between two collisions, also called the step length, is constant as well and it is given by d= vτ. The complete time t of a walk can be expressed as the number of steps n since t and is given by n=t/τ.

In one dimension the molecule has just one degree of freedom x, and can only move forward or backward. After n steps the molecule has the position[7]

X(n)=X(n-1)±d (13)

Steps forward (+d) have the same probability as steps backward (−d) and all individual steps are independent. Considering an ensemble of identical molecules starting at x=0 at t=0, their average x will be zero at all times: $\langle x(t)\rangle^2 = 0$. With time, i.e. with increasing number of steps, however, a spread of the ensemble occurs. This spread can be described by the standard deviation σ of x which is equal to the mean square displacement as the average is zero that is reported in eq. 14:

$$\sigma = \sqrt{\langle x^2(t)\rangle - \langle x(t)\rangle^2} = \langle x^2(t)\rangle \quad (14)$$

Thus, the mean square of the distance is:

$$\langle x^2(n)\rangle = \langle x^2(n-1)\rangle + \langle \pm 2dx(n-1)\rangle + \langle d^2\rangle = \langle x^2(n-1)\rangle + \langle d^2\rangle \quad (15)$$

In the last term of equation 15 the mix products average is zero due to the equal probability to have positive or negative sign. From eq. 15 it follows:

$$\langle x^2(n)\rangle = nd^2 \quad (16)$$

Thus the mean-square displacement in eq. 14 increases linearly with the number of steps n, and therefore with time t as it is reported in eq. 17.

$$\langle x^2(t)\rangle = \frac{d^2}{\tau}t \quad (17)$$

The step length d and the time for one step τ of eq. 17 can be replaced by the diffusion coefficient D, which is defined as:

$$D \equiv \frac{d^2}{2\tau} \quad (18)$$

It follows that in 1D random walk motion the mean square displacement is proportional to time and to D as reported in eq. 19:

$$\langle x^2(t)\rangle = 2Dt \quad (19)$$

Under the assumption of isotropic motion we can derive the expressions for 2D and 3D motion:

2D: $$\langle x^2(t)\rangle + \langle y^2(t)\rangle \rightarrow \langle r^2(t)\rangle = 4Dt \quad (20)$$

3D: $$\langle x^2(t)\rangle + \langle y^2(t)\rangle + \langle z^2(t)\rangle \rightarrow \langle r^2(t)\rangle = 6Dt \quad (21)$$

During a typical observation time, each particle takes many steps on the 1D random walk. The probability that a random walking particle took a total of k steps to the right after a sequence of n steps in the random walk is provided by a binomial distribution:

$$P(k;n,q) = \frac{n!}{k!(n-k)!}(q)^k(1-q)^{n-k} \quad (22)$$

Where q is the probability of moving to the right at each step which is q=1/2 for an unbiased random walk. By using the binomial distribution, it is possible to determine p(x), which is the probability of finding a particle at a position x+dx as a function of time after a large numbers of individual steps have occurred:

$$p(x) = \frac{1}{\sqrt{4\pi Dt}} e^{-x^2/4Dt} dx \quad (23)$$

This equation 23 describes a Gaussian distribution and it can be also referred to as the Brownian propagator. In fact the random walk model predicts that diffusing molecules, placed in the origin at zero time point, spread over time in a way that the mean position is unchanged, but the variance in the distribution increases as a 2Dt. This result has been already found in the macroscopic treatment for diffusion in a 3D form.

Interestingly, if only a two dimensional projection of a three dimensional diffusion process is measured, the two dimensional description is valid, because the motion along z is not taken into account. This is somehow not fully intuitive but can be demonstrated analytically. This is the case of many experimental scenarios (imaging, particle tracking, FRAP and FCS on surfaces or quasi surfaces due to resolution limits) where it is not possible to probe 3D motion but only to gain 2D motion information.

As soon as it is proved experimentally that motion is isotropic in all three directions, the components in the *x*, *y*, and *z* directions of the probe movement can be treated as independent, and the analysis of the diffusion behavior based on 2D projections is correctly described by models for 2D motion. This can be shown using the example of free diffusion: the solution of the diffusion equation (eq.4) in 3D and computed in eq. 6, can be evaluated for a molecule with diffusion coefficient *D* at position (x_0,y_0,z_0) at time 0 as the probability to find itself at a position (x_1,y_1,z_1) at time *t* which is given by the Green's function:

$$P_D^{(3D)}(x_1, y_1, z_1, t \mid x_0, y_0, z_0, 0) = (4\pi Dt)^{-3/2} \exp\left[-\frac{(x_1 - x_0)^2}{4Dt} - \frac{(y_1 - y_0)^2}{4Dt} - \frac{(z_1 - z_0)^2}{4Dt} \right] \tag{24}$$

Eq 24 is used to calculate the MSD according to

$$\begin{aligned} \mathrm{MSD}^{(3D)} = & \iiint dx_1 dy_1 dz_1 \iiint dx_0 dy_0 dz_0 W_D(x_0, y_0, z_0) \times \\ & P_D(x_1, y_1, z_1, t \mid x_0, y_0, z_0, 0) \left[(x_1 - x_0)^2 + (y_1 - y_0)^2 + (z_1 - z_0)^2 \right] \end{aligned} \tag{25}$$

where

$$W_D^{(3D)}(x, y, z) = \lim_{t \to \infty} P_D^{(3D)}(x, y, z, t \mid x_0, y_0, z_0, 0) \tag{26}$$

is the equilibrium distribution, leading to the expected linear dependence of the MSD on time

$$\mathrm{MSD}^{(3D)} = \langle r^2(t) \rangle = 6Dt \tag{27}$$

In order to describe the projection of 3D data onto the *x*-*y* plane the integration is changed to

$$\begin{aligned} \mathrm{MSD}^{(3D,\mathrm{proj.})} = & \iiint dx_1 dy_1 dz_1 \iiint dx_0 dy_0 dz_0 W_D(x_0, y_0, z_0) \times \\ & P_D(x_1, y_1, z_1, t \mid x_0, y_0, z_0, 0) \left[(x_1 - x_0)^2 + (y_1 - y_0)^2 \right] \end{aligned} \tag{28}$$

by deleting $(z_1 - z_0)^2$ into eq. 25 and turns out to be the same as for true 2D diffusion:

$$\mathrm{MSD}^{(3D,\mathrm{proj})}. = \mathrm{MSD}^{(2D)} = 4Dt \tag{29}$$

This follows from the definition of the Green's function as a normalized probability distribution and can be generalized to all processes where the Green's function can be factorized into terms each depending on only one spatial coordinate[8].

Deviation from a random walk

The individual mean square displacements do not necessarily follow a linear dependence with the observation time, as shown above for the random walk diffusion. In real systems, the diffusion of an individual particle is often influenced by local anisotropies, such as obstacles, adsorption sites or regions with increased drug or regions with a uniform flow[9-12]. These influences are visualized as deviations from the linear behavior in a MSD versus time. For some specific cases, it is possible to derive analytically a mathematical formula that describes the time dependence of the MSD.

ANOMALOUS DIFFUSION MODEL

In unobstructed diffusion, the mean-square displacement of diffusing particle is proportional to time. But obstruction or binding may lead to anomalous diffusion, in which diffusion is hindered and the mean-square displacement is proportional to a fractional power of time less than one[13]. This can be caused by obstruction by inert obstacles as well as by the presence of binding phenomena[14-15]. The list of systems displaying anomalous dynamical behavior is quite extensive and hosts, among others, the following systems in the sub-diffusive regime: nuclear magnetic resonance (NMR) diffusometry in percolative [16], and porous systems [17], Rouse or reptation dynamics in polymeric systems [18-20], transport on fractal geometries [21], or the dynamics of a bead in a polymeric network [22]. Anomalous diffusion in the presence or absence of an external velocity or force field has been modeled in numerous ways, including fractional Brownian motion [5], generalized diffusion equations [23], Langevin equations [24], generalized master equations [25].

Anyway there is still open discussion in literature to how to write a generalized diffusion equation which comprise anomalous diffusion behavior.

In first attempts of generalizing the standard diffusion equation for the description of diffusion processes on fractal geometries of dimension d_f, radius-dependent diffusion coefficients were assumed. The generalized diffusion equation [23] reads

$$\frac{\partial C}{\partial t} = r^{1-d_f}\,\frac{\partial}{\partial r} r^{1-d_f} D(r) \frac{\partial}{\partial r} C(r,t) \tag{30}$$

with the radius-dependent diffusion coefficient $D(r) = Dr^{-\Theta}$, and derived the corresponding propagator

$$C(r,t) = A(\Theta, d_f)(D[2+\Theta]^2 t)^{-d_f/(2+\Theta)} \exp\left(-\frac{r^{2+\Theta}}{D(2+\Theta)^2 t}\right) \quad (31)$$

The mean squared displacement for this process, given by $\langle x^2(t)\rangle \propto D_\alpha t$ with $\alpha = 2/(2+\Theta)$ can readily be inferred. As Θ is positive, this result implies sub-diffusion Further investigations indicated that the asymptotic form of the propagator on fractals such as the Sierpinski gasket, is given by the scaling form

$$C(r,t) \propto A(\alpha,\beta)\zeta^\beta \exp(-c\zeta^u) \quad (32)$$

Where $\zeta = r/t^{\alpha/2}$, $u = 1/(1-\alpha/2)$, whit β a system-dependent parameter. This is usually referred to as a stretched Gaussian.

The physical and phenomenological interpretation of anomalous diffusion has been widely investigated but there is still open discussion for some aspects [26-28].

CORALLED DIFFUSION MODEL

Whenever there is a steric confinement due to rather a density increase or a physical boundary to the motion, these can be interpreted as an apparent repulsive force on the bodies which may be approximated linearly. Diffusion in a corresponding isotropic harmonic potential

$$U(x,y,z) = \left(x^2+y^2+z^2\right)\left\langle r_c^2\right\rangle / 6k_B T \quad (33)$$

Can be described by the Green's function:

$$P_D^{(3D)}\left(x_1,y_1,z_1,t \mid x_0,y_0,z_0,0\right) = \left(\frac{\pi\left\langle r_c^2\right\rangle}{3}\right)^{-3/2}\left[1-\exp\left(-2\frac{6Dt}{\left\langle r_c^2\right\rangle}\right)\right]^{-3/2} \times$$

$$\exp\left(-\frac{3\left[x_1 - x_0\exp\left(-6Dt/\left\langle r_c^2\right\rangle\right)\right]^2 + 3\left[y_1 - y_0\exp\left(-6Dt/\left\langle r_c^2\right\rangle\right)\right]^2 + 3\left[z_1 - z_0\exp\left(-6Dt/\left\langle r_c^2\right\rangle\right)\right]^2}{\left\langle r_c^2\right\rangle\left(1-\exp\left[-26Dt/\left\langle r_c^2\right\rangle\right]\right)}\right) \quad (34)$$

where $\langle r^2(t)\rangle$ is the long term MSD in 3D, or the correlation length of the space accessible to the bodies. This Green's function can be factorized as described above. It can be interesting to calculate the MSD projected to the *x-y* plane which gives

$$\mathrm{MSD}^{(3\mathrm{D,\ proj.})} = \left\langle r_c^{\,2} \right\rangle \cdot \left[1 - \exp\left(-\frac{4 D_b t}{\left\langle r_c^{\,2} \right\rangle} \right) \right] \tag{35}$$

for confined body diffusion with a coefficient D_b, now being the long-term MSD in 2D[8].

SINGLE FILE DIFFUSION MODEL

In the case of rigid particle another theory might apply. When the size of the constraint is as small as the particle diameter, then molecules cannot pass each other resulting in single-file diffusion process. In this case the Green's function can be written as:

$$p(x,\ t)\ =\ \frac{1}{\sqrt{4\pi F t^{1/4}}} \exp(-x^2/4Ft^{1/2}) \tag{36}$$

The mean square displacement does not scale linearly with time anymore but it is:

$$\langle r^2(t) \rangle = 6Ft^{1/2} \tag{37}$$

Where F is a mobility coefficient. This model does not account for wall-particle interactions, neither molecule's flexibility, whereas it only predicts interacting rigid wall particles motion when mutual passage is impossible[29-30].

A small collection of such diffusion equations is given below:

Normal diffusion: $\langle r^2(t) \rangle = 6Dt$ (38)

Anomalous diffusion: $\langle r^2(t) \rangle = 6\Gamma t^{\alpha}, 0 < \alpha < 1$ (39)

Diffusion and convection: $\langle r^2(t) \rangle = 6Dt + (Vt)^2$ (40)

Coralled motion: $\langle r^2(t) \rangle \cong \langle r_C^{\,2}(t) \rangle \left[1 - A_1 \exp\left(\frac{(-6A_2 Dt)}{\langle r_C^{\,2}(t) \rangle} \right) \right], A_1, A_2 \neq 0$ (41)

Single file diffusion: $\langle r^2(t) \rangle = 6Ft^{1/2}$ (42)

MSD

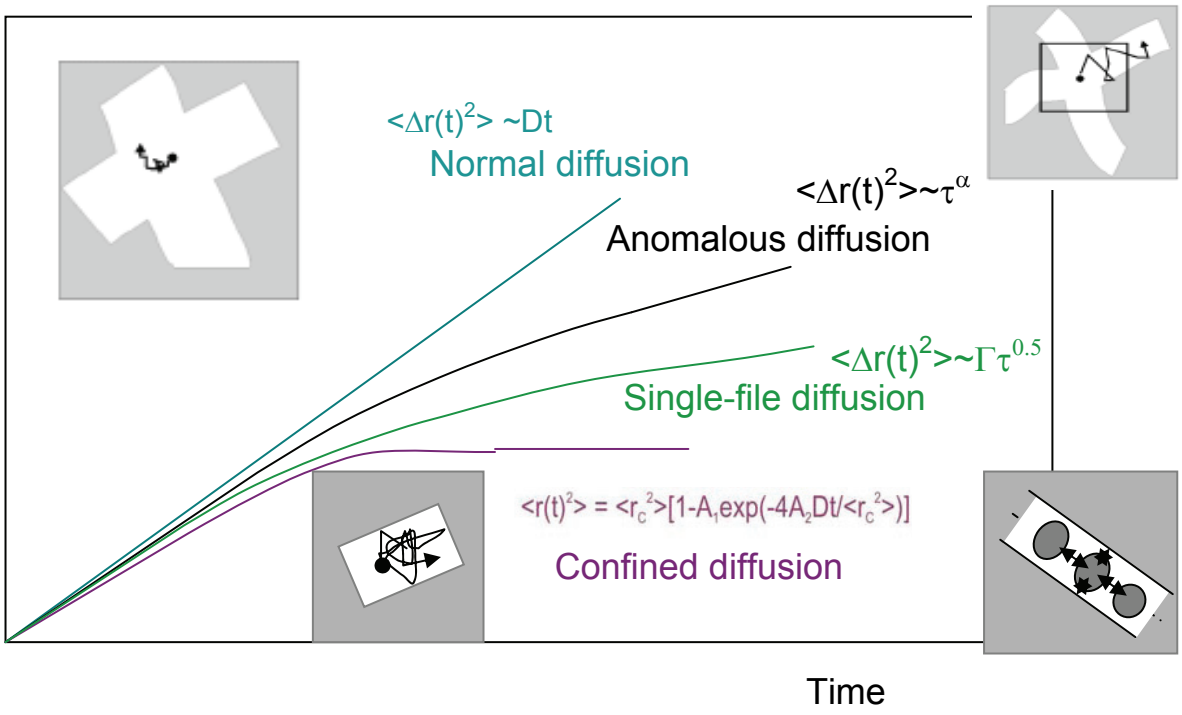

Figure 1 : Various modes of motion under different conditions. The mean-square displacement $\langle r^2(t)\rangle$ as a function of time t for, pure diffusion, anomalous diffusion, single file diffusion and confined motion.

Normal diffusion gives a linear curve through the origin. In the case of anomalous diffusion in which the exponent α is a number between 0 and 1, the curve has a decreasing slope. In the case of single file diffusion the anomalous exponent is 0.5. In the last case a molecule diffuses within a confined region. It can be shown that the value of the asymptote $\langle r_c^{\,2}(t)\rangle$ corresponds to the effective area of the confinement. The other parameters in equation 10 (A_i) relate to the confinement geometry, and are not easily obtained analytically[12].

Influence of pores and confinement on diffusion

The influence of pores and generally of geometrical constraints on the diffusion behavior can be complex. Diffusivity is in general reduced due to the presence of barriers and confinement. Many parameters play a role in the diffusivity reduction, such as barrier dimension, geometrical shape and arrangement, molecule dimension, deformability, flexibility and chemical nature; molecule-barrier interactions and type of interaction, which can cause molecules to undergo for instance absorption/desorption kinetics.

An important issue is the time scale at which diffusion deviate from its bulk behavior. If the temporal or spatial scale of the influences is large in comparison to the temporal and spatial resolution of the experimental apparatus, the diffusion will be perceived as unaffected by the geometrical constraint. If the temporal or spatial scale of the effects is comparable to the trajectory size the diffusivity becomes anomalous. If the interactions take place on a very short time-scale, and if the molecules are otherwise free to diffuse in interconnected pores, the effects average out to give a normal diffusivity with a reduced effective diffusion coefficient, D_{eff} .

The macroscopic approach gives a quite convincing treatment in which the diffusivity coefficient simply scale with same parameters due to the geometry. The ratio between the effective and the free diffusion coefficients (D_{free} /D_{eff}) can be expressed by a factor R, which comprises the influences of the geometry (e.g. the tortuosity) and interconnectivity of the pores for long observation times. This relationship is a useful tool for engineers but lucks completely in the microscopic mechanism.

The influence of the geometrical constraints can, however, be more complicated. The case we investigate in this work belongs to this frame: the pores or the channels are so narrow that molecules might have to change their conformation depending on their size and on their chemistry. In any case molecular hits against the nanomaterial walls are much more probable compared to a bulk diffusion process. The geometry of the confinement in both membrane's pores and nanochannels might introduce anisotropy into the motion, as the axial direction is usually jumping free whether motion in the radial direction of the pores might be hindered. In the nanochannels anisotropy could be revealed on every direction as the height is nanometric and the width is micrometric. This could influence the motion in a different way.

Then it is not clear how to predict molecules motion in these scenarios. The anomalous behavior expressed as a non linear dependence of the mean square displacement with time, has not clarified all the possible aspects yet for this phenomenon. Another doubtful

aspect would be the meaning of the diffusion coefficient as it is not a constant anymore but it results as a function of time.

Generally, as we have reported, the effects of the geometrical constraints are difficult to predict analytically, and results are usually compared with simulations. With good probability the dynamic behavior of a molecule in its transport process across a channel or a pore might be dependent on the diffusion step it is undertaking. We can of course highlight two main processes in this phenomenon, first being the entry in the pore rather than a channel or slit, also named as translocation, and second the diffusion transport within the pore. Both processes might have characteristic parameters to be considered for a theoretical discussion.

Figure 2: Cartoon representing the two main processes involved in diffusion in confinement or in pores, entry and diffusion.

Translocation across a pore has been also widely investigated in the literature. Main theoretical results have been proposed for biased translocation [31], which is not a relevant aspect for this thesis work. In the work of Panja et al. (2008), some scaling arguments are presented for the unbiased translocation of polymers, and the main result is that translocation is a time-dependent process where for $\tau < \tau_{rouse}$ the process is sub-diffusive whereas for $\tau > \tau_{rouse}$ it becomes diffusive[32].

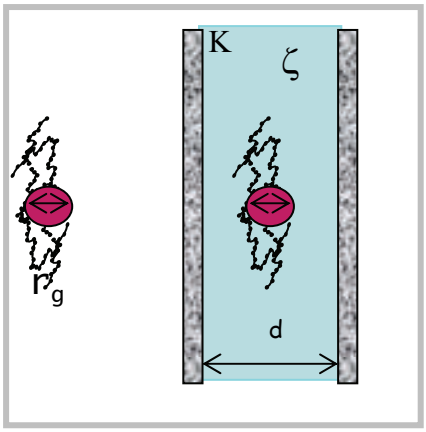

Figure 3:Cartoon showing different parameters involved in the diffusion process.

In the diffusion process in a confined environment parameters that might play a role are molecular weight, radius of gyration, molecule's rigidity or flexibility, channel's characteristic dimensions, the friction exerted by the solvent on the diffusing molecule, and molecule - wall interactions which can be translated into a repulsive rather than an attractive interaction energy.

Efforts to measure diffusion deviation from bulk behavior due to confinement and barriers are ongoing since decades. Two main treatments have been proposed in literature. An hydrodynamic treatment developed in the 70s could predict rigid and non-interacting molecules behavior, whereas it did not account for particle-wall interaction and molecule's flexibility. In chapter 4 it will be reviewed in more detail. In the same period the scaling theory from de Gennes were applied to both polymer dynamic and static features. Scaling arguments were derived to account for molecule's flexibility but not for molecule-wall interactions. None of the mentioned theories can explain all possible undergoing mechanisms.

More experimental work is ongoing to derive confinement effects on diffusion.

References

1. Fick A., " On liquid diffusion" *The London, Edinburgh and Dublin Philosophical magazine and Journal of Science*, **10** (4), 30-39 (1855)
2. Brown R., *The miscellaneous botanical works of Robert Brown: Volume 1*., R. Hardwicke, London (1866)
3. Einstein A., " Uber die von der molekularkinetischen Theorie der Warme geforderte Bewegung von in ruhenden Flussigkeiten suspendierten Teilchen" *Annalen der Physik*, **322** (8), 549-560, (1905)
4. Perrin J., *Les atoms*, Félix Alcan (1913)
5. Mandelbrot M.M., *The fractal geometry of nature*, Freeman San Francisco (1982)
6. Muller C. B., PhD dissertation " *Applications of Two Focus Fluorescence Correlation Spectroscopy in Colloid and Polymer Science*" RWTH, (2008)
7. Berg H.C., "*Random walks in biology*" Princeton University Press, (1983)
8. Gorisch S. M., Wachsmuth M., Ittrich C., Bacher C. P., Rippe K., Lichter P., "Nuclear body movement is determined by chromatin accessibility and dynamics" Supporting text, *Proceeding of the National Academy of Science*, **101**, 36, 13221, (2004)
9. Saxton M. J., Jacobson K., Single Particle Tracking: Applications to Membrane Dynamics. *Annual Review on Biophysics and Biomolecular Structures*, **26**, 373, (1997)
10. Qian H. Sheetz M.P., Elson E.L., "Single Particle Tracking: Analysis of Diffusion and Flow in two-dimensional systems*", Biophysical Journal* **60**, 910, (1991)
11. Scutz G.J., Schindler H., Schmidt Th, „ Single Molecule Microscopy on Model Membranes Reveals Anomalous Diffusion. *Biophysical Journal*, **73**, 1073, (1997)
12. Kirstein J. U. PhD dissertation "*Diffusion of single molecules in nanoporous mesostructured materials*" LMU Munchen, (2007)
13. Bouchaud, J. P., and A. Georges "Anomalous diffusion in disordered media. Statistical mechanisms, models and physical applications". *Physics Reports*. **195**:127–29, (1990)
14. Saxton, M. J. "Anomalous diffusion due to obstacles: a Monte Carlo study. *Biophysical Journal* **66,** 394–401. (1994)
15. Saxton, M. J. "Anomalous diffusion due to binding: a Monte Carlo study". *Biophysical Journal* **70**, 1250–1262. (1996)

16. Klemm A, H.-P. Muller, R. Kimmich," NMR microscopy of pore-space backbones in rock, sponge, and sand in comparison with random percolation model" *Physical. Review E* **55** 4413. (1997)
17. Kimmich R., "NMR: Tomography, Diffusometry, Relaxometry", *Springer, Berlin,* (1997)
18. Weber H.W., R. Kimmich, "Anomalous segment diffusion in polymers and NMR relaxation spectroscopy" *Macromolecules* **26,** 2597, (1993)
19. de Gennes P.-G., "Scaling Concepts in Polymer Physics", *Cornell University Press, Ithaca*, (1979).
20. Doi M,. S.F. Edwards," The Theory of Polymer Dynamics", *Clarendon Press*, Oxford, (1986)
21. Porto M., A. Bunde, S. Havlin, H.E. Roman, " Structural and dynamic properties of the percolation backbone in two and three dimensions" *Physical. Review E* **56** 1667. (1997)
22. Barkai E., J. Klafter, " Comment on "Subdiffusion and Anomalous local viscoelasticity in Actin Networks"" *Physical Review Letters*. **81** 1134. (1998)
23. O'Shaugnessy B., I. Procaccia, *Physical Review Letters*. **54** 455. (1985)
24. Fogedby, H.C. " Langevin equations for continuos time Lévy flights" *Physical Review Letters* **73** 2517. (1994)
25. Oppenheim I., K.E. Shuler, G.H. Weiss (Eds.), "Stochastic Processes in Chemical Physics: The Master Equation", *MIT Press, Cambridge, Massachusetts*, (1977)
26. Metzler R., Klafter J., "The random walk's guide to anomalous diffusion: a fractional dynamics approach*" Physics Reports* **339** 1-77(2000)
27. Saxton, M. J.. "The biological meaning of anomalous subdiffusion." *Biophysical Journal* **84**:487. (2003)
28. Saxton, M. J.. "A Biological Interpretation of Transient Anomalous Subdiffusion. I. Qualitative Model" *Biophysical Journal* **92** 1178–1191(2007)
29. Lutz C., Kollmann M., Bechinger C.," Single file diffusion of Colloids in One dimensional Channel", *Physical Review Letters*, **93**, 2, 26001, (2004)
30. Chou C. Y., Eng B. C., Robert M.,"One dimensional diffusion of colloids in polymer solution" *The journal of chemical physics* **124**, 044902 (2006)
31. de Gennes P.G. "Passive entry of a DNA molecule into a small" *Proceeding of National Academy of Science* **96**, 7262, (1999)

32. Panja D., Barkema G. T., Ball R.C, " Polymer translocation out of planar confinements", *Journal physics: Condensed Matter,* **20,** 075101 (2008)

CHAPTER 3

Nanoporous membrane fabrication and experimental set up

The interest in manufacturing micro and nanofabricated membranes is of scientific and technological relevance because of the presence of voids of controllable dimensions at the atomic and molecular level, which is the nanometer scale. This enables the membranes to discriminate and interact with selected molecules, thus allowing greater control of dose profile for drug delivery applications or improving ultra-filtration technologies. Mesoporous materials have in fact many interesting properties considering size-separation of macromolecules and drug delivery applications. The small size of the pores (2–50 nm) confines the space of a drug and engages the effects of surface interactions of the drug molecules and the pore walls. Depending on the size and the surface chemistry of the pores, sustained release of a drug or more interestingly, zero order release kinetic can be obtained.

The way membrane pore dimension and structure can affect the releasing profile, which is related to the diffusion properties of molecules confined within membrane's pores, is still unclear. In order to correlate membrane geometrical features to the diffusion behaviour of confined molecules, we manufactured silicon nanoporous membranes to subsequently evaluate their release features. To this aim two different experimental set-up were designed, uniaxial release from transwell and diffusion cell analysis.

State of the art

Several interesting technologies have already been investigated for manufacturing nanoporous membranes. Gong et al. demonstrated the use of mechanically robust nanoporous alumina capsules, with uniform pores of 25 nm to 55 nm for controlled drug delivery. The nanoporous alumina capsules were fabricated by a two step anodization process of an alumina tube and pore diameter could be easily controlled via the anodizing voltage relationship of 1.29 nm/V [1]. A breakthrough in membrane fabrication technology has been the application of microfabrication technology in this field.

Desai et al. used bulk and surface micromachining to obtain micromachined biocapsules. The design of the microfabricated biocapsule consisted of a surface micromachined membrane on top of an anisotropically etched silicon wafer, which provided mechanical support. To reach pore size in the tens of nanometres range, they developed strategies based on the use of a sacrificial oxide layer, sandwiched between two structural layers, for the definition of the pore pathways[2].

Tong et al described a technique to manufacture 25 nm pores by Focus Ion Beam (FIB) in silicon nitride on a microfabricated 5 μm structure, with a silicon frame beneath to support the fragile sieve[3]. A new transfer technology was demonstrated by Unnikrishnan et al., where a delicate thin-film nano-membrane is supported on a robust silicon microsieve fabricated by plasma etching. The silicon sieve is micromachined independent of the thin film, which is later transferred onto it by fusion bonding. Using this thin-film transfer technique, nano-membranes down to 50 nm thickness have been fabricated[4].

Porous silicon (PSi) materials have some advantages compared to the silica-based materials, but also some disadvantages, like a wider pore size distribution. Since the demonstration of visible photoluminescence of PSi, first reported by Prof. Canham in 1990 this material found many new interesting applications[5]. PSi was found to be bioinert, bioactive or biodegradable[6]. The speed of dissolution of Psi, for instance, depends on the porosity and pore size, and it can be predicted and controlled with fabrication parameters. One of the main research topics in the Psi bioapplication studies, in addition to drug delivery, has been biosensing and, based on this, protein adsorption on the PSi surface. It has recently been demonstrated as a charge- and size- based separation tool of macromolecules[7].

The basic method to fabricate PSi is electrochemical dissolution of Si in HF based solutions. This is obtained by monitoring either the anodic current (galvanostatic) or voltage (potentiostatic). In general, constant current is preferable as it allows better control

of the porosity and thickness. It also provides better reproducibility from sample to sample. In the simplest setup to fabricate PSi, plates of Si and Pt are dipped into HF solution and an etching current is applied between these electrodes. The porous layer is formed on the surfaces of the Si, which is used as a positive anode. Usually a cathode is made of platinum and the fabrication cell has to be made of HF-resistant material, for example Teflon. Dilute aqueous HF or ethanolic - HF are generally used as electrolytes. Ethanol is added to reduce formation of hydrogen bubbles and to improve the electrolyte penetration in the pores and, thus, uniformity of the PSi layer[8]. The n-type Si substrate has to be illuminated during anodization to generate photo-excited holes on the surface. In the case of p-type substrate this is not required [9]. Although PSi can be fabricated with the very simple setup described above, the disadvantage of this system is the nonuniformity in both the porosity and thickness of the PSi layer. This is especially true if highly resistive Si substrates are used, because the current flow from the anode (Si) has its highest value at the surface of the electrolyte. The potential drops laterally along the substrate as the electrolyte reaches the deeper structures of the Si substrate. This induces porosity and thickness gradients. If the substrate is of low resistivity and the lateral dimension is much larger than the dip length, the porosity and thickness gradients are reasonably small. These gradients, however, can be avoided by using an anodization cell based on anodized Si substrate in contact with a conductive anode material. The good contact is important for attaining a homogeneous PSi layer that is commonly obtained using a metal deposition on the backside of the Si wafer. After the etching, the next step to be considered is drying of the PSi material, if a liquid electrolyte has been used. Drying, if the electrolyte in the pores is allowed to evaporate at atmospheric pressure and temperature, may induce cracking and shrinkage. Especially the higher, brittle porosity structures (>75%) often do not have mechanical strength enough to survive the electrolyte evaporation without significant degradation in the structure. This is because the formed liquid vapor interface can generate large capillary stresses. In most cases (porosity <75%), drying of PSi in laboratory air or under nitrogen flush is feasible. Almost all properties of PSi, such as porosity, porous layer thickness, pore size and shape, as well as microstructure, strongly depend on the fabrication conditions. In the case of anodization, these conditions include HF concentration, chemical composition of electrolyte, current density (and potential), wafer type and resistivity, crystallographic orientation, temperature, time, electrolyte stirring [10]. Thus, a complete control of the fabrication is complicated and all possible parameters should be taken into account. The effects of dopant type and concentration on

the pore morphology of particles are rather well characterized and the morphologies are usually grouped into four categories: n, p, n+, p+. As the dopant concentration increases (and the resistivity decreases), the pore diameters and inter-pore matter lengths also increase. This means that a finer mesoporous structure could be obtained with low-doped Si substrates. Also the type of dopant affects the pore diameters. In the n-type PSi, the pore diameters are usually larger than in the p type Psi. Decreasing concentration of HF usually reduces the dimensions of the forming structures, and usually smoother and straighter pores are formed. The pore shape is frequently observed to be not only cylindrical (or spherical), but also rectangular pores at least in n-type Psi[11]. Using higher current densities, more linear pores are formed. Generally, an increase in current density or anodization potential leads also to an increase in the pore diameter. A more complicated situation is met, if specific pore volumes or surface areas are considered. For example, in the case of p+-type Si, the surface area/weight is increased when the current density is increased[12], but, at the same time, also the porosity is increased[13].

Fabrication process

Porous silicon is obtained by electrochemical etch in fluoridric acid based solution starting from a silicon substrate. A photolithographic process is carried to delimit the area where to produce the porous layer. Then the porous silicon membranes are obtained by an electrochemical etch followed by a lift off technique.

In order to obtain porous membranes of roughly 0.5 cm^2 area, 8 mm in diameter, it was first necessary to design a photolithographic mask of proper dimensions. Silicon wafer of type p+ and of <100> orientation were first cleaned in ethanol solution and dried in nitrogen air, then a 5 A layer of aluminum was deposited on the back side. The wafer were then annealed for 15 minutes at 400°C and placed on a spinner for the photoresist application process. S1818 positive type photoresist was spun at 22 rpm for 30 seconds over the cut wafers which were then dried in a oven for 10 minutes at 100°C and then exposed to UV radiation at 10mW through a Mask-Aligner for 10 seconds. The exposed samples were then developed in DE126 for 10 seconds and nitrogen dried. In order to obtain the nanoporous structure, the processed wafers were placed in an electrochemical cell in a 50% w/w fluoridric acid in ethanol solution. A current density of 17 mA /cm^2 was applied for 10, 20 or 30 minutes to achieve nanoporous formation on the top of the fresh exposed layer to the acid solution, and subsequently a lift off current density of

150mA/cm^2 was applied for 15 seconds to detach the nanoporous layer originated during the electrochemical etch from the silicon wafer chips.

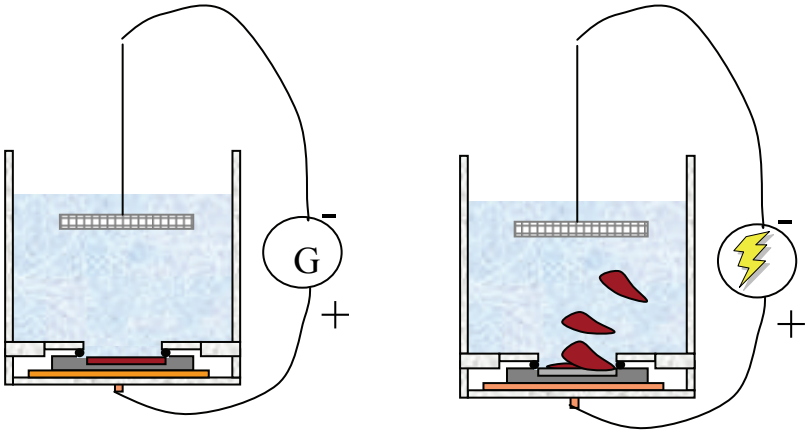

Figure 1: Cartoon of the anodization cell during electrochemical etch and lift off technique

Parameters optimization

Membranes detached from the wafer were collected from acid solution and washed in ethanol, rinsed in pentane and air dried.

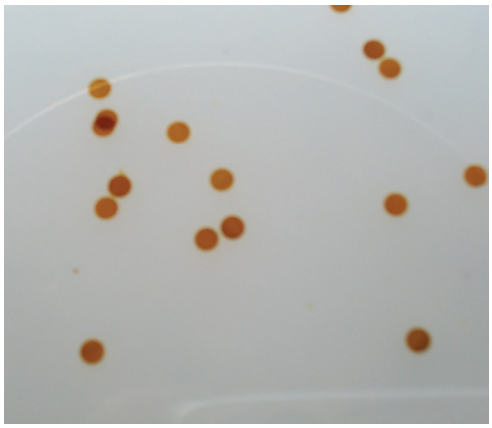

Figure 2: Porous silicon membranes collected from the etching solution and rinsed in pentane.

Membrane thickness was measured by means of a αSTEP profilometer and a strict dependence with electrochemical etch duration was found. Measured values are shown below.

Etching time [min]	10	20	30
thickness [μm]	22-24	40-45	50-53

Table 1: Porous silicon membranes thickness

Optical and morphological characterization

Fabricated membranes were optically inspected by Scanning Electron Microscopy (SEM). From an elementary statistical observation of the taken pictures it was possible to roughly characterize the pore dimension obtained.

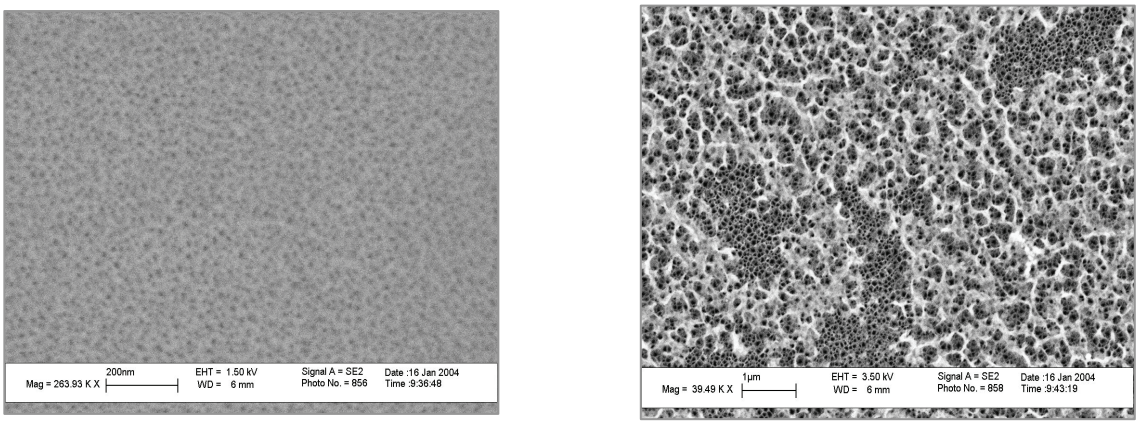

Figure 3: SEM micrographs of the two surfaces of the manufactured membranes. Left: Above surface. Right: Bottom Surface.

In fact, it was found that the membranes side exposed to the acid solution had an average pore diameter of about 10 nm, whereas the opposite side had pore diameter in the range 10 to 100 nm. We could not identify any relationship between pore morphology and etching duration whereas it is known from literature that pores morphology and dimension are affected by the chemical nature of the substrate in use[10].

Membranes were then morphologically characterized by nitrogen sorption.

After degassing, pure nitrogen at 77K° was initially inserted at a rate of 5 cm^3 per gram of sample and then at sequentially increasing rates which anyway allow the system to get back to equilibrium. From nitrogen adsorption isotherm it is possible to evaluate the sample surface area applying BET method, and the total pore volume and the pore dimension distribution from the BJH method. Adsorption isotherms give the relationship between the adsorbed gas amount at the gas pressure in equilibrium with the adsorbed gas at constant temperature. This relationship is given by Langmuir isotherm under the hypothesis of equivalent adsorption sites. Whenever sites are not equivalent, whether because they are partially filled or morphologically diverse, Langmuir equation does not hold anymore and it is replaced by BET (Brunauer, Emmett et Teller) equation. An adsorption isotherm graph is built in the 0.05-0.35 range of relative pressure which is related to the formation of a single layer of nitrogen molecules adsorbed onto the sample surface. The BET equation is then applied to this range and it returns an experimental

evaluation of the sample surface area. Moreover some typical adsorption-desorption curves are known to be characteristic of specific pore shapes, and it is in fact possible to qualitatively describe it comparing the experimental one with literature results.

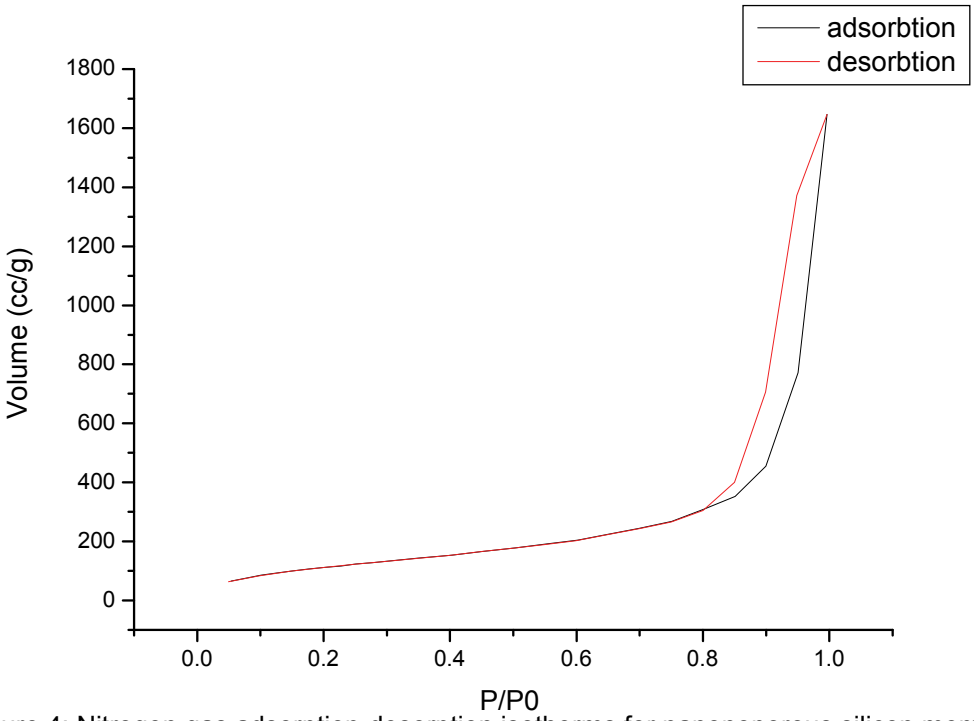

Figure 4: Nitrogen gas adsorption-desorption isotherms for nanonoporous silicon membranes.

Applying the BET model to nitrogen adsorption isotherms of nanoporous silicon membranes, a surface area of 442 m^2/g was found. The hysteresis on the adsorption – desorption curves could be related to capillary condensation in mesopores, thus showed that membranes have pores of mesoscopic dimension. Hysteresis shape was typical of pores having a narrow dimension distribution of slit-shaped mesopores. [14]. From Barrett–Joyner–Halenda (BJH) procedure is then possible to evaluate the pore dimension distribution. Given that adsorption can be described as a two step process, which implies surface adsorption on pore surfaces and capillary condensation in the pore volume, BJH model reads as:

$$V = \sum_{i=1}^{k} \Delta V_i (r_i \le r_c) + \sum_{i=k+1}^{n} \Delta S_i t_i (r_i > r_c) \qquad (1)$$

Where V, the gas adsorbed volume, is given as sum of condensed volume in pores smaller than a characteristic dimension (r_c), which is function of the system partial pressure, plus all the contributions from the adsorbed layers of thickness t onto the surfaces (S) of pores having larger dimension than r_c.

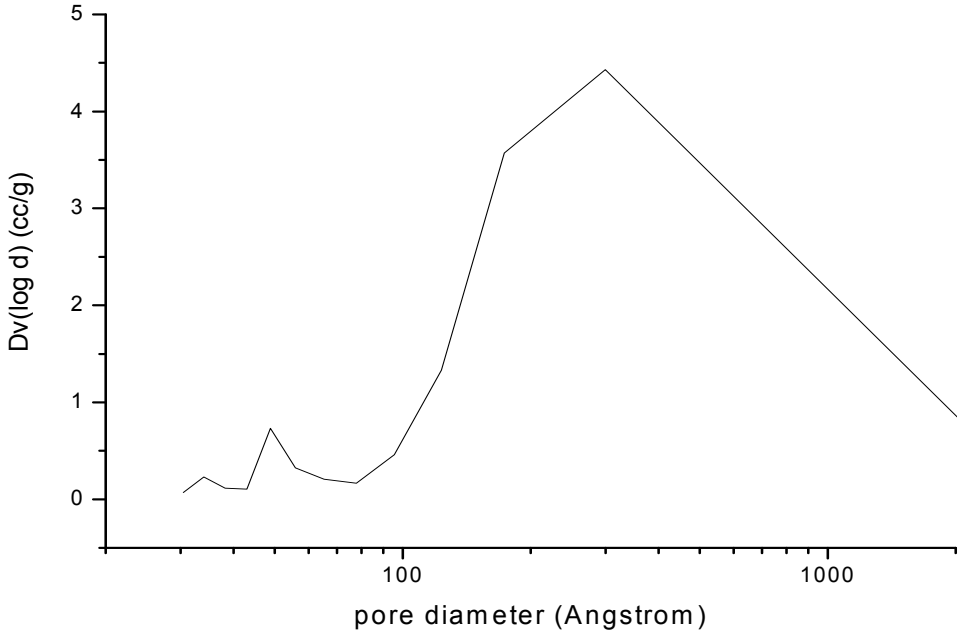

Figure 5: BJH model applied to the desorption branches of BET measurement for nanoporous silicon membranes.

An average pore diameter in the range of 7-30 nm was deduced from the desorption branches of isotherms applying BJH model (the Halsey model for the adsorption layer t was used).

Experimental set-up

In order to characterize biomolecules release and to study their diffusion, two different experimental set-up were designed.

Transwell system

The proposed experimental system envisages the uniaxial flow of biomolecules through the membrane nanopores. Nanoporous silicon membranes were glued with a polymeric solution onto commercial Transwell holders and then placed between two reservoirs. A fresh polymeric solution of PDMS, SylGard 184, was mixed in a 10:1 by weight percentage and degassed in a vacuum oven for 30 minutes was used to glue silicon membranes to the Transwell support. The membrane separates an initially filled biomolecules-containing reservoir from a water solution environment where biomolecules are depleted. The volume above the membranes was filled with a fluorescent macromolecules solution, whereas the lower volume contained bi-distillated water.

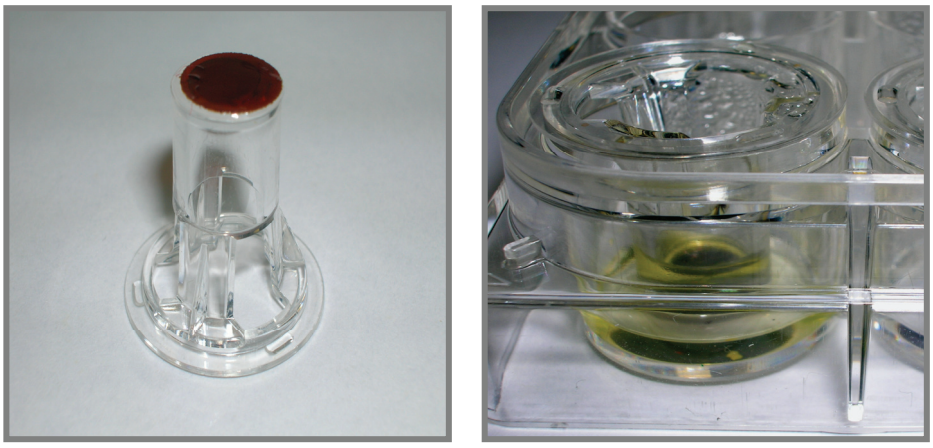

Figure 6: Left: Nanoporous silicon membrane glued on top of a Transwell system. Right: Experimental set-up of a fluorescent solution loaded on top of a membrane that releases in the lower volume.

Both volumes were monitored by time to register macromolecules concentration time variations due to the occurring permeation process.

Diffusion cell

In order to overcome evaporation and prevent diffusion layer formation a diffusion cell was specifically designed to properly perform permeation measurements. The cell was designed as a closed system to better control concentration parameters and solution volume amount. Both reservoirs are much larger compared to the one used for the Transwell system and this permitted the infinite tank assumption. It could also be assumed constant concentration in the upstream reservoir equal to the feed concentration.

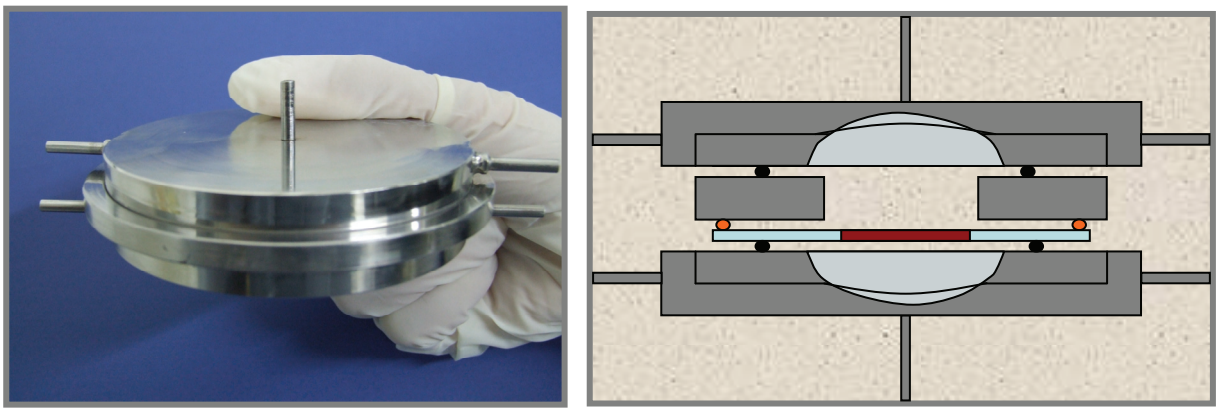

Figure 7: Left picture of a custom made diffusion cell. Right: Cross section of a diffusion cell, in red a membrane.

Diffusion layer formation could be discarded as a tangential flux was provided in both chambers. In order to reduce mechanical stress into the membranes' structure they were

glued onto polypropylene support discs of 3mm internal diameter and 4 mm external diameter. Every gluing operation had to be accomplished right after the membrane fabrication in order to give mechanical stability to the fabricated system. The supporting disc glued to the nanoporous membranes were then glued with cyanoacrylate onto a wider supporting disc to fit the chamber dimension. The holding system was then mounted between two O-rings in the middle of the diffusion chamber, and tested against any liquid leakage before measurements' running. The diffusion cell was connected by Teflon piping to the two reservoirs.

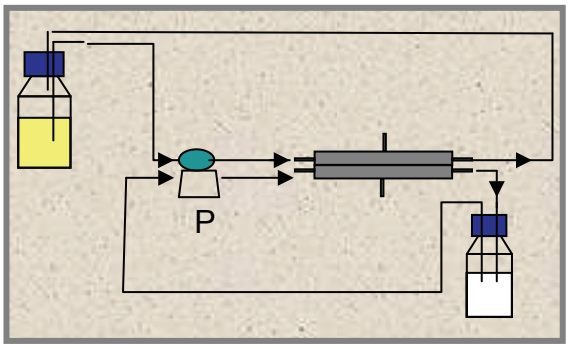

Figure 8: Schematic representation of the experimental set-up of diffusion cell and connection to reservoirs.

A peristaltic pump drew liquid from the upstream reservoir and sent it to the upside of the chamber, from where it went back to the reservoir. The same pump also drew water from the downstream reservoir and sent it to the lower side of the diffusion chamber from where it was redirected to the downstream reservoir. As a result, the two volumes were separated by the membrane which was watertight fixed in the middle of the chamber. The volume above the membrane was filled with a fluorescent macromolecule solution, whereas the lower volume contained bi-distillated water. Both volumes were monitored by time to register macromolecules concentration time variations due to the occurring permeation process.

Conclusions

A method was demonstrated to manufacture nanoporous silicon membranes. Two different experimental set-up were designed to perform biomolecules permeation studies in nanoporous membranes.

References

1. Gong D. Yadavalli V., Paulose M., Pishko M., Grimes C.A, “Controlled molecular release using nanoporous alumina capsules”, *Biomedical Microdevices* **5:1**, 75–80, (2003)
2. Desai T. A.,. Hansford D. J, Kulinsky L., Nashat A.H, Rasi G, Tu J, Wang Y, Zhang M. Ferrari M.” Nanopore Technology for Biomedical Applications” *Biomedical Microdevices* **2:1**, 11-40, (1999)
3. Tong H D, Jansen H V, Gadgil V J, Bostan C G,. Berenschot J W, van Rijn C J M, Elwenspoek M C,. “Silicon nitride nanosieve membrane” *Nanoletters* **4:2**, 283-287, (2004)
4. Unnikrishnan S., Jansen H., Berenschot E., Elwenspoek M., “Wafer scale nano-membranes supported on a silicon microsieve using thin-film transfer technology”, *Journal of Micromechanics and Microengineering* **18**, 064005, (2008)
5. Canham LT.. “Silicon quantum wire array fabrication by electrochemical and chemical dissolution of wafers”. *Applied Physics Letters* **57**:1046–1048, (1990)
6. Canham LT.. “Bioactive silicon structure fabrication through nanoetching techniques”. *Advanced Materials* **7,** 1033–1037, (1995)
7. Striemer C.C, Gaborski T.R., McGrath J. L, Fauchet P. M., “ Charge- and size-based separation of macromolecules using ultrathin silicon membranes”. *Nature Letters* **445**, 15, 749 (2007)
8. Halimaoui A.. “Porous silicon: Material processing, properties and applications”. In: Vial JC, Derrien J, editors. *Porous silicon science and technology*. France: Springer-Verlag. pp 33–52. (1995)
9. Levy-Clement C. “Characteristics of porous n-type silicon obtained by photoelectrochemical etching”. In: Vial JC, Derrien J, editors. *Porous silicon science and technology*. France: Springer-Verlag. pp 329–344. (1995)
10. Canham LT, editor. “Properties of porous silicon”. EMIS Datareview series No 18. London: INSPEC. (Chapter 1), (2005)
11. Cullis AG, Canham LT, Calcott PDJ.. “The structural and luminescence properties or porous silicon”. *Journal of Applied Physics* **82**, 909–965. (1997)
12. Salonen J, Bjorkqvist M, Laine E, Niinisto L. “Effects of fabrication parameters on porous p+ type silicon morphology” *Physics of State Solid* (a) 182:249–254. (2000)

13. A. Salonen, A. M. Kaukonen, J. Hirvonen, V.-P. Letho, ”Mesoporous Silicon in Drug Delivery Applications” *JOURNAL OF PHARMACEUTICAL SCIENCES*, **97**, 2, (2008)
14. Gregg S. J., Sing K. S. W. “Adsorption, surface area and porosity” 2nd edition. Academic Press, New York, (1982)

CHAPTER 4

Investigations of molecular permeability properties in nanoporous membranes

An understanding of the equilibrium and transport properties of macromolecules in porous media is important in the design of controlled release devices for the delivery of drugs, in dialysis and other membrane separations technique. As we have already mentioned, when the size of solute is comparable to the pore size through which it is diffusing, the effective diffusion coefficient of a solute within a pore is usually found to be less than its bulk value. Efforts to study this phenomena from a macroscopic view point has been ongoing for several decades. We first present a brief resume of the most citied results from literature and then we will show our findings, in both experimental set-up investigated, which are permeation across membranes on Transwell and permeability studies in diffusion cell.

Theoretical aspects of molecules permeation through membranes

Molecules permeation through membranes has been investigated fro many years. In general, the membrane is treated as an array of cylindrical pores and the solute is assumed to have both Brownian dynamics and hydrodynamic characteristics. For spherical solutes in bulk solution, this leads to the Stokes Einstein equation:

$$D = \frac{K_B T}{\zeta} = \frac{K_B T}{6\pi\mu r} \tag{1}$$

already introduced in chapter 2, where D is the bulk solution diffusion coefficient, K_B is Boltzmann's constant, T is the absolute temperature, ζ is the molecular friction coefficient in bulk solution, μ is the viscosity, and r is the radius of the solute.

The reduced solute diffusivity that is typically observed with macromolecular solutes in porous media results from two phenomena. One is thermodynamic and leads to an intrapore concentration driving force which is less than the driving force based on bulk solution concentrations. Steric and in some cases long range interactions between the solute and the pore wall exclude the solute from the region near the pore wall. This is described with an equilibrium partition coefficient K_{eq}, which is the ratio of the average solute concentration within the pore to that in the bulk solution at equilibrium. For a spherical solute in a cylindrical pore it is:

$$K_{eq}(\lambda) = \frac{\int_0^{1-\lambda} e^{-E(\beta)/K_B T}\,\beta d\beta}{\int_0^1 \beta d\beta} \tag{2}$$

In eq. 2 λ is the ratio of solute to pore size (r_s/r_p), b is the dimensionless radial position of the solute in the pore (r/r_p), and E is the interaction energy between the solute an the pore wall. The second effect is a transport effect. As the pore wall is really close to the solute, the hydrodynamic drug experienced by the solute in the pore is greater than the drug experienced in an unbounded fluid. This enhanced drag is characterized by K^{-1}, which is the ratio of the friction coefficient of the solute in the bulk solution to that within the pore:

$$K^{-1}(\lambda) = \frac{\int_0^{1-\lambda} [\zeta_{bulk}/\zeta(\lambda,\beta)] e^{-E(\beta)/K_B T}\,\beta d\beta}{\int_0^{1-\lambda} e^{-E(\beta)/K_B T}\,\beta d\beta} \tag{3}$$

where $\zeta(\lambda,\beta)$ is the molecular friction coefficient of solute of size l at position b in the pore. These two effects are combined to define the effective diffusion coefficient D[1]:

$$\frac{D(\lambda)}{D_{bulk}} = K_{eq} K^{-1} \tag{4}$$

In the case of E=0, which means that only steric interactions apply between the solute and the pore wall, the partitioning coefficient of eq. 2 becomes $K_{eq}=(1-\lambda)^2$. If we neglect the influence of the parameter b, which means that the distance from the pore wall does not play an important role on the value of the drug coefficient, it fallows $\zeta(\lambda,\beta)=\zeta(\lambda,0)$. The drug function $\zeta(\lambda,0)$ was calculated by algebraic stream function method [2]. Combining this two approximations leads to the commonly used Renkin equation[3]:

$$D = D_{bulk}(1-\lambda)^2(1-2.104\lambda+2.089\lambda^3-0.948\lambda^5) \tag{5}$$

In 1997 a better expression was found by Brenner and Gaydos using an asymptotic matching technique to account for the lateral position inside the pore to obtain $\zeta(\lambda,\beta)$[4]. Thus equation 5 becomes:

$$D = D_{bulk}(1+(9/8)\lambda\ln\lambda-1.54\lambda+O(\lambda)) \tag{6}$$

Experimental investigations have generally confirmed that the Renkin equation well describes the behaviour of spherical and rigid particles diffusing across a membrane. For instance in the work from Bohrer et al in 1984 they showed that ficoll and dextrans behaves differently[5]. Ficoll were quite well described by Renkin's equation whereas much more flexible molecules such as Dextrans evidently deviated from Renkin's predictions as is shown in figure 1.

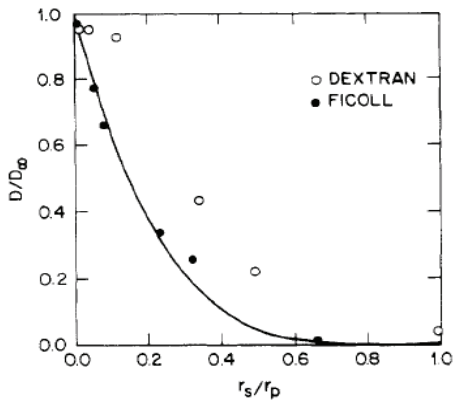

Figure 1: Experimental result of hindered diffusion coefficient to bulk value for Dextran and ficoll molecules in different membrane pore sizes obtained by Bohrer et al.[5]

The first efforts to understand macromolecules behavior in membranes permeations studies towards small pores were those from Cassassa in 1967[6]. In one of the earliest theoretical studies of the equilibrium partitioning of flexible macromolecules, Cassassa derived expressions for random flight polymer chains and calculated the partition

coefficient using a mathematical analogy to transient heat conduction. He continued his work later and derived also the expression for star-branched random flight chains[7]. Davidson et al. used Monte Carlo simulations to calculate partition coefficients for flexible polymers, including the effect of attractive interactions between chain segments and the pore wall in their model[8]. Results showed that small, attractive interaction energies between chain segments and the pore wall produced dramatic increases in the partition coefficient of chains with finite length. Davidson and Deen performed the analogous continuum ‘‘diffusion equation’’ calculation for the partition coefficient adding an attractive square well interaction[9]. Lin and Deen used a diffusion reaction equation to describe the effects of long-range polymer-pore wall interactions on the equilibrium partitioning coefficient[10]. Results were presented for square-well potentials, electrostatic double layer potentials, and van der Waals potentials. The intrapore hydrodynamic resistance for flexible polymers has been presented by Davidson and Deen (1988a)[11]. The hydrodynamic resistance for a flexible polymer is predicted to be less than that of a rigid sphere with the same λ, when the Stokes-Einstein radius is used to characterize the size of the flexible polymer. However, the effective diffusion coefficient is predicted to be smaller for a flexible macromolecule than for a rigid sphere because the equilibrium partition coefficient is sufficiently smaller for the flexible molecule.

Experimental investigations with flexible macromolecules have yielded mixed results. Diffusion coefficient values of linear polystyrene measured in Nuclepore polycarbonate membranes by Cannell and Rondelez were in close agreement with the theory of Davidson and Deen for random coil polymers. A later study by Davidson and Deen (1988b) also showed large diffusivities for Dextran and polyethylene glycol than those predicted for either spherical solutes or random coil polymers[12]. Diffusion coefficient values for polyisoprene measured by Bohrer et al [13]and for polyethylene oxide, and polyvinylpyrrolidone measured by Davidson and Deen were also larger than values predicted from their theory of 1988a.

DIFFUSION STUDIES IN POROUS SILICON

Recently due to the increasing interest in nanotechnology fabrication processes and their engineering applications, molecular permeation through nanoporous media has gained new interest .Many experimental works have been performed using nanoporous membranes. In 2002, Leoni et al. reported quite extensively on the characterization of

diffusion properties and tissue effects of nanoporous silicon membranes produced by the microfabrication methods[14-16]. They used three different size molecules: glucose, human albumin, and immunoglobulin (IgG) in order to study the effects of pore size for immunoisolation. Diffusion of the molecules through membranes was determined in vitro with four pore sizes: 7, 13, 20, and 49 nm. The diffusion coefficients were compared to the free diffusion in water. It was found that when the pore size approaches several times the molecular dimensions, the rate of diffusion starts to deviate from the values predicted by Fick's law. Although the membranes did not provide complete immunoisolation[17], it was observed that IgG diffusion was greatly hindered for all the pore sizes examined. Compared to glucose and albumin, the relative diffusion coefficient of IgG was several orders of magnitude lower.

Martin et al. extended the idea of using nanoporous silicon membranes to the control of drug delivery. They studied the release of 125I-labelled bovine serum albumin (BSA) and human recombinant interferon. In the in vitro studies both the compounds showed almost constant release rates (zero-order kinetics).

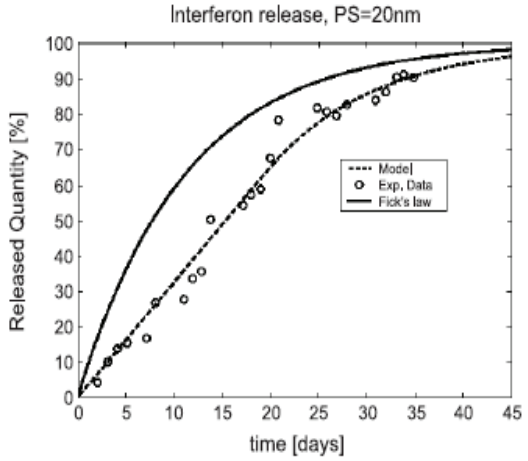

Figure 2: Experimental results of interferon release trough 20 nm pore membranes. [18].

For example in the case of a capsule with 20 nm membrane, Interferon was constant up to 20 days (fig. 2) and with a 13-nm membrane, BSA release rate was constant up to 60 days, clearly deviating from the Fick's law[18]. These findings were discussed through a macroscopic model which basically replaces into the Stokes-Einstein relation the van der Waals equation that accounts for non-ideal gases (fluids)[19-20] using a mathematical treatment for a generalized diffusion equation developed in [21]. Though the macroscopic model derived well described the experimental results, we believe that the mathematical treatment applies weakly to the physical problem discussed.

Permeability studies in Transwell

METHODS

The proposed experimental system envisages the uniaxial flow of biomolecules through the membrane nanochannels. The membrane separates an initially filled biomolecules-containing reservoir from a water solution environment where biomolecules are depleted. The volume above the membranes was filled with a fluorescent Dextrans-FITC macromolecules solution, whereas the lower volume contained bi-distillated water. Dextrans concentration in the lower reservoir was measured by means of a Spectrofluorimeter (485-535 nm). Two different molecular weights have been used (10kDa and 500kDa) at two different concentrations (0.1 and 0.2 mg/ml for 10kDa MW and 0.1 and 0.2 mg/ml for 500kDa MW). Measurements were carried out every two days on average. The two MWs taken into account have been chosen as they both have hydrodynamic radius of about the same order of dimension as the membranes pores.

RESULTS

Release measurements showed that the 10kDa Dextran at 0.1mg/ml concentration permeated the silicon membrane and that in 700 hours a value of C/C_{eq} up to 80% was reached (see Figure 3).

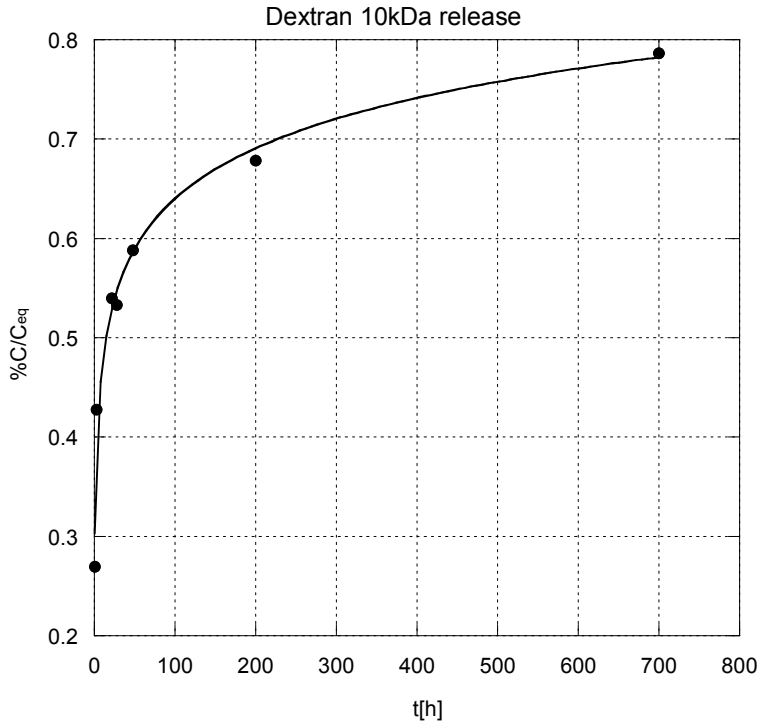

Figure 3: Dextran-FITC 10kDa release from Transwell over time. Dots are experimental values, line works as an eye-guide.

Probe	**Dextran 10kDa**		**Dextran 500kDa**	
Concentration (mg/ml)	0.1	0.2	0.1	0.2
Released Amount (% C/Ceq)	0.6 (7 days)	0 1 month	0.2 (7 days)	0 (7 days)

Table 1. Summary of the release results of 10kDa and 500kDa Dextrans from Transwell devices at two different initial concentrations.

A mutual diffusion coefficient can be derived from release data shown in Fig.3. Under the hypothesis of constant concentration in the reservoir, and neglecting both evaporation effects and effects due to the presence of a diffusion boundary layer, a mass balance can be applied to the uniaxial system described above. Pore geometry was assumed straight and cylindrical, and the number of pores was derived from BET data. The mass balance which applies under the assumption of quasi-stationary process [4] is reported below (eq. 7):

$$\ln\left[1 - C(t)/C(\infty)\right] = -\left(DnA_p / L\right) \times \left(1/V_1 + 1/V_2\right)t \quad (7)$$

where C(t) is the Dextran concentration in the lower reservoir at a time t, C(∞) is the equilibrium concentration of the system, D is the Dextran effective diffusion coefficient in the pores, n the number of pores, A_p and L are the membrane's section and thickness respectively, V_1 and V_2 are the reservoir's volumes.

The diffusion coefficient derived is equal to 5E-12 cm^2/s. As the bulk diffusion coefficient is about 9E-7 cm^2/s, it follows that mobility inside the pores is strictly reduced, though this coefficient includes both hydrodynamic reduction due to the increase in the drug factor and partitioning due to steric exclusion.

Permeability studies in Diffusion Cell

METHODS

In order to overcome evaporation and prevent diffusion layer formation a diffusion cell was specifically designed to properly perform permeation measurements. In this scenario membranes were glued onto plastic support discs and placed in between two O-rings. The holding system was then mounted between two chambers. Each volume was stirred by means of a tangential flux. Experiments were carried out taking advantage of low concentration, 0.1mg/ml, 10kDa Dextrans-FITC. Permeated concentration was measured by means of a Spectruofluorimeter previously calibrated.

RESULTS

In order to better describe the permeation process a diffusion cell equipment was designed. The results found for this experimental set-up are shown in Figure 4. Lag time of the permeation process was about 150 hours. The diffusion coefficient in an experiment of permeation can be derived from (Eq. 2):

$$t_D = \frac{L^2}{6D} \quad (8)$$

where t_D represents the characteristics time lag of the permeation process. From Equation 8, a diffusion coefficient of about 2E-12 cm^2/s was derived. This value is about the same order of magnitude as the value reported in a Transwell release experiments. Although many membranes were tested, only a few survived the long time needed to follow a complete release kinetic. This could be due to the mechanical stress induced in the thin nanoporous membrane because of the presence of the peristaltic pump needed for system agitation. In order to improve the experimental apparatus, It might be necessary to obtain solute agitation in a different way. Mechanical stress could be reduced by the addition of a metallic filter with mesh size in the millimetre range, though this would need the modification of the diffusion chamber dimensions.

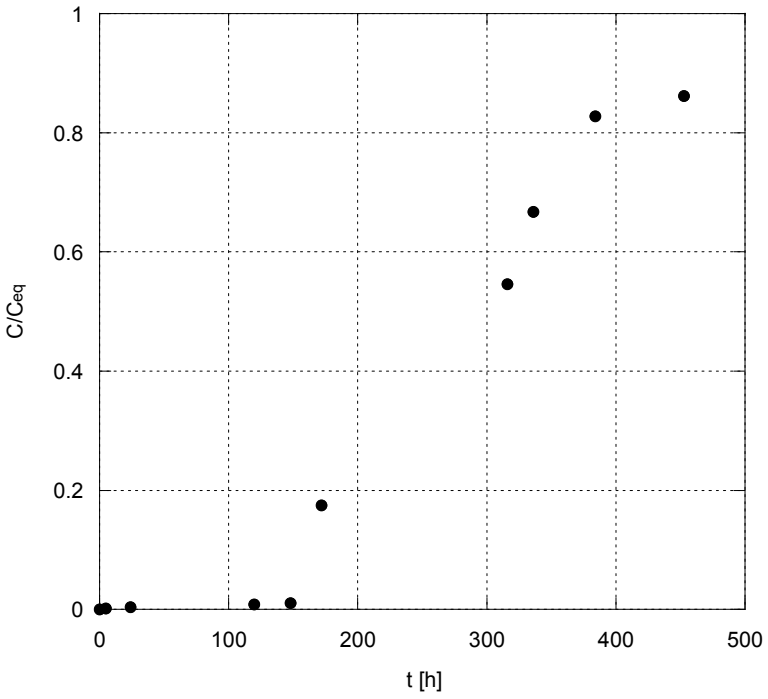

Figure 4. Dextran-FITC 10kDa permeation in a diffusion cell.

Conclusions

Nano porous silicon (PS) membranes have been used to study the release characteristics of biomolecules through nanochannels. The release of biomolecules from nanoporous membranes results to be deeply affected by material microstructure parameters, as well as molecular chemistry and concentration. Hindered diffusion was shown for Dextran 10kDa

with a decrease of about four orders of magnitude in the diffusion though the measured coefficient includes both hydrodynamic reduction due to the increase in the drug factor and partitioning due to steric exclusion.

These findings claim a dipper insight into transport phenomena through nanochannels in order to better design a drug delivery systems.

References

1. Shao J. and R. E. Baltus **"**Hindered Diffusion of Dextran and Polyethylene Glycol in Porous Membranes" *AIChE Journal. **46,*** 6 , 1149 (2000)
2. Haberman W.L., Sayre R.M., "Motion of rigid and fluid spheres in stationary and moving liquids inside cylindrical tubes" David Taylor Model Basin Report N°1143 US Navy Department Washington D.C (1958)
3. Renkin, E. M., ''Filtration, Diffusion, and Molecular Sieving through Porous Cellulose Membranes,'' *Journal Gen. Physiology*, **38**, 225, (1954)
4. Brenner, H., and L. J. Gaydos, ''The Constrained Brownian Movement of Spherical Particles in Cylindrical Pores of Comparable Radius, Models of the Diffusion and Conventive Transport of Solute Molecules in Membranes and Porous Media,'' *J. Colloid Interface Science*, **58**, 3121 (1977)
5. Bohrer, M. P., G. D. Patterson, and P. J. Carroll, ''Hindered Diffusion of Dextran and Ficoll in Microporous Membranes,'' *Macromolecules.*, **17**, 1170, (1984)
6. Casassa, E. F., ''Equilibrium Distribution of Flexible Polymer Chains Between a Macroscopic Solution Phase and Small Voids,'' *Journal of Polymer Science: Part B: Polymer Physics*, **5**, 773, (1967)
7. Casassa, E. F., and Y. Tagami, ''An Equilibrium Theory for Exclusion Chromatography of Branched and Linear Polymer Chains,'' *Macromolecules.*, **2**, 141, (1969)
8. Davidson, M. G., U. W. Suter, and W. M. Deen, ''Equilibrium Partitioning of Flexible Macromolecules Between Bulk Solution and Cylindrical Pores,'' *Macromolecules.*, **20**, 1141 (1987)
9. Davidson, M. G., and W. M. Deen, ''Equilibrium Partitioning of Long-Chain Polymers Between Bulk Solution and Pores in the Presence of Short-Range Attractions,'' *Journal of Polymer Science: Part B: Polymer Physics*, **28**, 2555, (1990)
10. Lin, N. P., and W. M. Deen, ''Effects of Long-Range Polymer-Pore Interactions on the Partitioning of Linear Polymers,'' *Macromolecules.*,**23**, 2947, (1990)
11. Davidson, M. G., and W. M. Deen, ''Hydrodynamic Theory for the Hindered Transport of Flexible Macromolecules in Porous Membranes,'' *Journal of. Membrane Science.*, **35**, 167 (1988a.)

12. Cannell, D. S., and F. Rondelez, ‘‘Diffusion of Polystyrenes through Microporous Membranes,’’ *Macromolecules.*, **13**, 1599, (1980)
13. Davidson, M. G., and W. M. Deen, ‘‘Hindered Diffusion of Water-Soluble Macromolecules in Membranes,’’ *Macromolecules.*, **21**, 3474, (1988b)
14. Bohrer, M. P., L. J. Fetters, N. Grizzuti, D. S. Pearson, and M. V. Tirrell, ‘‘Restricted Diffusion of Linear and Star-Branched Polyisoprenes in Porous Membranes,’’ *Macromolecules.*, **20**, 1827, (1987)
15. Desai TA, Hansford DJ, Kulinsky L, Nashat AH, Rasi G, Tu J, Wang Y, Zhang M, Ferreri M.. “Nanopore technology for biomedical applications” *Biomedical Microdevices* **2**:11–40. (1999)
16. Cohen MH, Melnik K, Boiarski AA, Ferrari M, Martin FJ.. “Microfabrication of silicon-based nanoporous particulates for medical applications”. *Biomedical Microdevices* **5**:253–259 (2003)
17. Leoni L, Boiarski A, Desai TA.. “Characterization of nanoporous membranes for immunoisolation: Diffusion properties and tissue effects”. *Biomedical Microdevices* **4**:131–139. (2002)
18. Martin F, Walczak R, Boiarski A, Cohen M, West T, Cosentino C, Ferrari M. “Tailoring width of microfabricated nanochannels to solute size can be used to control diffusion kinetics”. *Journal of Controlled Release* **102:**123–133. (2005)
19. Cosentino C., Amato F., Walczak R., Boiaraski A., Ferrari M., “Dynamic Model of Biomolecular Diffusion Through Two-Dimensional Nanochannels” *Journal Physical Chemistry B*, **109**, 7358 (2005)
20. Amato F, Cosentino C., S. Pricl, M. Ferrone, M. Fermeglia, M. Ming-ChengCheng, Walczak R Ferrari M “Multiscale modeling of protein transport in silicon membrane nanochannels. Part 2. From molecular parameters to a predictive continuum diffusion model” *Biomedical Microdevices* **8,** 4, (2006)
21. Peskir G., ‘‘On the Diffusion Coefficient: The Einstein Relation and Beyond” *Stochastic Models*, **19**, 383 (2003)
22. Salonen, A. M. Kaukonen, J. Hirvonen, V.-P. Letho, ”Mesoporous Silicon in Drug Delivery Applications” *JOURNAL OF PHARMACEUTICAL SCIENCES*, **97**, 2, (2008)

CHAPTER 5

Nanochannels fabrication and experimental set-up

Recently, science and engineering of molecular transport within nanofluidic channels, with critical dimensions of 10–100 nm, have drawn a lot of attention with the advances in micro - and nanofabrication techniques [1]. New applications have been created for separating and manipulating biomolecules with nanodevices. Nanometer scale channels have been used to separate DNA by entropic effects, and to study the kinetics of individual biological molecules with single molecule technique.[2-6]. It is therefore essential to understand the underlying physics and transport properties of highly confined macromolecules. Such knowledge will not only be important for the development of theoretical physics but also could help the design and optimization in future applications such as separations and drug delivery.[7]

The use of fluidics with micrometer to nanometer dimensions is in fact advantageous because it offers a means of examining biomolecules in their natural aqueous environments. Therefore, in addition to the various mentioned applications, nanofluidic channels are an ideal, well-controlled experimental platform to study nanoscale, fluidic or molecular transport properties[8]. Confined channels allow to affect the physics governing the behaviour of molecules in a precise manner turning out of being the ideal environment for the experimental single molecule investigations of molecular transport laws on nanoscale.

State of the art

Several nanochannel fabrication schemes can be found in literature. Most of them have employed top down lithographic methods. A common approach takes advantages of high resolution lithography and consist of etching nanoscale trenches in silicon or glass substrates. The trenches are then enclosed to make nanochannels by means of bonding to a cover glass [9-11]. Sacrificial etching layer techniques have been demonstrated to manufacture channels down to 50 nm[12].

Many fabrications have been accomplished also using Nanoimprint lithography (NIL). This technique has been developed to allow many devices to be created from a single template, and has resulted in channels that have been reduced to as small as 10 nm by taking advantage of deposited films for channel shrinking and sealing. The fundamental way that the channels are initially created is by creating an interference pattern using two beams from an argon laser (351 nm) on a photoresist[13]. With careful adjustment of the parameters this can create channels which are 100 nm across and together with nonuniform deposition techniques were used also to generate sealed nanochannels as small as 10 nm [14]. Because of the etching processes used, these methods tend to form channels with rectangular geometries, and it can be difficult to make narrow channels over large areas. In NIL, high resolution lithography is still typically required for the fabrication of the template.[12,14].

Another technique implies direct nanomachining using a Focus Ion Beam (FIB) tool. A FIB uses a beam of energetic ions such as Ga+ to sputter material away and is capable of resolution down to 20 nm and can etch down many microns in principle[13]. FIB lithography has been also demonstrated to manufacture 50 nm nanoslits[14]. There are some problems with this technique, such as implanting of the Ga+ ions in the substrate which can reduce the optical transmission of the substrate.

These techniques allow good flexibility in the possible shapes of the nanofluidic structures. However, they require relatively expensive nanolithography techniques to define their features[1].

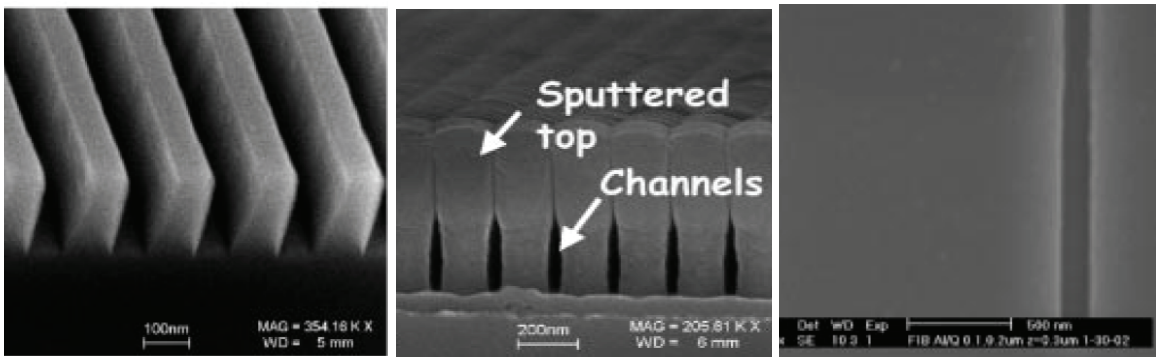

Figure 1: LEFT_Array of channels etched into quartz. The channel pattern was imprinted into a polymer which acted as a reactive ion etching (RIE) etch mask. MIDDLE_ Arrays of posts fabricated by Nanoimprinting Lithography and sealed by sputtering. RIGHT_ FIB-milled nanoslits in a 50-nm thick aluminum film. (a) 100-nm straight lines.

While one dimensional (1D) nanofluidic channels have been used to study the polymer dynamics in pseudo 1D nanochannels [15], zero order release kinetic was demonstrated in devices with nano-deep channels obtained from sacrificial etching layer technique [16], moreover the sorting, filtering, and manipulation of biomolecules require confinement only in one dimension[17]. Therefore, a more interesting fabrication process is to fabricate ‘‘shallow’’ channels, instead of ‘‘narrow’’ channels[1].

This technique has already been successfully applied to the separation of large DNA molecules[2] and it was first demonstrated for silicon substrates. A channel pattern is defined by photolithography on a silicon substrate and then etched for a short time (either by wet etching or reactive ion etching) to generate very shallow trenches. Then, anodic bonding is used to bond a flat Pyrex glass wafer to the silicon substrate with the help of high electric field (400-800 V across the junction) and heat (typically 300-400 °C). This technique eliminates the need of nanolithography to build nanofluidic structures, while allowing the well-defined flat nanochannels with good control on channel depth. The channel depth can be controlled by tuning etch time of the substrates, and the etch rate can also be slowed down (either by diluting wet etchant or de-optimizing the RIE conditions) to make the thickness control more precise. Also, nanochannels made by this method are much more robust mechanically.

While silicon is not suited for fluorescent applications because of high fluorescent background signal mainly shown in the 700-900 nm range Polydimethylsiloxane, (PDMS) is transparent in the visible and UV region, it is inexpensive compared to silicon, its manufacturing technique, as replica molding, are pretty simple to use, but its softness has been demonstrated to cause channels’ instability during sealing procedures. It has in fact

been demonstrated [18] that it was difficult to generate free standing channels down to 100nm even in h-PDMS which has three times higher modulus than Sylgard 184.

The technique described above was also successfully applied to the manufacturing process of glass-glass devices[1]. Glass-glass nanoslits have successfully been used for DNA transport properties studies in confined geometry[7].

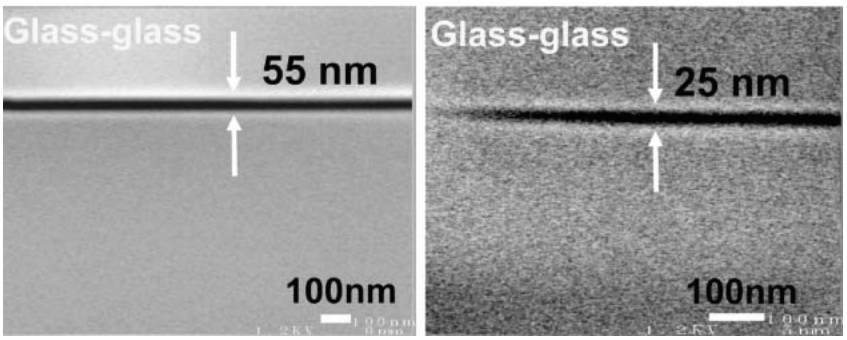

Figure 2: Cross-sectional SEM images of nanochannels with depths of 55 nm and 25 nm fabricated on glass substrate bonded with another glass cover.

The critical step in this manufacturing technique is the bonding process as due both to the strong electric field and to the high temperature employed, the nanochannel might sag causing a change in channel size. Usually, the low temperature bonding requires a rigorous cleaning procedure prior to bonding and the bonding strength is not so large as for high temperature bonding. Besides, the usage of adhesives or glue may clog the channels, especially for fabricating very shallow channels. In contrast to the low temperature bonding process, thermal fusion bonding at high temperature can provide good bonding strength and high bonding yield. Although glass–glass bonding at high temperature (around 600 °C for Pyrex) can be achieved successfully with large bonding strengths, the channels tend to be distorted and even collapse since the glass material at high temperature will be softened. Mao demonstrated the range of aspect ratio which could give good bonding results for the fusion bonding of glass-glass nanoslits[1,18]. Thus, it is important to maintain the proper aspect ratio which satisfy good bonding sealing conditions for the fabrication process of glass nanoslits.

Fabrication Process

In order to manufacture nanochannels to be used to conduct FCS measurements of molecular motion on the nanoscale we had to select materials compatible with fluorescent applications that could achieve good transparency and low background noise. Thus we focused our experimental work on glass substrates. We decided to fabricate shallow

nanofluidic channels as they do not require nanolithography techniques. We patterned both Pyrex and Borofloat samples as they both have high optical transmission in the visible as well as in the UV range. To this aim we took advantage of the white room facilities in ENEA, department of MatNano, Portici site, Napoli. We used both classic photolithography followed by wet etching and FIB lithography.

WET ETCHING

Materials

Glass wafers were cut by diamond cutting machine in samples of rectangular shape of 1cm x 2cm lenght, and washed with Deconex (1-2 %) DI at 80 °C for 1.30h in ultrasonic bath. Samples were rinsed in boiling acetone and isopropilic acid and spun dry with nitrogen gas. To improve the adhesion of the photoresist the samples were first wet coated with liquid HDMS. The substrates were then coated with S1818 positive resist, for 30s at 22 rpm and soft baked at 100°C for 10 minutes in an oven. The wafers were exposed by UV contact litograpghy for 13 s at 10 mW UV radiation. The exposed wafers were developed for 10 s in DE126, rinsed in DI water and spun dry in nitrogen gas. The resist layer thickness was measured to be 1.2 μm. The glass substrate were immersed in a BOE (Buffered Oxide Etchant) solution of ammonium florure and fluoridric acid 7:1, without agitation. The etched depth was measured by P10 Temcor Profilometer.

Results

Wet etching was an unsatisfactory way to manufacture nanodepth channels. Our resist did not survive more than 5-6 minutes of etching time. The patterned geometry turned out to be not homogenous after several minutes of etching time. Channels widened of about 10% their patterned size in the first 10 minutes of etching process. P10 measured profiles were point dependent as there was more than 50 % variability in channel depth respect to the starting position of the measurements. On average we could achieve 2.2 μm of etched depth in 10 minutes.

FOCUS ION BEAM LITOGRAPHY

Materials

Borofloat samples were washed and cut as described previously. Before positioning in the FIB machine they were glued to a sample holder by silver paste coating on the wafer

edges. The FIB body was vacuum aspirated after holder positioning. Magnification necessary for micromachining were about 800X. Ionic current was set to 20 nA at 30kV.

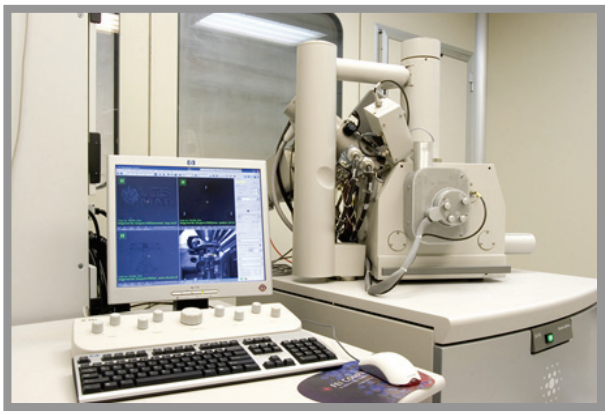

Figure 3: FIB apparatus used in ENEA, Portici, Naples.

Results

We could satisfactory manufacture different channel depths of 100, 50, 40 e 30 nm. Resolution of less than 25 nm was not achieved. An important parameter was found to be aspect ratio of channel width versus channel depth. Several samples of 500 μm length, 30 μm width and 30 or 40 nm depth were manufactured.

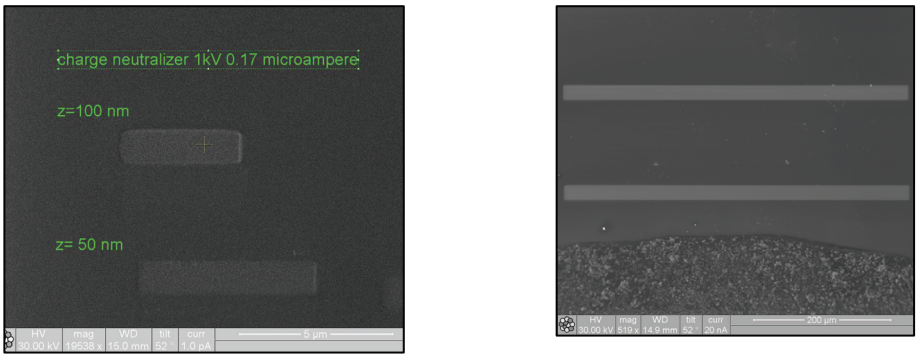

Figure 4: SEM pictures of FIB etched channels, depths of 50 and 100 nm.

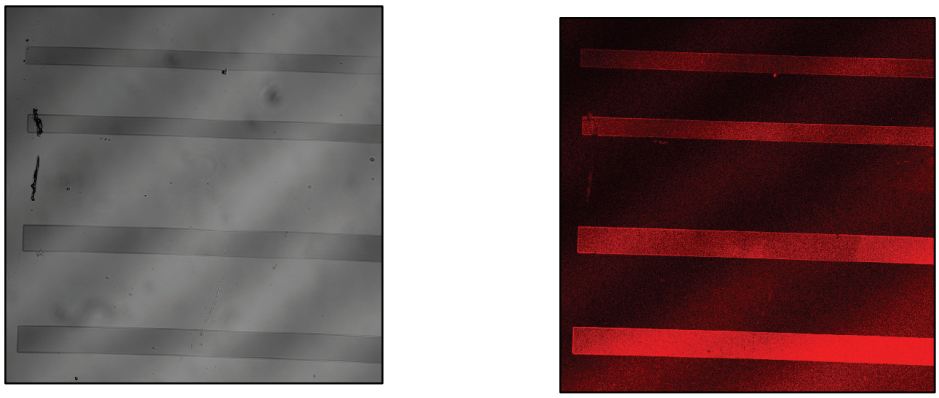

Figure 5: Confocal images of FIB etched channels, depth of 30 and 40 nm, width 20 and 30 microns. On the left transmission image, on the right Rhod6G covered sample. Exc 543 nm, LP 570 nm.

The etched channels had to be enclosed by anodic or fusion bonding to another Borosilicate glass wafers and macro holes were needed in order to load the macromolecule solution into the shallow channel. We bore macro holes through the glass wafers thanks to a glass drill bit of diameter 3 mm. We did not owned the proper machinery and expertise to perform the fusion bonding between the glass wafers. As our mainly aim was not to develop such an expertise in this nanotechnology field but to evaluate diffusion properties of molecules in confined geometry, we choose to look for an external company in order to perform the bonding, and decided to collaborate with Micronit Microfluidics [19].

Design of the chip

Together with Micronit Microfluidics engineers we designed our own chip to fulfil our requirements. Starting from the concept design represented below, we agreed to perform powder blasting to obtain the holes, wet etching to manufacture the nanochannels and direct bonding between the wafers.

Schematic chip representation

TOP LAYER			Size	Tolerance
Material	D263 glass	Thickness	1.1 mm	+/-0.1mm
Holes	Powderblasting	Large diameter	1700µm	+/- 100µm
		Small diameter	600µm	+/- 125µm
Channels	Etching	Depth	50µm	+/- 2µm
		Width	~6mm	
		Length	~15mm	
Channels	Etching	Depth	30nm	
		Width	30µm	
		Length	500µm	

BOTTOM LAYER			Size	Tolerance
Material	D263 glass	Thickness	145µm	+/-0.15µm

BONDING		Size	Tolerance

Method	Direct	Alignment accuracy		

DICING				
Method	Breaking	Chip Width	15mm	+/-300 μm
		Chip Length	45mm	+/-300 μm

Table 1: Work parameters established by Micronit engineers

We fallowed the experimental work of Mao [1] to set channels' dimensions as reported in the table 2 below.

width μm / depth nm	2	5	10	30
10	(C)	x	x	(D)
20	(C)	x	x	(D)
30	(C)	x	x	x

Table 2: Set of a nanoslit dimensions manufactured.

The combinations represented by (C) or (D) were supposed to have high risk of collapse while every combination was successfully manufactured. Channels were then manufactured 500 μm long, 2, 5, 10 and 30 μm wide and in three different depths 10, 20 and 30 nm. The nanochannels were manufactured as two arrays of 10 each with a pitch of 70 μm for all channel width, but for the 30 μm width where the pitch needed was 100 μm. The nanochannels are placed in between two 50 microns depth reservoir with width and length of 6 and 15 mm respectively. We decided to keep the commercial mask for the powderblasting process and not to use 6 out of the 10 holes manufactured in this way. Both inlet and outlet of the two macroscopic reservoir start from the four useful holes placed on one side of the chip. The final design of the chip is represented below in figure 6.

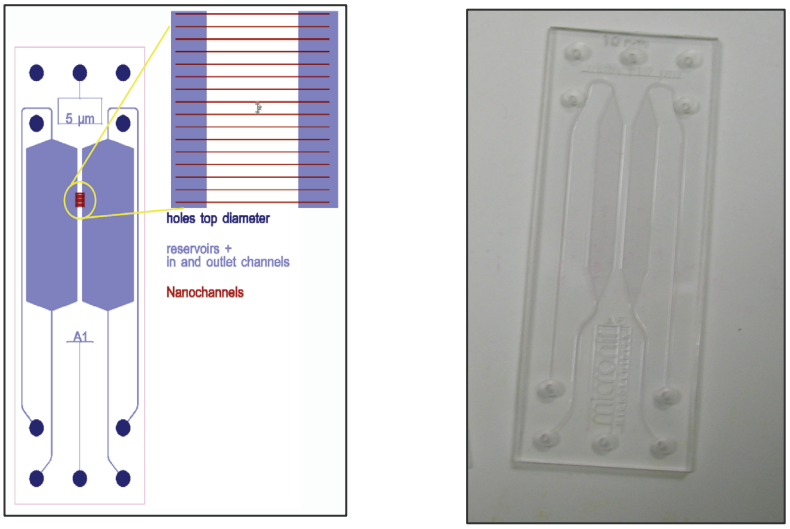

Figure 6: Left_ chip layout cartoon. Right_ chip picture.

In order to handle the glass chips we developed also a chipholder. The design was carried out taking into account the microscope stage dimension. In fact the chip holder together with the glass chip had to fit the microscope stage and the nanochannels had to be in a position suitable for the imaging.

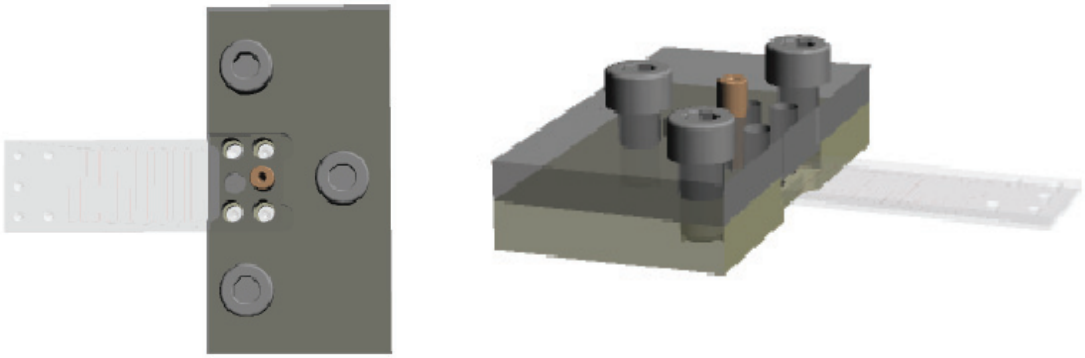

Figure 7: Project design of the chipholder.

In the previous figure there are shown two preliminary design of the system. The chipholder was manufactured in stainless steel with the bottom part in PEEK (Polyetheretherketone) thus to reduce mechanical stress to the glass chip. In order to place the chip on top of the objective in an accurate horizontal way, we changed the design adding an external tongue parallel to the chip as shown in figure 8..

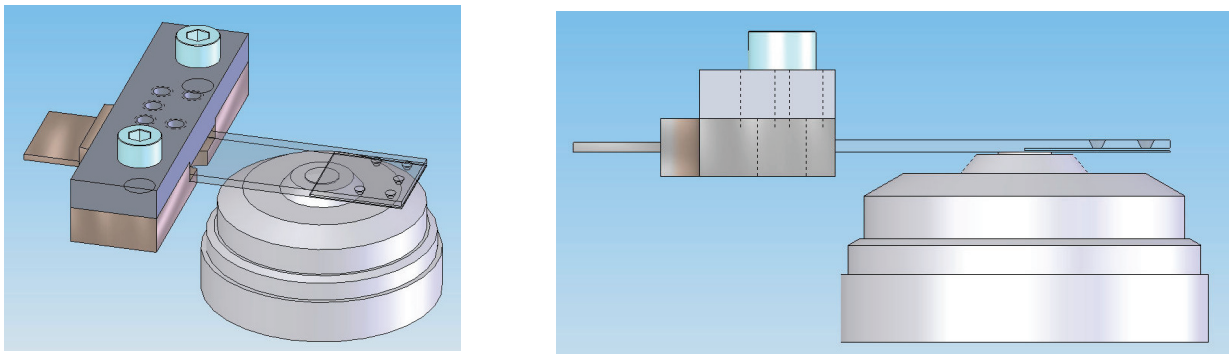

Figure 8: Project design of the chipholder with the external tongue.

The actual shape was modified afterwards to fit also LEICA microscopes' stages. A picture of the final system used is represented in figure 9.

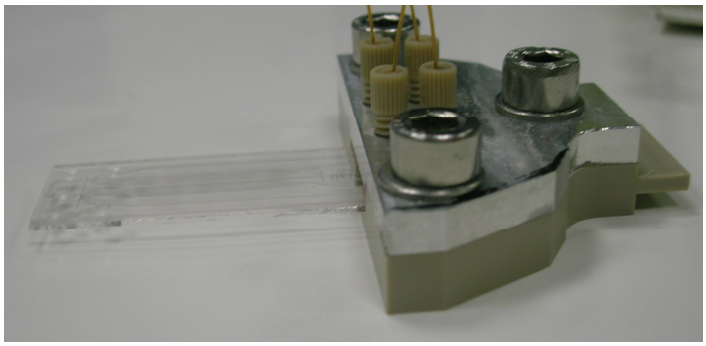

Figure 9: Picture of the chipholder in its final shape.

In order to load the fluidic solution four Nanoport inlets/ outlets perfectly suited for low dead volume applications and small chip volumes are arranged on the holder. These connections fit fused silica capillaries (375 µm OD, 150 µm ID, Polymicro) and small ferrules to be lodged at the capillaries ends made sure leak tight connections with the chip.

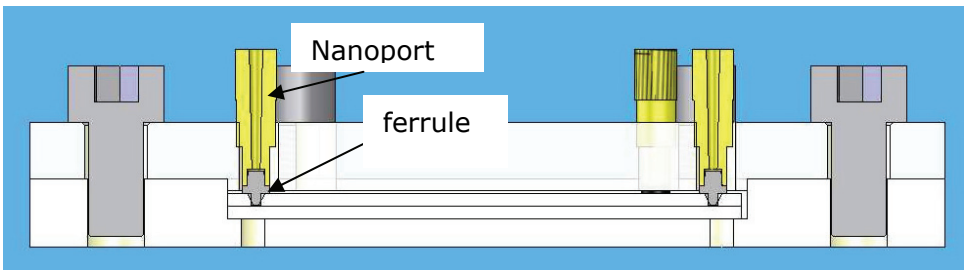

Figure 10: Cross section of the system to show fluidic connections.

At the other edge of the fused silica capillaries we have disposed other fluidic connections to be able to flush the experimental solution. We used syringe with a PEEK tubing connector from ILS microsyringes (5, 10 ml). These syringes are equipped with a 1/4 x 28" female flat bottom connector. In order to be able to attach the 360 µm O.D. fused silica capillary to the syringe a flat bottom nut (LT-115, Upchurch), a ferrule (P-250, Upchurch) and a tubing sleeve (F-242, Upchurch) were used. The tubing sleeve allows the capillaries to be used in an otherwise 1/16" port. The final apparatus is shown in fig. 11.

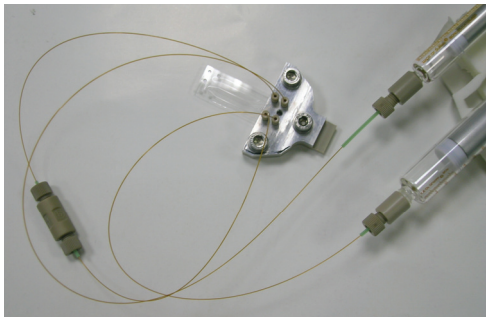

Figure 11: Picture of the experimental apparatus, a chip in the chipholder, fluidic connections.

Experimental set-up

Nanochannels were placed in the chipholder and all the fluidic connections were properly set. The chip was then connected by PEEK connectors to a syringe filled with nanomolar Rodhamine6g molecule solution. A small pressure was applied and the solution was sucked into the channels. Then the connectors were closed and solution let to equilibrate overnight. The channels were imaged in the red channel on a LEICA SP2 system with 63X water lens objective to control channels dimension and loading.

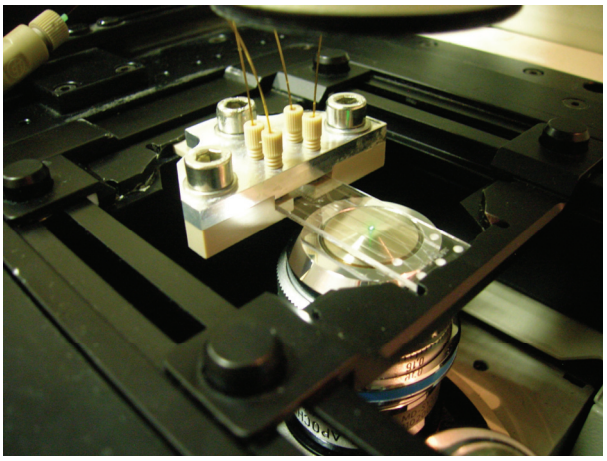

Figure 12: Nanochannels placed on top of 40X objective of a confocal microscope.

The intensity signal from the channels was uniform. None of the channels was collapsed.

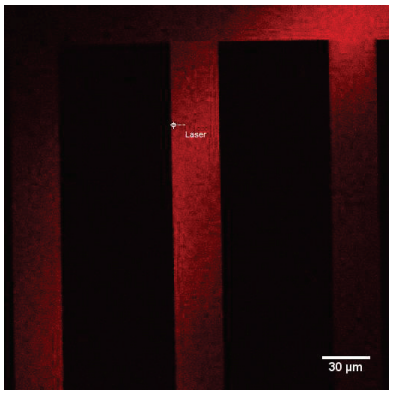

Figure 13: Confocal micrographs of 30 μm wide, 30 nm depth nanoslits loaded with Rh6G solution_: xy view.

Conclusions

Nanochannels can affect the physical behaviour of molecules under well-controlled confinement, thus they are the experimental apparatus required for single molecule observations of molecular motion under confinement. Nanochannels were successfully designed. After loading with a solution of fluorescent molecules and imaged they showed uniform fluorescent signal.

References

1. P. Mao and J. Han," Fabrication and characterization of 20 nm planar nanofluidic channels by channels by glass–glass and glass–silicon bonding" *Lab on a Chip*, **5**, 837–844, (2005)
2. J. Han and H. G. Craighead, "Separation of long DNA molecules in a microfabricated entropic trap array", *Science* **288**, 1026 (2000);
3. L. R. Huang, J. O. Tegenfeldt, J.J Kraeft, J. C Sturm, R. H. Austin, E. C. Cox, "A DNA prism for high-speed continuous fractionation of large DNA molecules" *Nature Biotechnology*. **20**, 1048 (2002)
4. O. A.Saleh and L. L. Sohn, " An artificial nanopores for molecular sensing" *Nano Letter*s. **3**, 37 (2003)
5. S. S. Verbridge J. B. Edel, S. M. Stavis, J. M. Moran-Mirabal, S. D. Allen, G. Coates, H. G. Craighead "Suspended glass nanochannels coupled with microstructures for single molecule detection" *JOURNAL OF APPLIED PHYSICS* **97**, 124317 (2005)
6. J. Fu, R. B. Schoch, A. L. Stevens, S. R. Tannenbaum, J. Han, "A patterned anisotropic nanofluidic sieving structure for continuous-flow separation of DNA and proteins" *Nature Nanotechnology* **2**, 121 (2007).
7. C. Hsieh, A. Balducci, and P. S. Doyle "An Experimental Study of DNA Rotational Relaxation Time in Nanoslits" *Macromolecules* **40,** 5196-5205, (2007)
8. S. J. Kim, Y. Wang, J. H. Lee, H. Jang, J. Han "Concentration Polarization and Nonlinear Electrokinetic Flow near a Nanofluidic Channel", *PHYSICAL REVIEW LETTERS,* **99**, 044501 (2007)
9. M. Stavis, J. B. Edel, K. Samiee, and H. G. Craighead," Single molecule studies of quantum dot conjugates in a submicrometer fluidic channel" *Lab-On-a-Chip* **5**, 337 (2005)
10. .M. Stavis, J. B. Edel, K. T. Samiee, D. Luo, and H. G. Craighead, "Detection and identification of nucleic acid engineered fluorescent labels in submicrometre fluidic channels" *Nanotechnology* **16**, 5314 (2005).
11. J. O. Tegenfeldt, C. Prinz, H. Cao, R. L. Huang, R. H. Austin, S. Y. Chou, E. C. Cox, and J. C. Sturm, *Analytical and Bioanalytical Chemistry*. **378**, 1678 (2004)

12. S. W. Turner, A. M. Perez, A. Lopez and H. G. Craighead, " Monolithic nanofluid sieving structures for DNA manipulation" *Journal of. Vacuum Science and Technology B: Microelectronics*, **16**, 3835. (1998)
13. R. H. Austin, J. O. Tegenfeldt, H. Cao, S. Y. Chou, and E. C. Cox "Scanning the Controls: Genomics and Nanotechnology" *IEEE TRANSACTIONS ON NANOTECHNOLOGY*, **1**, 1, (2002)
14. H. Cao, Z. Yu, J. Wang, J. O. Tegenfeldt, R. H. Austin, E. Chen, W. Wu and S. Y. Chou, " Fabrication of 10 nm enclosed nanofluidic channels" *Applied Physics Letters*, **81**, 174, (2002)
15. J. O. Tegenfeldt, C. Prinz, H. Cao, S. Chou, W. W. Reisner, R. Riehn, Y. M. Wang, E. C. Cox, J. C. Sturm, P. Silberzan and R. H. Austin, " The dynamics of genomic length DNA molecules in 100 nm channels" *Proceeding of the National Academy of Sciences U.S.A*., **101**, 10979, (2004)
16. Desai T. A.,. Hansford D. J, Kulinsky L., Nashat A.H, Rasi G, Tu J, Wang Y, Zhang M. Ferrari M." Nanopore Technology for Biomedical Applications" *Biomedical Microdevices* **2:1**, 11-40, (1999)
17. .J R. Webster, M. A. Burns, D. T. Burke and C. H. Mastrangelo, " Monolithic Capillary Electrophoresis Device with integrated fluorescent detector" *Analytical Chemistry* , **73**, 1622. (2001)
18. P. Mao, *Thesis dissertation* " Fabrication and characterization of nanofluidic channels for studying molecular dynamics in confined environment" MIT (2005)
19. www.micronit.com

CHAPTER 6

Fluorescence Correlation Spectroscopy measurements in nanochannels

The understanding of molecular motion in confined environments is definitely a scientific challenge which need to be overcome to better design and optimize nanodevices to be used in different applications.

Willing to investigate molecular physical properties on the nanoscale, there is the need to overcome the drawback of nano dimensions thus classical microscopy can not be used. Though nanoscopy has already been proved, it is still somehow not affordable[1]. A possibility to study the nanoscale is to perform FCS, a well established technique widely used for measuring macromolecules properties and interactions both in vitro and in vivo; it measures fluorescence intensity fluctuations of few fluorochrome molecules in an illuminated volume smaller then a femtonliter. Due to Brownian motion molecules go across the observation volume giving rise to fluorescence fluctuations, and through a time correlation analysis of the intensity fluctuations, molecule hydrodynamic properties of single molecules are then accessible. Though usually applied to bulk measurements or to investigations in cellular environment, It has also been used as a tool for velocity measurements in microfluidics and recentely it has been demonstrated has a detection tool for molecular motion in micrometric and submicrometric structures[2]. We have applied this technique to observe at a single molecule level molecular motion in nano-depth channels. We present the theoretical background of FCS, some interesting experimental findings, and our experimental work.

Theoretical background

FCS is a well-established biophysical technique developed in the early 1970s [3]. In principle, FCS can measure fluctuations in fluorescence intensity in a microscopic illuminated volume of fluorescent tagged molecules due to thermal motion. Molecular Brownian motion gives rise to fluorescence intensity bursts together with photochemical switching of the molecule, which autocorrelated in time can reveal diffusion properties and concentration of the probe. As a non invasive technique and since the introduction of confocal microscopy, which reduces the illumination volume to dimensions smaller than a femtoliter, it is widely applied to probe macromolecular interaction in cellular environment.

FLUORESCENCE

A brief overview of what are the energetic transitions that give rise to fluorescence will be given in order to understand the fluctuations recorded by FCS. When a fluorophore absorbs photons its electrons move to higher energy levels. The various energy levels involved in the absorption and emission of light by a fluorophore are classically represented in a Jablonski energy diagram.

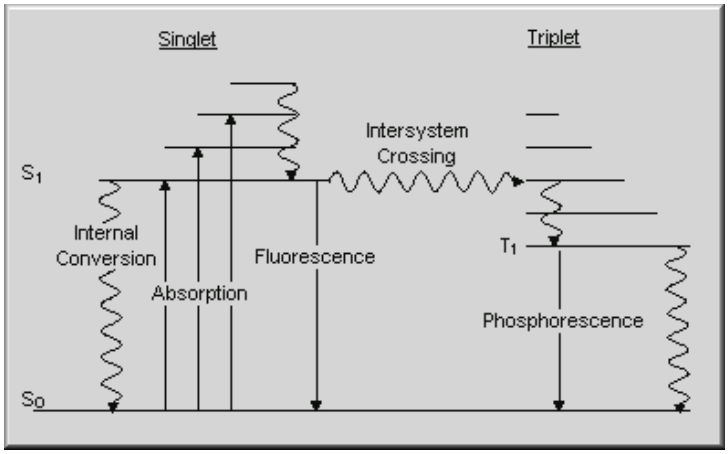

Figure 1: Schematic representation of a Jablonski energy diagram for the first energetic states, So, S1 and T1.

What first follows absorption of a photon with major probability is an internal conversion or vibrational relaxation to the lowest energy level of the first excited state S(1) = 0. This process occurs in absence of light emission on a timescale of picoseconds (ps). On a timescale much longer, of the order of nanoseconds (ns), the process named fluorescence occurs. The excited molecule finally leaves the long-lived lowest excited singlet state S(1) relaxing to the ground state S(0) with the emission of light of various wavelengths

depending on the chemical nature of the fluorochrome. The molecule can leave the exited state in alternative ways, dissipating energy as heat, or transferring energy to other molecules in a second type of non-radiative process, or going by intersystem crossing to the lowest excited triplet state. The latter phenomenon even if relatively rare, is somehow relevant because it results either in emission of light through phosphorescence or a transition back to the excited singlet state that yields delayed fluorescence. The rate constants for triplet emission are several orders of magnitude lower than those for fluorescence and thus can be easily measured by Fluorescence Correlation Spectroscopy [4].

FCS PRINCIPLES

Fluorescence in principle allows to tag and follow molecules in a detection volume. The spatial resolution of this kind of study is set by the resolving power of the microscope used which for confocal microscopy is of about 0.3 μm on the lateral dimension and 1 μm in the vertical one. Though a lot of efforts is being paid for the nanoscopy development, it is still not affordable [1,5]. Moreover the timescale of a diffusive process for a medium protein is hundreds of μs, where a typical videomicroscpy equipment can acquire images every 20 ms. Ruther than recording each molecules movement it is possible to register their fluctuations in number, which is their concentration fluctuation in the detection volume.

However in order to register relevant fluctuations of a macroscopic properties such as concentration which is at thermodynamic equilibrium by definition constant, the number of molecules in the system must be small and the relative fluctuations in the system parameters become significant. In fact in a dynamic system, relative fluctuations increase as the concentration of molecules decreases. Therefore, in order to obtain detectable fluctuations in fluorescence, the number of molecules residing in the detection volume at the same time should not be too high.

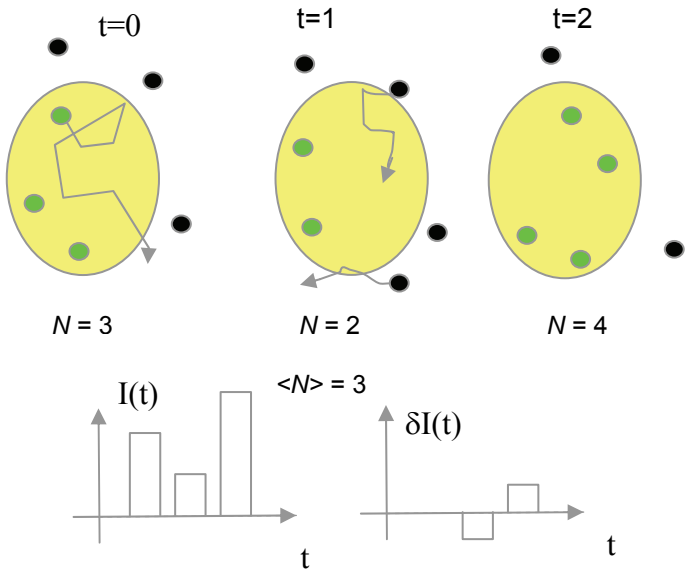

Figure 2: Cartoon of an illuminated volume where fluorescent particles move. At time t=0 three particles are detected, at t=1 there are only two, t=2 four and so on. This fluctuation in number due to Brownian motion generates a fluctuations in the fluorescence intensity detected.

In fact if we assume that molecules obey to a Poissonian distribution, the root mean square fluctuations of the particle number is given by:

$$\frac{\sqrt{\langle \delta N \rangle^2}}{\langle N \rangle} = \frac{\sqrt{\langle (N - \langle N \rangle)^2 \rangle}}{\langle N \rangle} = \frac{1}{\sqrt{\langle N \rangle}} \qquad (1)$$

which means that concentration in use for a common FCS equipment should be on the nano-micro molar range, which gives an average number of molecules in the confocal volume (~fl) in the range of 0.1-1000. FCS is therefore applied to the detection and statistical fluctuation analysis of almost single molecules (to be rigorous it applies only in the concentration range of 1 molecule on average in the detection volume), and is therefore considered a single molecule technique.

A typical FCS experiment is performed on confocal microscopes since Rigler first combined both technologies. The association of FCS technique with confocal microscopy reduces the number of molecules in the control volume, without compromising the signal to noise ratio. Basically, in a confocal what changes in comparison to a wide field microscope is the introduction of a pinhole in the beam path, on the image plane, that tremendously decreases the out of focus light and reduces the lateral dimension of the image.

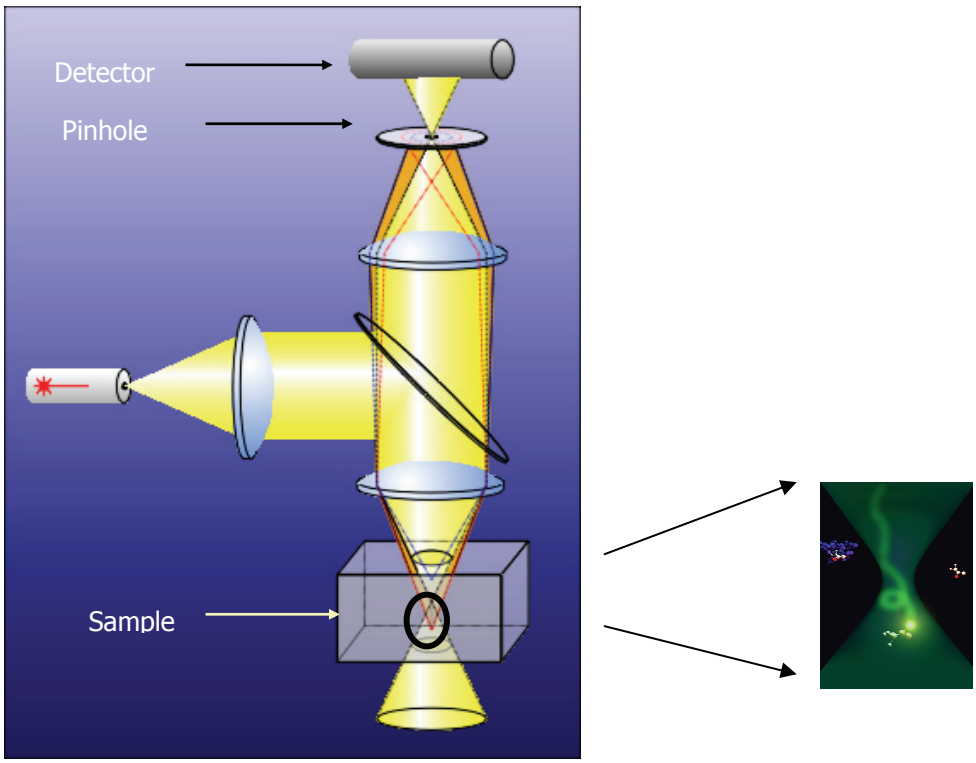

Figure 3: Picture of a confocal beam path where the introduction of a pinhole in the detection path decreases the out of focus light in the formed image.

The laser beam is directed via a dichroite mirror into a confocal microscope and focused by the objective into the sample. Emitted fluorescence from the sample comes back from the same objective, passes through the beam splitter, and is focused onto the image plane where the pinhole is located. The light passing the pinhole is spectrally filtered by highly selective bandpass emission filters and is focused onto the sensitive areas of the avalanche photodiodes. Each individual burst resulting from a single molecule can be registered. The photons are recorder in a time resolved manner. Standard TTL pulses from the diodes are fed to the PC-based correlator which autocorrelates the signal giving back the autocorrelation function[6].

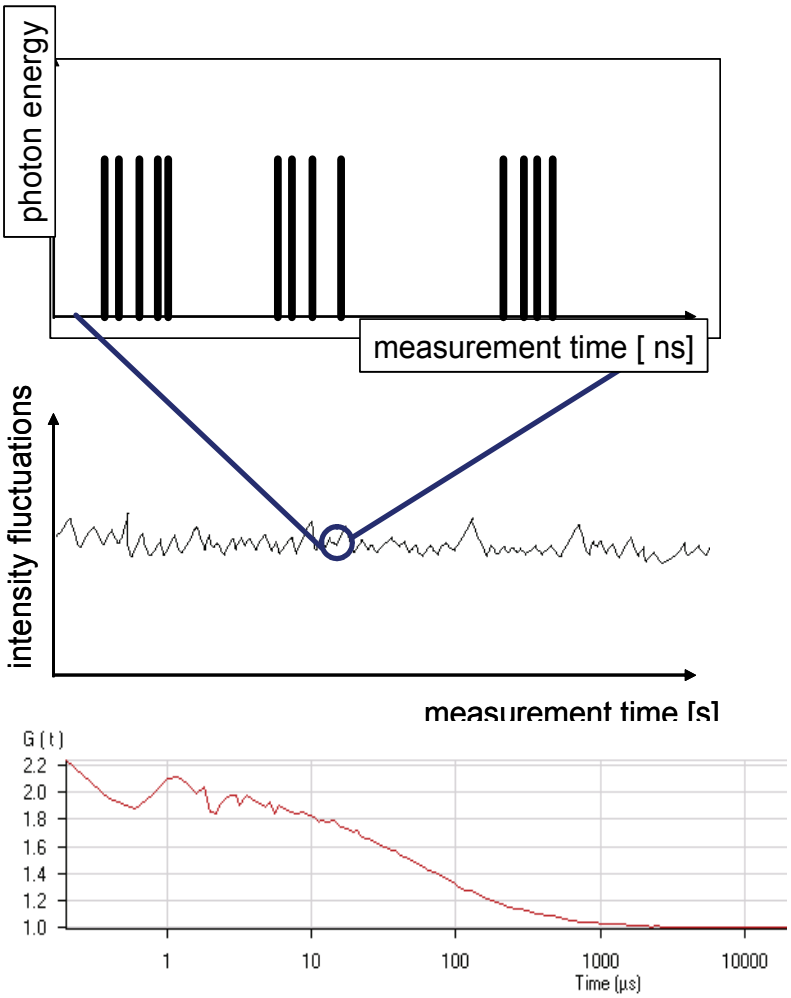

Figure 4: TTL pulses in an intensity time trace. The signal is then autocorrelated in a PC-based correlator which gives back the autocorrelation function.

CLASSICAL DERIVATION OF THE AUTOCORRELATION FUNCTION

The signal fed into the APD is recorded in a time resolved manner and represents the fluorescence intensity fluctuations due to the particles diffusion into and out of the illuminated volume. It contains information about the translational diffusion time of the molecule, which is related to the size of the confocal volume, and about the number of molecules in that volume. The way to take out these parameters starts with the autocorrelation functions analysis. The recorded fluorescence fluctuations are temporally autocorrelated which in principle means that the signal is compared over time to itself. At very close time points the signal is similar to itself, whereas as the time goes by it gets more and more different, as it is shown in the cartoon in fig 5.

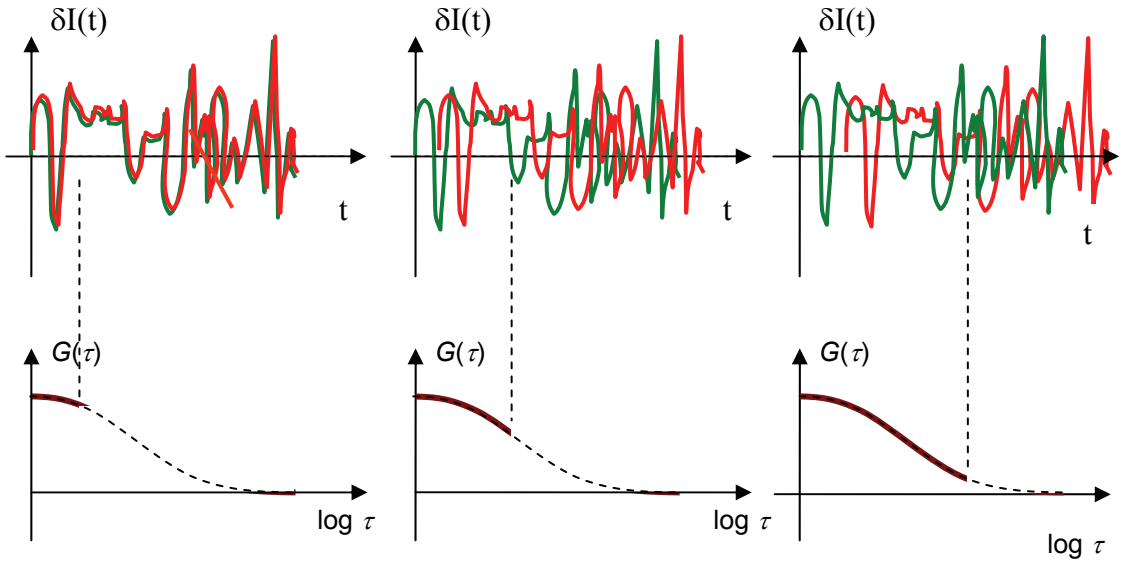

Figure 5: Schematic representation of the formation of an autocorrelation function. The self similarity of the deviation of the intensity signal is lost by time, which means that the system is loosing autocorrelation.

The autocorrelation function is defined as:

$$G_{\mathrm{O}}(\tau) = \frac{\langle \delta I(t)\, \delta I(t+\tau) \rangle}{\langle I(t) \rangle^2} \qquad (2)$$

where $\delta I(t)$ are the instantaneous deviations from the time average of the fluorescence intensity calculated as in eq 3:

$$\delta I(t) = I(t) - \langle I(t) \rangle . \qquad (3)$$

In the simplest case, all fluctuations arise from passages of the molecules in the detection volume, or in other terms, from local fluctuations of molecules' concentration. Basically they depend on the probability for a particle in r at time t=0 to be after a time τ in the position r', weighted over the detection efficiency of the instrument. This is because when a particle translates in the middle of the laser beam exited area the detection efficiency in that point is higher compared to a transition on the borders, where the laser beam energy is actually lower.

Under the assumption that all fluorocrhome properties are not changing over time the autocorrelation function can be computed as:

$$G(\tau)=\frac{<\delta I(0)\delta I(\tau)>}{<I(t)>^2}=\frac{\iint_V I_e(r)I_e(r')\phi(r,r',\tau)drdr'}{\left(\langle C\rangle\int_V I_e(r)dr\right)^2}=\frac{\iint_V I_e(r)I_e(r')\langle\delta C(r,0)\delta C(r',\tau)\rangle drdr'}{\left(\langle C\rangle\int_V I_e(r)dr\right)^2} \quad (4)$$

Where we have associated fluctuations in fluorescence intensity to fluctuations in molecule concentration, having discarded fluctuations in physical-chemical parameters of the fluorochrome itself (molecular absorption cross-section, quantum yield).

Thus the autocorrelation function of intensity fluctuations is a convolution of the autocorrelation function of the concentration fluctuations with the emission profile. $I_e(r)$ is in fact the spatial emission intensity distribution, which is typically assumed to have a Gaussian shape profile computed as:

$$I_e(r)=e^{-2\frac{x^2+y^2}{w_{xy}^2}}e^{-2\frac{z^2}{w_z^2}} \quad (5)$$

where w_{xy} and w_z define the beam waist half amplitudes across the xy plane and the orthogonal direction z. The emission intensity distribution function is determined by the optical transfer function of the objective-pinhole combination which determines the spatial collection efficiency of the setup, times the spatial amplitude of the excitation energy.

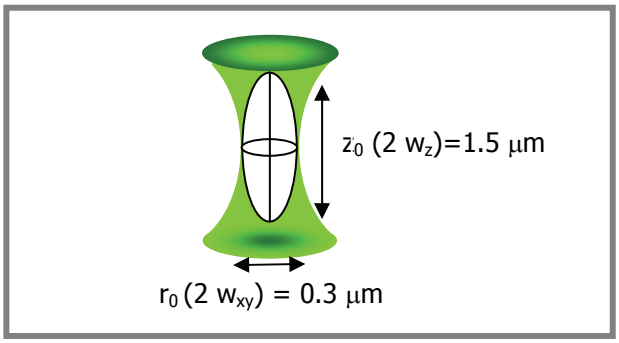

Figure 6: Representation of a Gaussian emission beam shape.

The fluctuations in concentration can be computed, as they are basically the average concentration times the probability density p_{xyz} for a single molecule which starts a random walk at time t=0 at point r to be at r' after a time t.

$$\langle\delta C(r,0)\delta C(r',\tau)\rangle=\langle C\rangle\frac{1}{(4\pi D\tau)^{-\frac{3}{2}}}e^{-\frac{(r-r')^2}{4D\tau}} \quad (6)$$

which is basically the Fick's second law solution for diffusion with the appropriate boundary conditions, as shown in chapter 2, with diffusion coefficient D. If the effective confocal volume is defined as:

$$V_{eff} = \frac{\left(\int I_e(r)dV\right)^2}{\int I_e(r)^2 dV} = \frac{\left(\int e^{-2\frac{x^2+y^2}{w_{xy}^2}} e^{-2\frac{z^2}{w_z^2}} dV\right)^2}{\int e^{-4\frac{x^2+y^2}{w_{xy}^2}} e^{-4\frac{z^2}{w_z^2}} dV} = \pi^{\frac{3}{2}} r_0^2 z_0 \qquad (7)$$

Then we can substitute in eq. 4 eq.5, 6 and 7 and we can obtain the expression for the autocorrelation function in a 3D Brownian diffusion process:

$$G(\tau) = \frac{1}{N} \frac{1}{\left(1+\frac{4D\tau}{\omega_{xy}^2}\right)\sqrt{\left(1+\frac{4D\tau}{\omega_z^2}\right)}} \qquad (8)$$

The confocal volume shape is assumed to be Gaussian on x,y,z directions, and can be identified from the structure parameter s given from the ratio: $s= w_z / w_{xy}$ of the two parameters that identify the Gaussian beam size. The diffusion time τ_{diff} is related to the lateral beam waist of the focus through:

$$\tau_{diff} = w_{xy}^2 / 4D \,. \qquad (9)$$

Then it is possible to rewrite the autocorrelation function in eq. 7as a function of N, s, τ_{diff} , which are basically the readout parameters from an FCS experiments:

$$G(\tau) = \frac{1}{N} \frac{1}{\left(1+\frac{\tau}{\tau_{diff}}\right)\sqrt{\left(1+\frac{\tau}{\tau_{diff} s^2}\right)}} \qquad (10)$$

The autocorrelation function $G(\tau)$ that we have obtained in eq 10 is the product of three independent functions each one referred to one dimensionality (or direction) :

$$G_{xyz}(\tau) = g_x(\tau)g_y(\tau)g_z(\tau) \tag{11}$$

This is possible as long as motion is isotropic. Moreover it is physically meaningful as it corresponds to independent molecules translations along each direction. From eq. 11 then we can split each single contribute of a 3D autocorrelation function and derive the autocorrelation function in the case of bi-dimensional motion or mono-dimensional motion, simply by elimination the g(τ) contribute along the direction we are not sensitive to.

Each contribute can be written as:

$$g_i(\tau) = \frac{1}{k}\frac{1}{\sqrt{\left(1+\frac{\tau}{\tau_{diff}}\right)}} \tag{12}$$

Where k is a constant related to the effective volume definition, which for a non 3D shape has no longer the expression reported in eq. 6. Then we can compute the expressions of the autocorrelation function for 1D and 2D diffusion processes:

$$G_{2D}(\tau) = \frac{1}{N}\frac{1}{\left(1+\frac{\tau}{\tau_{diff}}\right)}; \tag{13}$$

$$G_{1D}(\tau) = \frac{1}{N}\frac{1}{\sqrt{\left(1+\frac{\tau}{\tau_{diff}s^2}\right)}} \tag{14}$$

Which are the autocorrelation functions in 2D and 1D geometries[7-10].

TRIPLET STATE KINETIC

The classical model has been developed under the assumption that all dye photochemical features will not change over the experimental time. Actually, this assumption might be inadequate. Many transitions can happen during a measurement run but on the observation time scale (smaller than μs) what the instrument is very sensitive to are the transitions due to the triplet state. A triplet state correction is then needed to account for the first μseconds of the autocorrelation function shape. It was demonstrated that the autocorrelation function correction for a triplet state kinetic can be written as:

$$G(\tau)_t^{cor} = \left((1-T) + Te^{-\frac{\tau}{\tau_t}} \right) G_{dif}(\tau) \quad (15)$$

where T is the fraction of non fluorescent molecules due to a triplet state, and τ_t is the time spent in a triplet state [11].

ANOMALOUS DIFFUSION MODEL

As we have already discussed in chapter 2, in the case of presence of steady obstacles that hinder molecular motion it was found that the mean square displacement does not follow any longer a linear dependence with time but rather it is proportional to some power of time less than 1:

$$\langle r(t)^2 \rangle = 6D(t)t \propto t^{\alpha} \quad (16)$$

where α is the anomalous coefficient, with α <1. This means that in the treatment we have proposed to compute the autocorrelation function, the Brownian propagator represented in equation 5 does not hold anymore.

Taking into account this diverse time dependence of diffusion, which is translated into a different time correlation of concentration fluctuations we can compute an autocorrelation function for anomalous diffusion kinetic:

$$G(\tau) = \frac{1}{\langle N \rangle} \left(1 + \frac{Te^{-\tau/\tau T}}{1-T} \right) \cdot \frac{1}{1 + \left(\tau / \tau diff \right)^{\alpha}} \cdot \frac{1}{\sqrt{1 + \frac{\left(\tau / \tau diff \right)^{\alpha}}{s^2}}} \quad (17)$$

Where α represents the anomalous coefficient and where also the triplet state correction appears[12-13].

Model of diffusion limited by boundaries in the axial direction: our treatment

Nanochannels are characterized by a micrometric width and a nanomentric height, with a rectangular cross section. As we have mentioned before in one photon fluorescence correlation spectroscopy the detection volume has a Gaussian shape profile, with waist radius in the order of 300 nm and a waist height of about five to seven times the radius, i.e. above 1.5 μm.

Whenever the sample we are probing is as small as the size of the confocal volume, and our nanochannels belong to this scenario, we should consider the case where boundaries in the xy plane rather than in the z direction affect the shape of the autocorrelation function. As it was shown by Gennerich in 2000 [14] for cytosolic compartments investigated by FCS, it is fundamental to take into account boundaries in the diffusion path to generate a diverse autocorrelation function. The misinterpretation of a confined geometry could lead to experimental fitting results with pour biophysical meaning.

Though Gennerich work is a breakthrough in this field and unique, it can not derive a closed form for the autocorrelation function in the case of lateral or vertical boundaries. We demonstrated a diverse mathematical treatment which gives rise to a closed form for the final autocorrelation function.

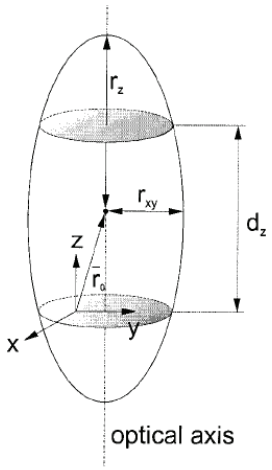

Figure 7: Quasi-ellipsoid detection volume V_d, characterized by the radii xy and z, confined in axial direction by boundary planes at z=$z0 \pm d_z/2$. With respect to the origin (x = 0, y= 0, z =0), the detection volume of the confocal setup is centered at $\boldsymbol{r}0 = (x_0, y_0, z_0)$.

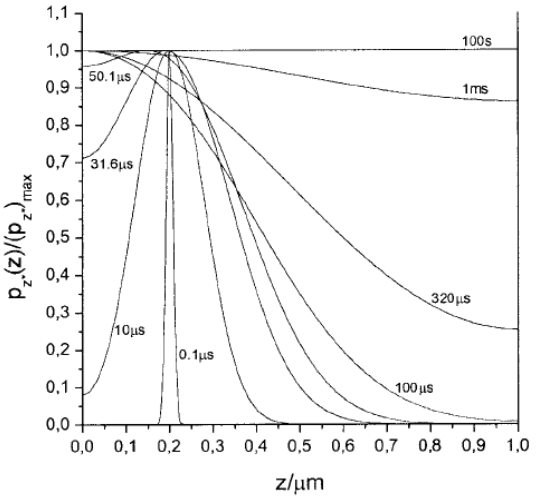

Figure 8: Normalized probability density $p_z(z)$ for a single molecule whose diffusion is confined to the space between boundary planes at z = 0 μm and z = 1 μm (d_z = 1 μm), plotted for different times τ after the start of the random walk at z' = 0.2 μm (D = 2.8 x 10^{-6} cm^2/s)

In the case of confinement along optical axis, there is only a fraction of the excitation volume which indeed gives rise to fluorescence fluctuations. As the diffusive flux vanishes at the boundaries, Gennerich expanded the concentration fluctuation d*C*(***r***, *t*) in a Fourier cosine series along the *z*-axis. After a number of algebraic steps and Fourier transforms, they showed that as it is:

$$G_{xyz}(\tau) = g_x(\tau) g_y(\tau) g_z(\tau) \tag{18}$$

we can write:

$$G_{xyZ}(\tau) = \frac{1}{N} \frac{1}{\left(1 + \frac{\tau}{\tau_{diff}}\right)} . G_{Zc}(\tau); \tag{19}$$

and the term related to the confined fluctuation con be obtained from:

$$p_k(t) = \frac{1}{d_k} \sum_{n=-\infty}^{\infty} Exp(-Dt(\frac{n\pi}{d_k})^2) Cos(\frac{n\pi}{d_k} k) Cos(\frac{n\pi}{d_k} k') \tag{20}$$

which gives the one-dimensional probability density of a molecule whose random walk is confined to the space between the boundary planes.

OUR TREATMENT:

In our treatment we did not confine the concentration fluctuations but we mirrored the emission volume against the lateral boundaries. Thus we treated an unconfined molecule which translates in an apparent periodic detectable emission obtained as consecutive mirroring of the real one at the system boundaries.

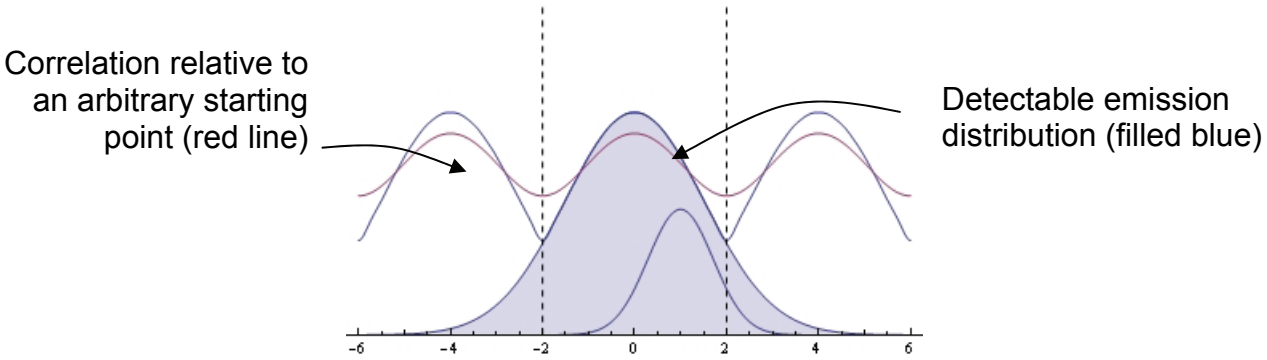

Figure 9: Concept idea representation of the mathematical procedure. In filled blue Gaussian emission distribution, which is reflected at the boundaries -2, +2 in arbitrary unit. in the drawing. in red correlation relative to an arbitrary starting point.

By averaging respect all possible starting positions inside the real system, it could finally be computed the correlation contribute corresponding to the confined direction:

$$g_k(t/t_d) = \frac{\sqrt{\pi}\,Erf(\sqrt{2}R)}{2RErf(2R)}\left(1 - \sum_{n=1}^{\infty} Exp(-(1+t/t_d)(\frac{n\pi}{2R})^2)\,\mathrm{Re}(Erf(\sqrt{2}R + i\frac{n\pi}{2\sqrt{2}R}))\right) \qquad (21)$$

Where: $t_d = \frac{r_k^2}{4D} =$ is the characteristic time of the fluctuation evolution, and where $R = \frac{d_k}{r_k} =$ is the ratio of real system size and amplitude of laser beam.

The model well represents the expected physical behavior for decreasing system size.

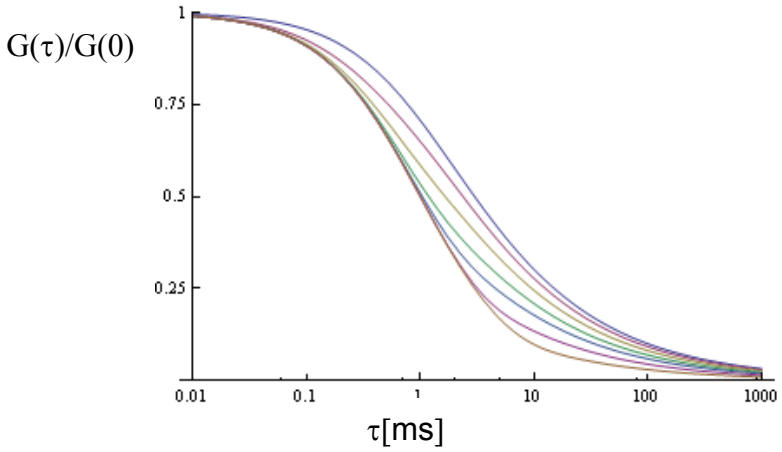

Figure 10: Modeled auto-correlation relative to a 3D case with one constrained direction for a number of values R=d/r

In fact, for decreasing system size the autocorrelation function moves towards the 2D autocorrelation function. This is shown in figure 10 where we represent a 3D autocorrelation function with one confined dimensionality. This means that as the detection volume is narrowed because of physical boundaries along one direction, we lose sensitivity from the confined dimension up to confusing the system with a 2D geometry.

Therefore our treatment is advantage because it permits to write a closed form for the autocorrelation function in a confined geometry preserving the problem physical meaning.

Measurements of transport properties in nanochannels

Molecular dynamics in glass nanoslits are investigated by fluorescence correlation spectroscopy. FCS can probe transport properties in micro - nanofluidic structures at a single molecule level. Both molecular weight, molecule chemistry and deformability can affect particle mobility. Hence molecules of interest rationalize diverse possible mechanisms taking into account molecules of low and high molecular weight and diverse rigidities. Evidence of constrained diffusion are shown.

MATERIALS

Borosilicate nanochannels manufactured by chemical etching and direct bonding procedures as described in chapter 5 are used to affect molecules mobility as recorded by FCS. Channels are nanomentric in depth and micrometric in width. Depth can vary between 10 , 20 and 30 nm; whereas width of imaged channels is 5, 10 or 30 microns with a constant length of 500 microns. Molecules features deeply influences transport mechanisms, therefore we investigated Rhodamine 6G (Fulka) as a small rigid molecule; Dextrans of two molecular weights, Dextrans 40kDa-Rhod6G (Molecular Probes Invitrogen), Dextrans 70kDa-RhodB, (Molecular Probes Invitrogen), to take into account molecule size effect in the case of a flexible molecule; and PEG 20kDa-RhodB (Nanocs, New York) to consider how a more flexible molecule, compared to dextrans, having a diverse chemistry can regulate the undergoing transport mechanism. DI water (ph=5.4) filtered with 100 μm filters (Whatman) was used to prepare fresh 100 nM molecules solutions.

Molecule	MW [Da]	r_h [nm]
Rhod6G	479	0.8*
dextran	40000	6*
dextran	70000	9*
PEG	20000	5.8*

Table 1: Molecule dimension and molecular weight. r_h determined from Stokes-Einstein relation.

Microscopes:

Two different confocal systems were used for measurements, a Leica FCS2 extension of TCS SP2 AOBS confocal microscope in EMBL, Heidelberg, and a ConfoCorII Zeiss available in our lab at DIMP, Università Federico II, Napoli.

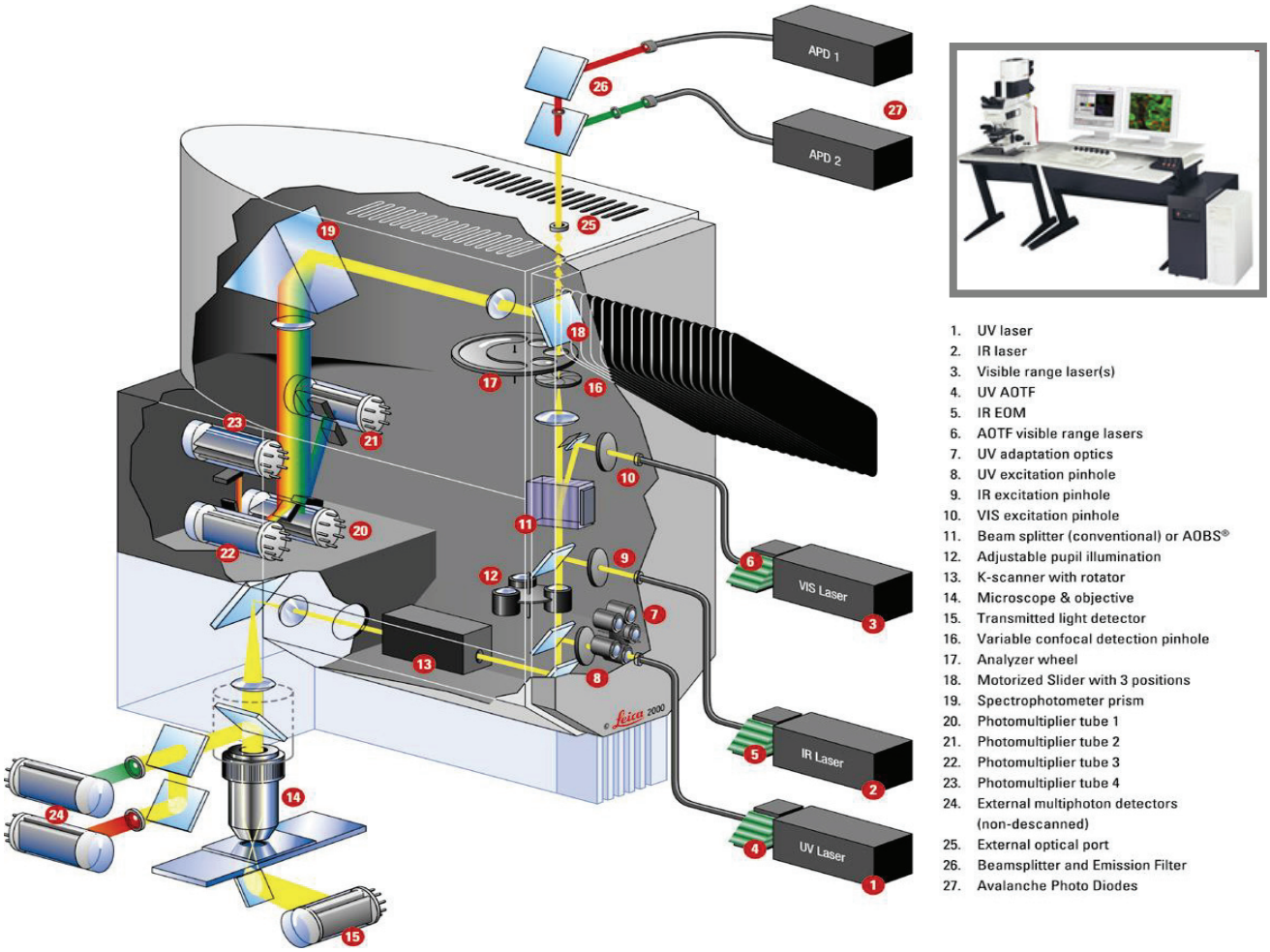

Figure 11: LEICA SP2 AOBS, FCS system

The main SP2 Leica microscope features for our applications are the Acousto-Optical Beam Splitter (AOBS) and the galvanometer driven fine focusing stage for z positioning.

The AOBS, represented in figure 11 with the number 11, directs the excitation light of the laser onto the specimen and separates the fluorescent light returned from the specimen and the reflected excitation light. It replaces conventional excitation filters such as double or triple dichroite. The AOBS is a transparent optical crystal to which an ultrasonic field is applied. Light which penetrates the optical crystal. Is deflected depending in its wavelength and the wavelength of the ultrasonic field. The AOBS can therefore select a laser line, control the amount of light and the beam splitter ratio between excitation and detection light for the selected laser line. Moreover the two tools enhanced and ultra-high dynamics ensure that reflection light, which comes back through the beam

path in opposite direction, is removed from the optical axis and therefore is not detected. This tool was useful as our sample are not so bright and can generate a high percentage of reflected light which can reduce the signal to noise ratio. Through the same tool it is also possible to select a high rate of reflected light which is a useful tool as well whenever focusing on the sample is necessary. Also the galvanometer driven fine focusing stage for z positioning can be helpful for focusing as it is useful for creating images from vertical xz sections and through the z selection tool, it is possible to go back to a xy scan at the z plane selected.

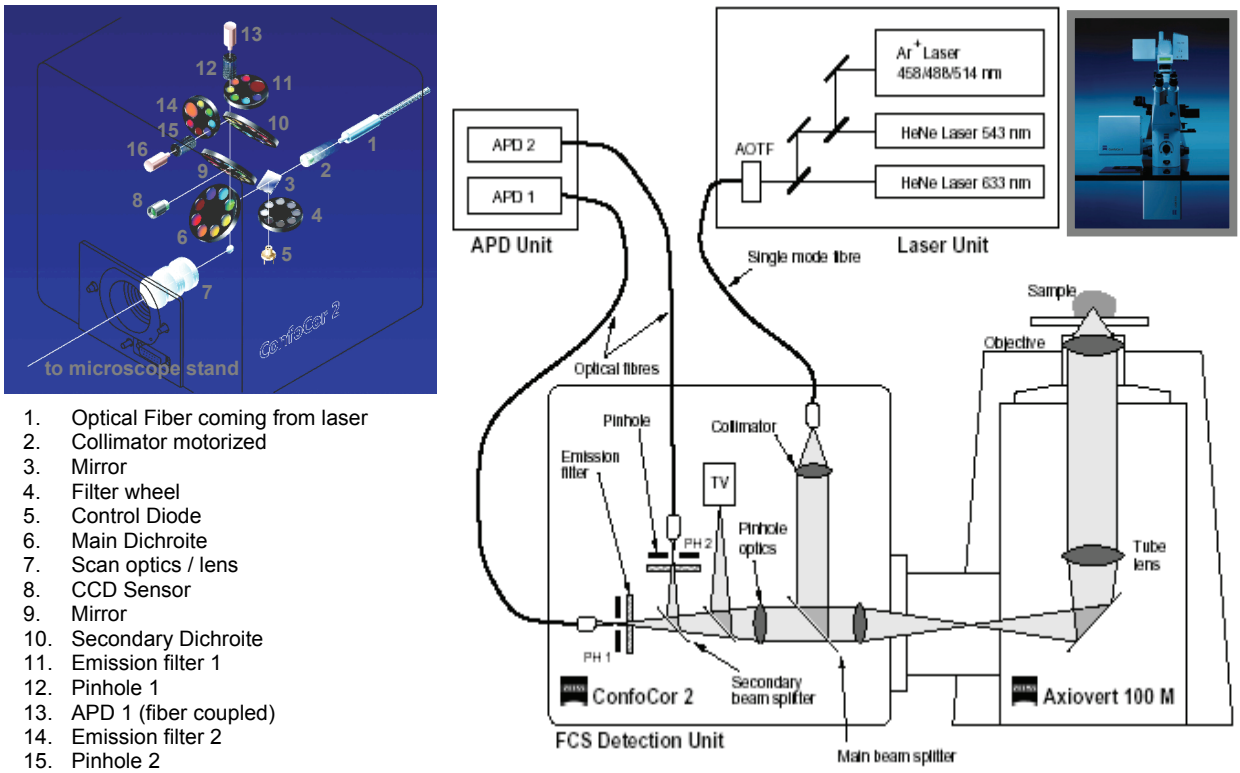

1. Optical Fiber coming from laser
2. Collimator motorized
3. Mirror
4. Filter wheel
5. Control Diode
6. Main Dichroite
7. Scan optics / lens
8. CCD Sensor
9. Mirror
10. Secondary Dichroite
11. Emission filter 1
12. Pinhole 1
13. APD 1 (fiber coupled)
14. Emission filter 2
15. Pinhole 2
16. APD 2

Figure 12: ZEISS ConfCor II, optical path and, on the left, optical elements in the FCS head.

The ConfCor II has a conventional dichroite beam splitter and it does not allow xz scansion mode, therefore focusing was accomplished manually during xy imaging. On the other hand it was easier to change filter sets for FCS measurements in ConfoCor II compared to SP2, because though SP2 is a filterless confocal (spectral scanner), the FCS module need the manual replacement of filter cubes.

Both systems are equipped with built-in correlators though we took advantage of a custom developed software, (Fluctuation Analyzer by Malte Wachsumth) for all of our measurements in nanochannels.

METHODS

Nanochannels were placed in the chipholder and all the fluidic connections were properly set. The chip was then connected by PEEK connectors to a syringe filled first with DI filtered water. A small pressure was applied and the solution was sucked into the channels. Then syringe was filled with a nanomolar fluorescent molecule solution and a small pressure was applied to load the channels. Nanochannels were let equilibrate for several hours before measurements to permit the fluorescent solution to diffuse from the micrometric reservoirs to the nanochannels and to equilibrate. Experiments were run the day after channel loading. Two different confocal systems were used for measurements, a SP2 Leica microscope in EMBL Heidelberg, and a ConfoCorII Zeiss available in DIMP, Napoli. The nanochannels were first imaged in the red channel on a LEICA SP2 system with 63X Plan Apo 'CS lbd. blu water correction 1.2 N.A. lens objective taking advantage of a xz scan tool to better identify the focus plane, whereas on the ConfoCorII channels were scanned in xy plane with a 40X Apochromat 1.2 N.A. water objective and then focus was manually adjusted. FCS experiments were performed in the middle of channels. Rhodamine6G tagged molecules were excited with the 488 nm line of the Argon laser, fluorescent emission was sent to a 530 nm LP filter and then acquired on the APD. RhodamineB tagged molecules were excited with the 543 nm HeNe laser, fluorescent emission was sent to a 560 nm LP filter and then acquired on the APD. Measurement time could vary between 60 and 120 seconds. Each experiment was carried out at least 10 times to have statistical information. For each molecule experiments were repeated in every channel height available, i.e. 10 nm, 20 nm and 30 nm.

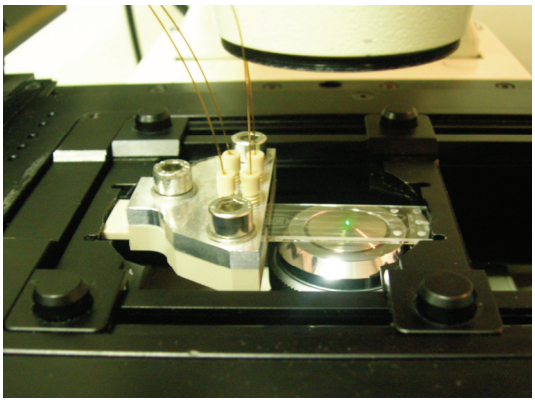

Figure 13: Nanochannels placed on top of 40X objective of ConfCorII microscope.

Laser beam was accurately directed in the middle of the channel. Data obtained from FCS measurements of bulk solutions were analyzed using ISS software rather than ConfCorII software, whereas experiments in nanochannels were analyzed by means of an autocorrelation software which was custom developed (Fluctuation Analyzer), and fitted with the non-linear fitting routine on Origin Microcal 7.0 based on the Levenberg-Marquardt algorithm. As 30 nm height reduce the sensitivity of our experimental system to a 4% over the vertical axis, it is like we do not perceive any motion in the z direction. Therefore we used a 2D model to fit our data. Both pure anomalous diffusion model and anomalous diffusion model upgraded for confinement were used.

RESULTS AND DISCUSSION

Channels were successfully imaged on both confocal systems. This shows that channels are empty, open and freely accessible to fluorescent solutions. In figure 14 we show two confocal images acquired on the SP2 system. On the left a xz section of a 30 mm wide channel loaded with a solution 100 nM of Rhodamine 6G is represented while on the right side the corresponding xy image is presented (magnification is different as suggested from scale bar).

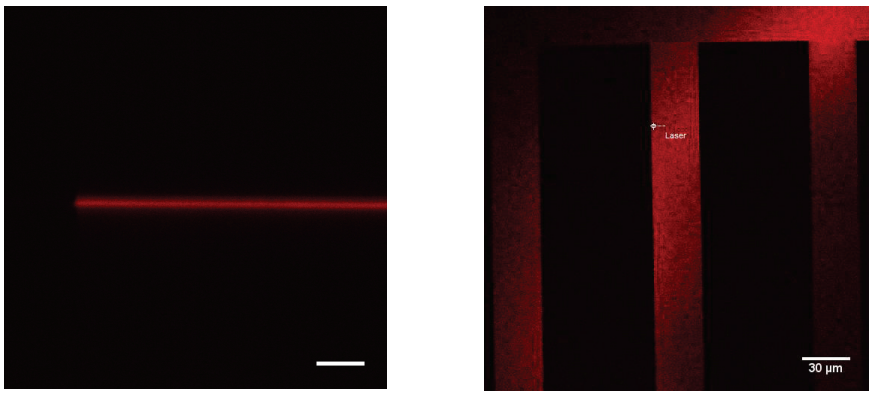

Figure 14: Confocal micrographs of 30 μm wide, 30 nm depth nanoslits loaded with Rh6G solution_ Left : xz cross section, scale bar 3 μm. Right: xy view, scale bar 30 μm.

FCS experiments were carried out for four different molecules each in three diverse channels size, 10, 20 and 30 nm. The results for Rhodamine 6G, Dextran 40kDa, Dextran 70kDa, and PEG 20kDa are reported below.

Rhodamine6G

Freshly prepared nanomolar solution of Rhodamine 6G were loaded into the channels and FCS measurements were run. Autocorrelation functions from bulk measurements and from measurements in 30 nm height, 20 nm height and 10 nm height channels are represented in figure 15.

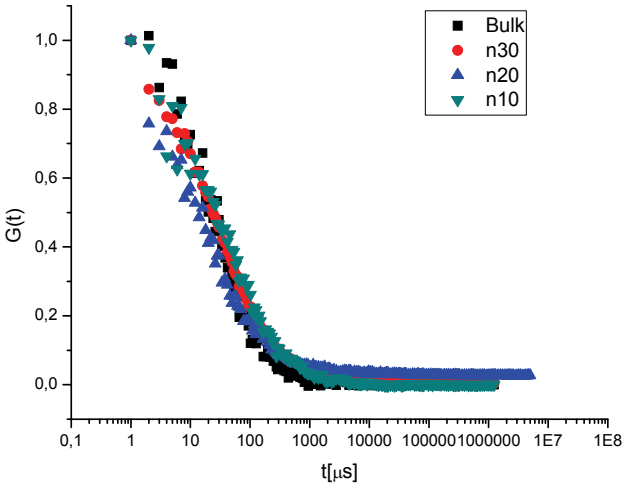

Figure:15. Autocorrelation Functions of Rhodamine6g for bulk measurements, black squre, and 30, red circle, 20, up-triangle blue, 10 nm channels, green triangle.

Below are reported in figure 16 the single component anomalous diffusion model fitting results for the Rhodamine 6G molecule. Both diffusion time and the anomalous parameter α are reported as a function of the ratio molecule hydrodynamic diameter against channel height.

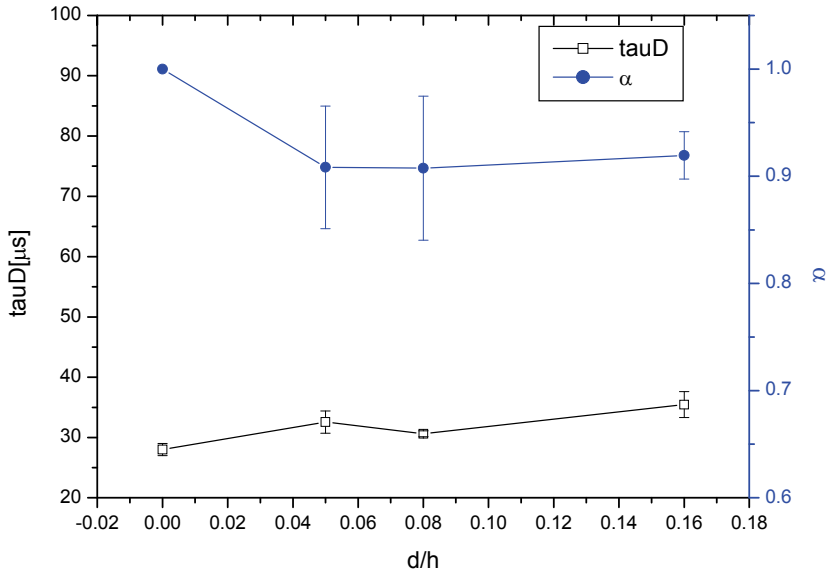

Figure 16:. Single component anomalous diffusion model fitting results for Rhodamine 6G molecule. On the left vertical axis is reported diffusion time and on the right axis the anomalous parameter α versus the ratio between molecules diameter and channel height.

Dextran40kDa

Freshly prepared nanomolar solution of Dextran 40kDa were loaded into the channels and FCS measurements were run. Autocorrelation functions from bulk measurements and from measurements in 30 nm height, 20 nm height and 10 nm height channels are represented in figure 17.

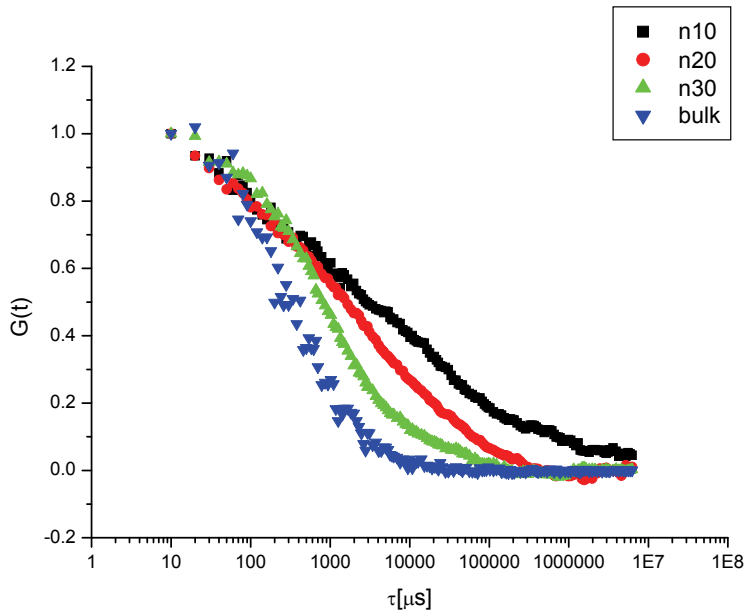

Figure:17. Autocorrelation functions of Dextran40kDa for bulk measurements, down triangle blue, 30 nm, up-triangle green, 20nm red circle, 10 nm channels, black square.

Below are reported the fitting results for a two components anomalous diffusion fitting model of Dextran40kDa autocorrelation functions. Both diffusion time and the anomalous parameter α are reported as a function of the ratio molecular hydrodynamic diameter against channel height.

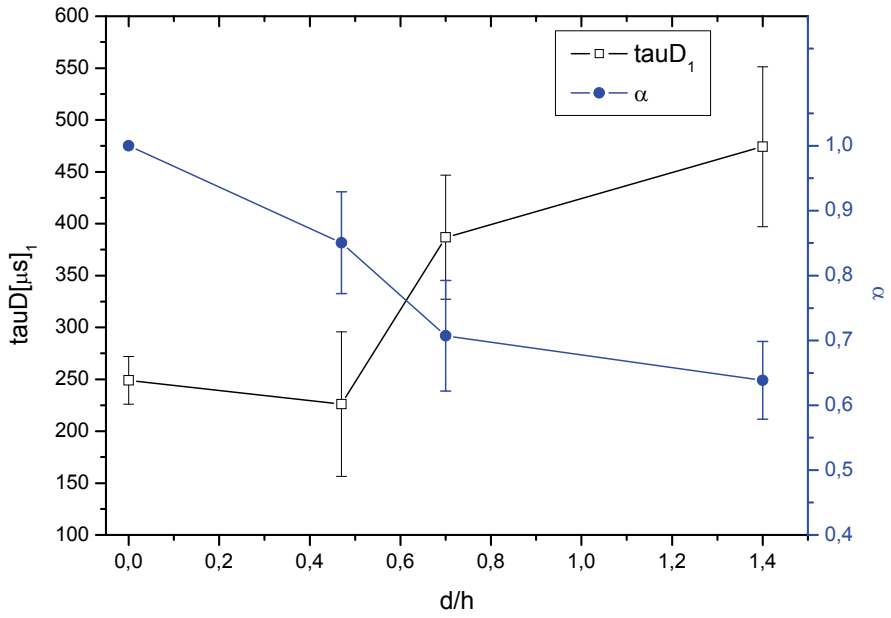

Figure 18. Two components anomalous diffusion model fitting results for the Dextran40kDa molecule. On vertical axis we report the diffusion time against the ratio between molecules diameter and channel height; and on the other axis we report the anomalous parameter α for first fitting component.

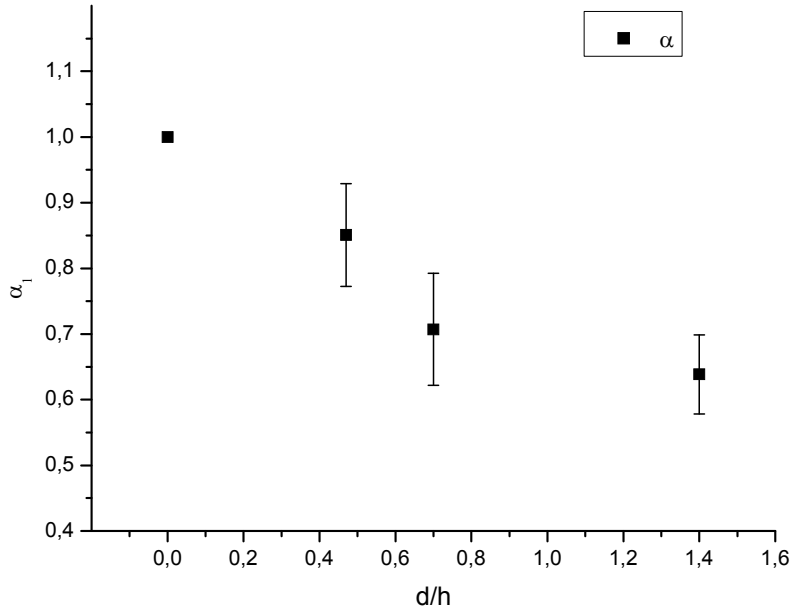

Figure 19:. Two components anomalous diffusion model fitting results for the Dextran40kDa molecule. On vertical axis is reported the anomalous parameter α against the ratio between molecules diameter and channel height evaluated for the first fitting component.

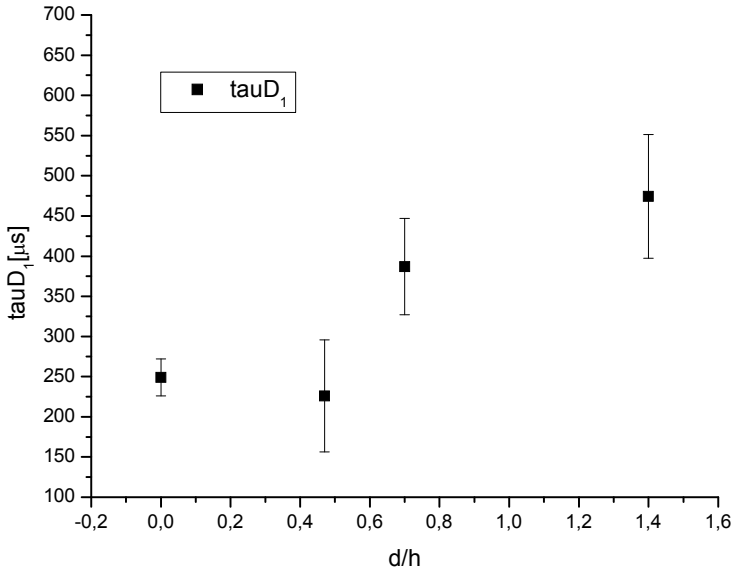

Figure 20:. Two components anomalous diffusion model fitting results for the Dextran40kDa molecule. On vertical axis is reported the diffusion time for the first component against the ratio between molecules diameter and channel height.

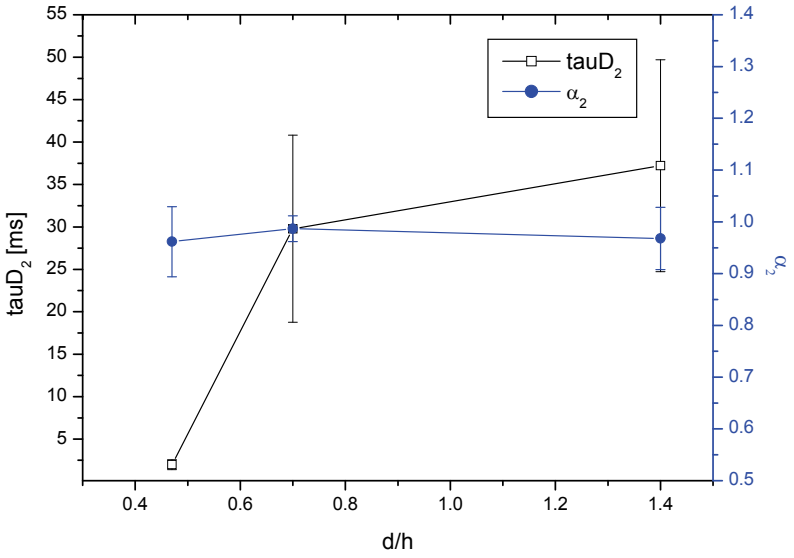

Figure:21. Two components anomalous diffusion model fitting results for the Dextran40kDa molecule. On vertical axis we report the diffusion time of second component against the ratio between molecules diameter and channel height; and on the other axis we report the anomalous parameter α.for second component.

Dextran70kDa

Freshly prepared nanomolar solution of Dextran 70kDa were loaded into the channels and FCS measurements were run. Autocorrelation functions from bulk measurements and from measurements in 30 nm height, 20 nm height and 10 nm height channels are represented in figure 22.

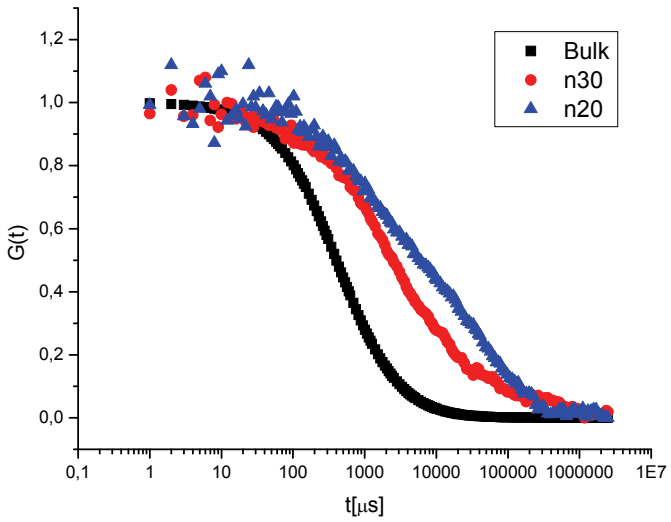

Figure:22. Autocorrelation functions of Dextran70kDa for bulk measurements, black square, 30 nm, red circle 20nm up-triangle blue.

Below are reported the fitting results for a two components anomalous diffusion fitting model of Dextran70kDa autocorrelation functions. Both diffusion time and the anomalous parameter α are reported as a function of the ratio molecular hydrodynamic diameter against channel height.

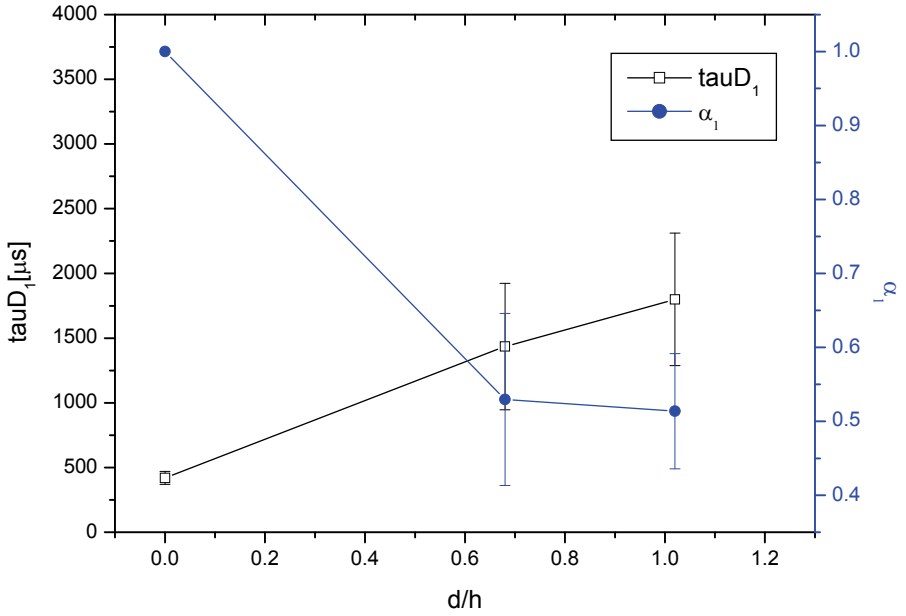

Figure:23. Two components anomalous diffusion model fitting results for the Dextran70kDa molecule. On vertical axis we report the diffusion time against the ratio between molecule diameter and channel height; and on the other axis we report the anomalous parameter α. Both parameters are results for the first fitting component.

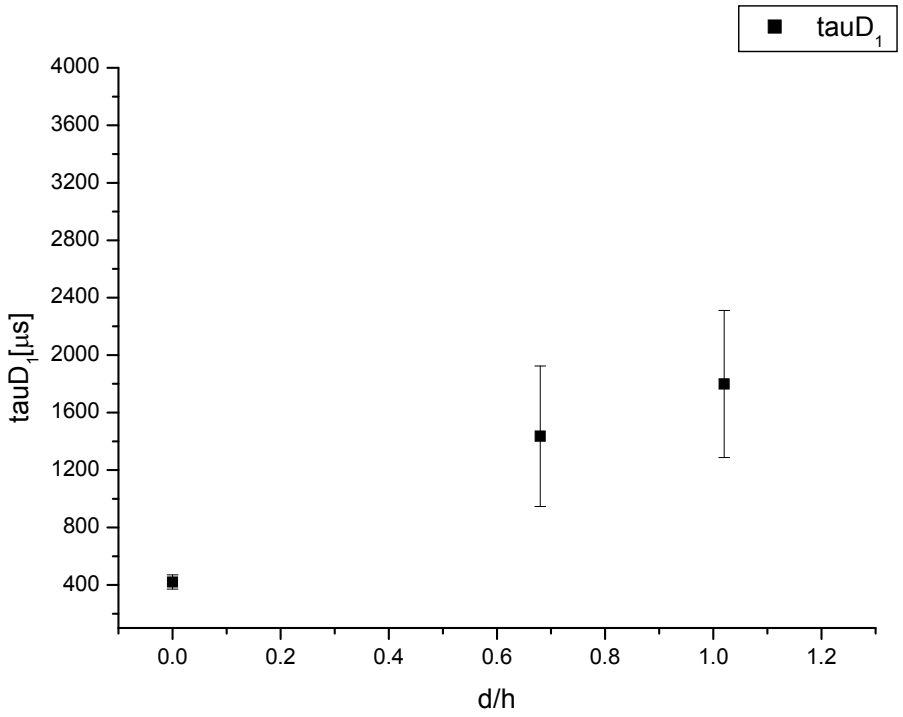

Figure 24: Two components anomalous diffusion model fitting results for the Dextran70kDa molecule. On vertical axis is reported the diffusion time against the ratio between molecule diameter and channel height evaluated for the first fitting component.

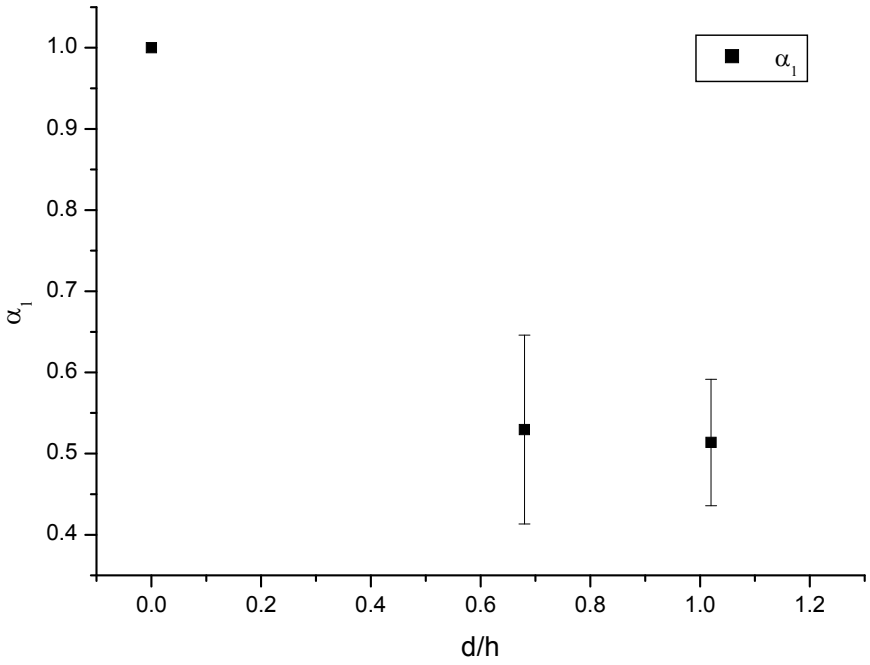

Figure:25. Two components anomalous diffusion model fitting results for the Dextran70kDa molecule. On vertical axis is reported the anomalous parameter α against the ratio between molecules diameter and channel height evaluated for the first fitting component.

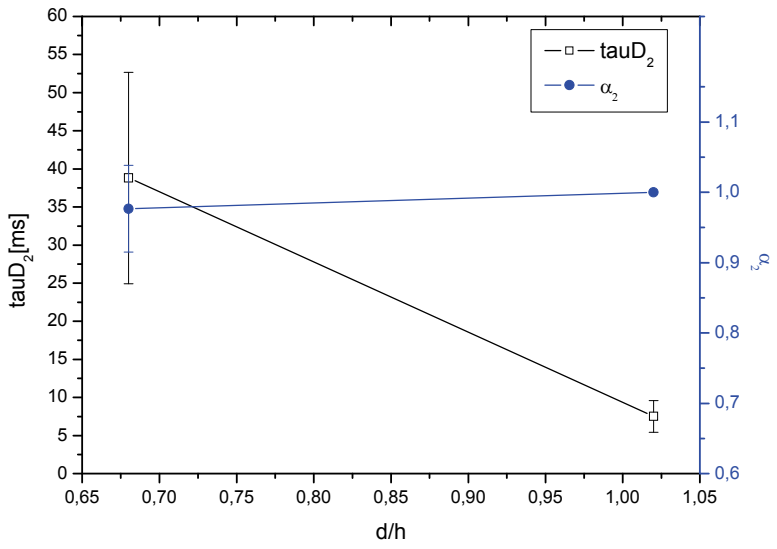

Figure:26. Two components anomalous diffusion model fitting results for the Dextran70kDa molecule. On vertical axis we report the diffusion time against the ratio between molecules diameter and channel height; and on the other axis we report the anomalous parameter α. Both parameters are results for the second fitting component.

PEG20kDa

Freshly prepared nanomolar solution of PEG20kDa were loaded into the channels and FCS measurements were run. Autocorrelation functions from bulk measurements and from measurements in 30 nm height, 20 nm height and 10 nm height channels are represented in figure 27.

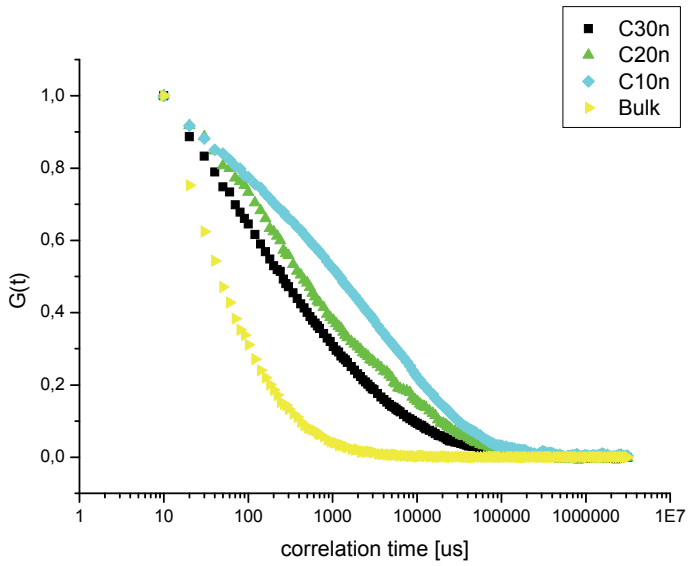

Figure:27. Autocorrelation functions of Peg20kDa for bulk measurements, yellow, 30 nm, black square, 20nm up-triangle green, 10 nm light blue.

Below are reported the fitting results for a two components anomalous diffusion fitting model of Peg 20kDa autocorrelation functions. Both diffusion time and the anomalous parameter α are reported as a function of the ratio molecular hydrodynamic diameter against channel height.

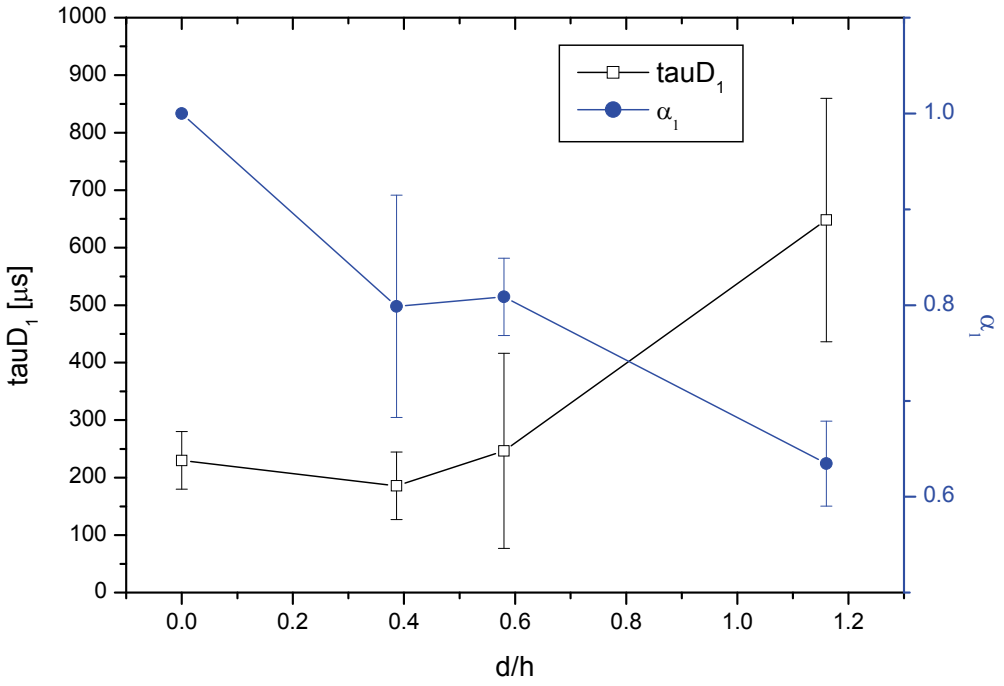

Figure 28: Two components anomalous diffusion model fitting results for Peg20kDa molecule. On vertical axis we report the diffusion time against the ratio between molecules diameter and channel height; and on the other axis we report the anomalous parameter α. Both parameters are results for the first fitting component.

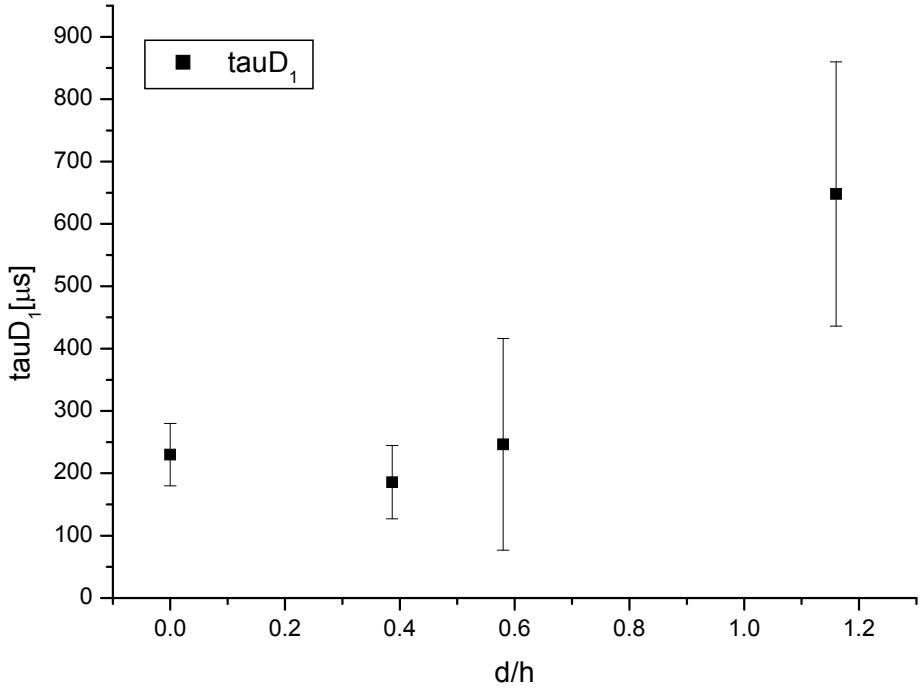

Figure 29: Two components anomalous diffusion model fitting results for the Peg20kDa molecule. On vertical axis is reported the diffusion time against the ratio between molecules diameter and channel height evaluated for the first fitting component.

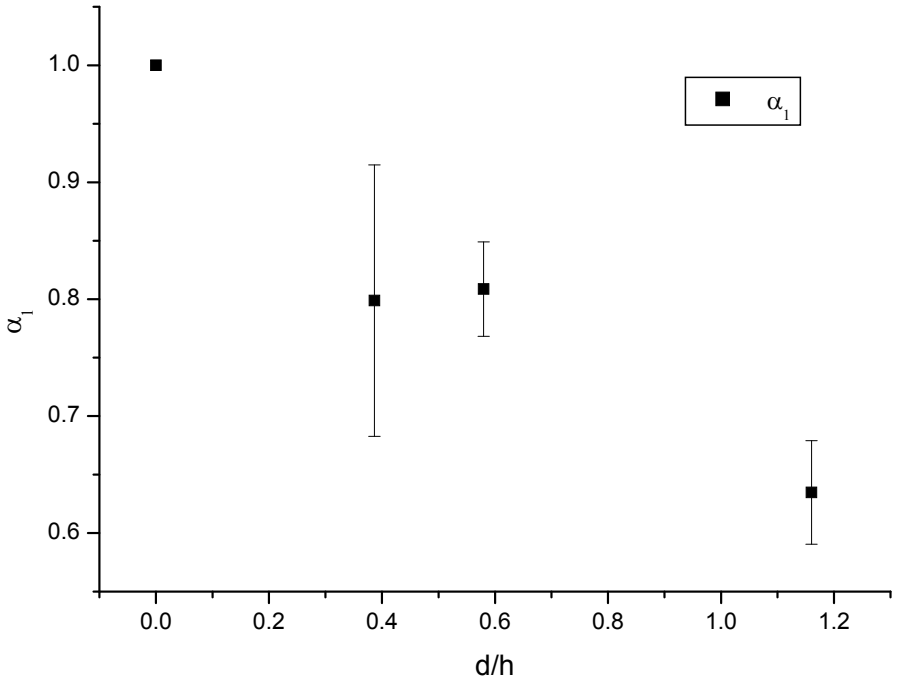

Figure 30: Two components anomalous diffusion model fitting results for the Peg20kDa molecule. On vertical axis is reported the anomalous parameter α against the ratio between molecules diameter and channel height evaluated for the first fitting component.

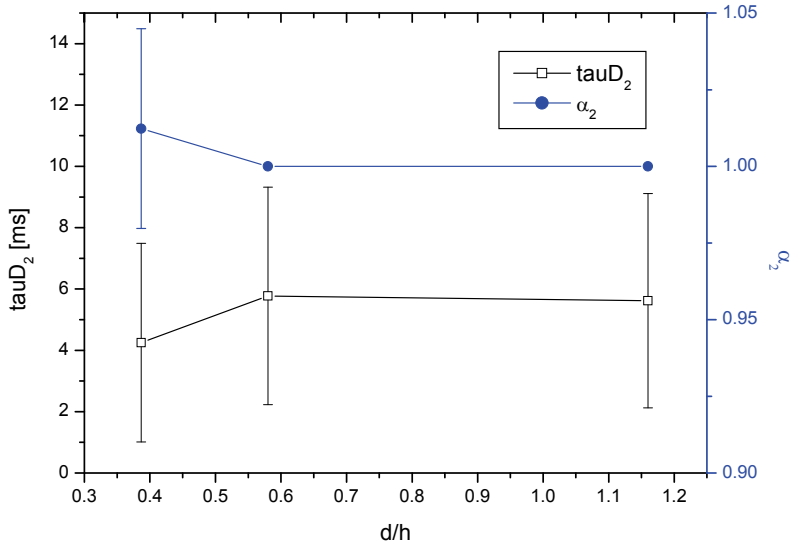

Figure 31: Two components anomalous diffusion model fitting results for the Peg20kDa molecule. On vertical axis we report the diffusion time against the ratio between molecules diameter and channel height; and on the other axis we report the anomalous parameter α. Both parameters are results for the second fitting component.

As we can see from figures 15 and 16, there is not evident influence of channel confinement to Rhodamine 6G motion. Autocorrelation function of different channel dimensions investigated substantially overlap. The diffusion time calculated from the fitting procedure stays quite constant as expected from the autocorrelation function shape. This is quite meaningful if we notice that Rhodamine 6G is a pretty small molecule whose diameter is not much larger than 1 nm. Therefore such a small molecule might not even feel the confinement being at least 10 times its size. Similar results were found also with two-photon excitation FCS in nanoslits of 50 nm height [2] and in classic FCS [15], whereas influence of confinement was observed by a macroscopic technique in higher channels of 260 nm for FITC molecules [16]. This molecules have comparable size with Rhodamine 6G but different chemistry which was not tested in our study as FITC gives high photo bleaching. Anyway we do not believe this could generate such a high reduction in the mobility measured.

On the other hand we do find an increased diffusion time for higher molecular weight molecules, Dextran 40kDa and Dextran 70kDa when channel size gets smaller. For fitting procedures of autocorrelation functions of higher MWs molecules we needed a two components model with a fast anomalous component [17]. Thus at short time we perceive the system as having a non linear dependence with time, but at longer times diffusion becomes normal. We take into account for our discussion the first component of our fitting model, as we believe the second come from long tail kinetics due to sorption to channel walls. The reduction in motion measured by FCS for higher MWs molecules means that even if confinement is exerted on the vertical axis, the system slows down on the xy plane. Motion in the horizontal plane is then hindered by vertical confinement. Diffusion time increases as channel height gets smaller for Dextrans and Peg molecules. The anomaly parameter α follows a decreasing trend with decreasing channel height, suggesting that the anomaly grade is related to the system size. Moreover what could be inferred from results is that the system is approaching a square root dependence with time, which is the theoretical limit for single-file diffusion.

We have not presented data for Dextran 70kDa molecule from the 10 nm channels height because we could not measure any motion in this systems. After 24 h nanochannels were not fully loaded yet, but only 50 μm above the entrance were fluorescent and filling was almost the same after 36h as can be seen in the pictures 32 below.

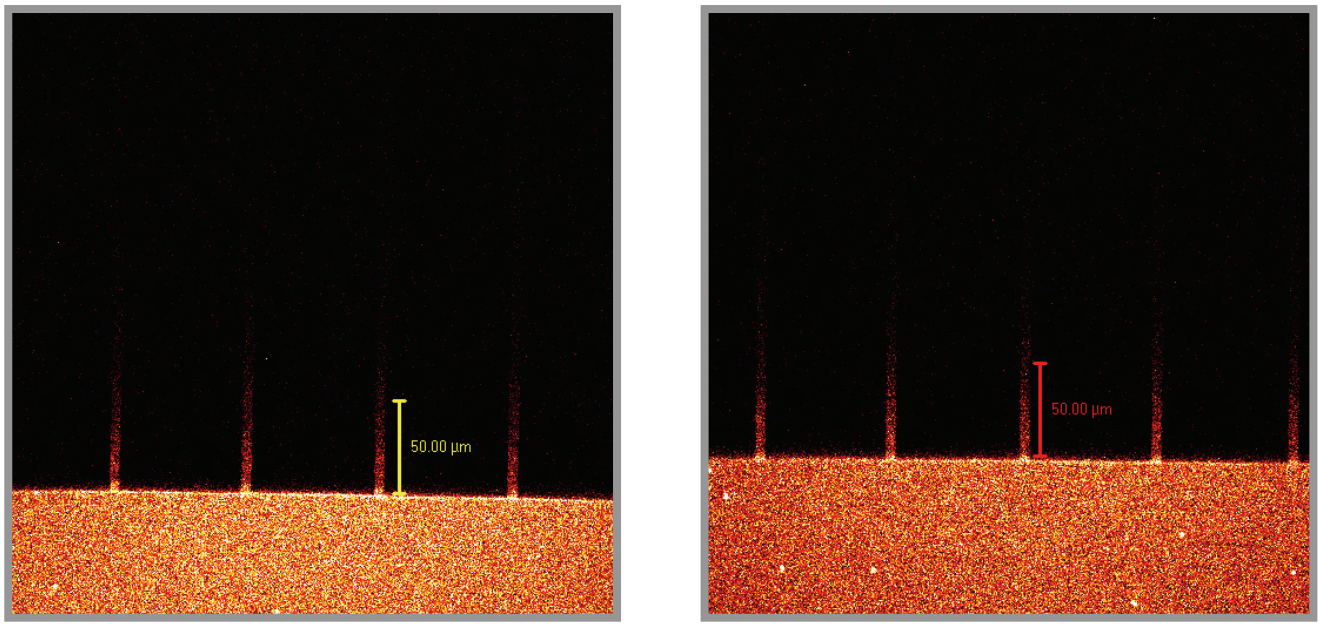

Figure 32: Confocal micrograph of a 10 nm height and 5 µm width channel loaded with 100 nM Dextran 70kDa. Left: Loading after 24h. Right: Loading after 36 h. Scale bar: 20 µm.

Our results from the Dextran 70kDa in 20 nm channel height are confirmed by FRAP (Fluorescence Recovery After Photobleaching) measurements. We performed FRAP measurements in nanochannels of 30 µm width and 20 nm height of Dextran70kDa-FITC. Our measured diffusion coefficient was 4 E-8 cm^2/s which is one order of magnitude lower than the bulk value for the same system of 2.8 E-7 cm^2/s, and comparable to 4.9 E-8 cm^2/s as measured from FCS experiments.

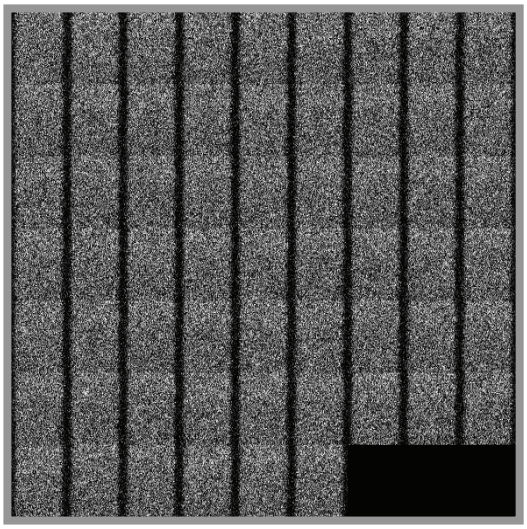

Figure 33: Montage of a FRAP experiment with Dextran 70kDa-FITC molecules in channels of 20 nm height. Montage was then analyzed by SFA with a custom written Matlab code and a diffusion coefficient of 4E-8 cm^2/s was evaluated.

However our results do not agree with the four orders of magnitude increase in diffusion coefficient found in 50 nm height channels for wheat germ agglutinin proteins [18]. We did not test proteins in our study but both Dextran 70kDa and PEG 20kDa show hydrodynamic radius bigger than wheat germ agglutinin protein, and in our findings both molecules do not perceive such high grade of confinement in our bigger channels of 30 nm height.

Finally, if we compare the different chemistry employed of Dextran 40kDa and PEG 20kDa, they have almost the same hydrodynamic radii which means that Dextrans have a more globular shape compared to PEG. This might cause a diverse mechanism under confinement. In fact Dextrans seem to feel less gradually the confinement, but as soon as we overcome the confinement ratio d/h of 1.5 Dextrans are expected to increase their diffusion time in a very steep way, as we measured no motion for d/h of 1.8 in the case of Dextran 70kDa in 10 nm slits. We could not test a higher grade of confinement for PEG molecules to verify the diverse mechanism because this molecule becomes highly unstable over 20kDa.

CONCLUSIONS

We have performed Fluorescence Correlation Spectroscopy measurements of molecular motion in solid confined geometries of glass nanoslits as small as 10 nm in height. Both small molecules such as Rhodamine 6G and high molecular weight molecules such as Dextrans 40 and 70 kDa and Peg 20 kDa were employed in order to investigate at a single molecule level the influence of size, chemistry and flexibility on confined diffusion.

From our results Rhodamine 6G seems to be quite unaffected from confinement ($d/h < 0.2$) whereas all macromolecules show a reduction of their diffusion coefficient of almost one order of magnitude with an anomaly parameter approaching the single –file limit of 0.5 in the case of strong confinement ($d/h > 1$). In particularly Dextran molecules of 70kDa showed no motion in the strong confinement case of $d/h = 1.8$.

More experimental work is needed to develop a complete scenario. Our study provides new experimental data for future improvement of theoretical models of diffusion in confined geometries.

References

1. Hell S.,W., Wichmann J, “Breaking the diffraction resolution limit by stimulated – emission-depletion fluorescence microscopy”, *Optics Letters*, **19**, 11, 780 (1994)
2. Petrasek Z. Krishnann M, Monch I, Schwille P “Simultaneous Two-Photon Fluorescence Correlation Spectroscopy and Lifetime Imaging of Dye Molecules in Submicrometer Fluidic Structures” *MICROSCOPY RESEARCH AND TECHNIQUE* **70**:459–466 (2007)
3. Elson E. L., Magde D” Fluorescence correlation spectroscopy I, Conceptual basis and theory” *Biopolymers* **13**, 1 (1974)
4. Lakowicz, J.R., “Principles of Fluorescence Spectroscopy”, third edition, Plenum Press, New York, (2006)
5. Betzig E, G. H. Patterson, R. Sougrat, O. W. Lindwasser, S. Olenych, J. S. Bonifacino, M. W. Davidson, J. Lippincott-Schwartz, H. F. Hess, “Imaging Intracellular Fluorescent Proteins at Nanometer Resolution” *Science* **313**, 5793 , 1642, (2006)
6. Pawley J.B., “Handbook of Biological Confocal Microscopy”, third edition, Springer Science and Business. New York, (2006)
7. Aragon, S. R., and R. Pecora.. Fluorescence correlation spectroscopy as a probe of molecular dynamics. *Journal of Chemical Physics.* **64**:1791–1803. (1976)
8. Rigler, R., U Mets, J. Widengren, and P. Kask.. ”Fluorescence correlation spectroscopy with high count rate and low background: analysis of translational diffusion”. *Eur. Biophysic. Journal Biophysical Letters.* **22**:169 –175. (1993)
9. Rigler R., Elson E. L., ” Fluorescence Correlation Spectroscopy: Theory and Applications” Springer Berlin (2001)
10. Thompson N. L., “ Fluorescence correlation spectroscopy “ in Topics in fluorescence Spectroscopy, J. R Lakowicz, ed, vol 1, Plenium Press, New York, (1991)
11. Widengren, J., Mets, UÈ . & Rigler, R. “Fluorescence correlation spectroscopy of triplet states in solution: a theoretical and experimental study”. *Journal of Physical Chemistry*. **99**, 13368-13379. (1995).
12. Bunde, A. & Havlin, S., Eds. “Fractals and Disordered Systems”, 2nd edit., pp. 115-175, Springer-Verlag, Berlin. (1995)

13. Saxton, M. J ”Anomalous diffusion due to obstacles: a Monte Carlo study”. *Biophysical Journal*. **66**, 394-401. . (1994).
14. Gennerich A. and Schild D “Fluorescence Correlation Spectroscopy in Small Cytosolic Compartments Depends Critically on the Diffusion Model Used” *Biophysical Journal* **79** 3294–3306, (2000)
15. Pappaert K, Biesemans J., Clicq D., Vankrunkelsven S., Desmet G.,” Measurements of diffusion coefficients in 1-D micro- and nanochannels using shear-driven flows”, *Lab on a Chip,* 5, 1104-1110, 2005.
16. Foquet M.,Jonas Korlach J., Zipfel W. R., Webb W. W., and. Craighead H. G ”Focal Volume Confinement by Submicrometer-Sized Fluidic Channels” *Analytical Chemistry*. **76**, 1618-1626, (2004),
17. Wawrezinieck L. Rigneaul H, Marguet D., Lenne P.F. ,“Fluorescence Correlation Spectroscopy Diffusion Laws to Probe the Submicron Cell Membrane Organization *Biophysical Journal*. **89**, 4029–4042, (2005)
18. Durand N F. Y. Bertsch A., Todorova M., and. Renaud P “Direct measurement of effective diffusion coefficients in nanochannels using steady-state dispersion effects” *Journal of Applied Physics Letters* **91**, 203106 (2007)

CHAPTER 7

Simulation of dynamical properties of molecules confined in nanochannels

In the last two decades a lot of simulation work has been done to unravel transport properties of molecules on the nanoscale. However the most relevant results are still on a atomistic scale, thus presenting mainly simple fluids behavior. Taking into consideration just water on the atomistic scale is already enough challenging because of moment dipole considerations, hydrogen bonding interactions, tetrahedral structure and so on. However the main interest for most engineering applications are macromolecules. Therefore it seems necessary to switch to a different simulation tool.

Main interest of this work is the understanding of molecular motion on the nanoscale in order to develop simulation recipes for macroscopic applications. A possibility to study molecules behavior at the nanoscale is to match atomistic and mesoscopic simulation in a multiscale modeling technique. In fact Molecular Dynamics method are limited to simulating the dynamics of a few thousand molecules over a few nanoseconds, therefore being inadequate for the simulation of physical processes that occur on the microsecond (or longer) time scale.

DPD (Dissipative Particle Dynamics), derived from molecular dynamics simulations and lattice gas automata, effectively opens up the mesoscopic length and time regimes in complex fluids to simulation. In this chapter we present some results from the atomist simulation work in confined geometries, introduce the DPD tool and present our results from DPD simulations.

Atomistic results of confined fluids

Due to the several and complicated interactions involved in complex fluids, most of the nanofluid transport theories developed so far are limited to the atomistic simulation of simple fluids. They are taken as a collection of atoms that interact via the Lennard–Jones potential and which dynamics can be described by Newton's law [1]. A significant result obtained for these confined systems is that depending on the critical length scale of the confinement, the transport behavior can deviate significantly from the bulk behavior. This follows from the fact that the fluid can no longer be considered homogeneous and there are strong oscillations in the fluid density at the solid/fluid interface.

Simple fluids in nanochannels are inhomogeneous because of the strong layering of fluid atoms near the channel wall. Classical fluidic transport theories do not account for the inhomogeneity and both diffusivity and viscosity are strongly affected by the fluid layering on the nanochannels wall. Fluid layering can be influenced by various parameters such as, fluid-wall interactions, wall structure and channel width. Relevant results in the investigation of the fluid-wall interactions parameter's influence in nanofluid transport show that the tendency of a fluid atom to stay close to the wall increases with the increase in the attractive force exerted by the wall atoms on the fluid and leads to the formation of boundary liquid layers of higher density than in the case of repulsive wall-fluid interactions.

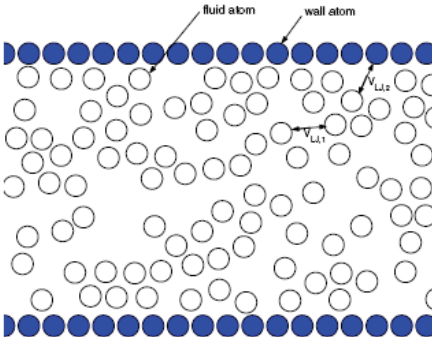

$$V_{LJ} = 4\epsilon \left[\left(\frac{\sigma}{r}\right)^{12} - \left(\frac{\sigma}{r}\right)^{6} \right]$$

Figure 1: Cartoon of simple fluids in a nanochannel. Fluid is represented by a Lennard–Jones potential

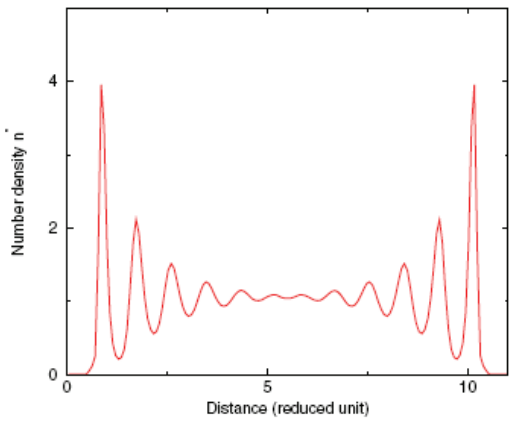

Figure 2: Density profile simulation for a LJ fluid in a11 fluid atomic diameter channel

Anyway the density distribution of fluid atoms is sensitive to both the fluid-wall interactions and fluid-fluid interactions. It was simulated also the density distribution along the unconfined direction, and it is shown that the fluid is highly structured also along the channel length [2].

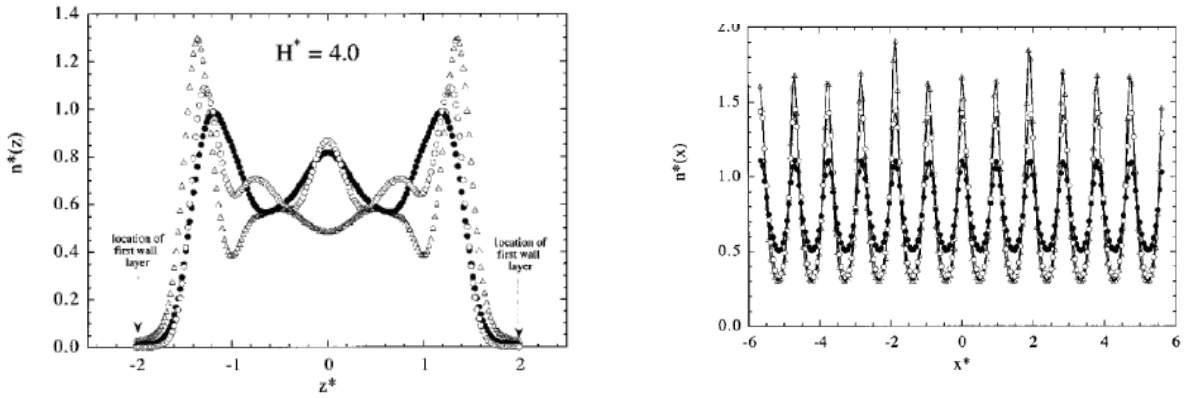

Figure 3: Number density profiles across (a) and along (b) a 4.0σ-wide slit channel for three different cases where the fluid–fluid and fluid–wall interactions are modelled differently (only repulsive w-f, f-f , filled circles, LJ system, open circles, and both WCA-LJ potentials, open triangles).

The diffusion of fluids confined in nanoscale channels has been studied extensively in slit and cylindrical pores. In a slit pore, diffusion is different in the direction parallel (the *x*- and *y*-directions) and normal (*z*-direction) to the pore wall, especially for narrow pores. This is because, unlike the diffusion parallel to the pore wall, the diffusion in the direction normal to the pore wall is inherently transient; in the long time limit, the diffusivity in the direction normal to the pore wall is zero due to the geometrical limit. To avoid this problem, the diffusion in the *z*-direction is usually characterized by a mean-square displacement $\Delta z^2(t)$ that is evaluated over the short time range. Magda et al. studied diffusion in slit smooth pores with MD simulations. They showed that D_{II} is a function of pore width. It first fluctuates with pre width dimension and then smoothly increases towards the bulk value. Also the average density variation does change with the pore width [3].

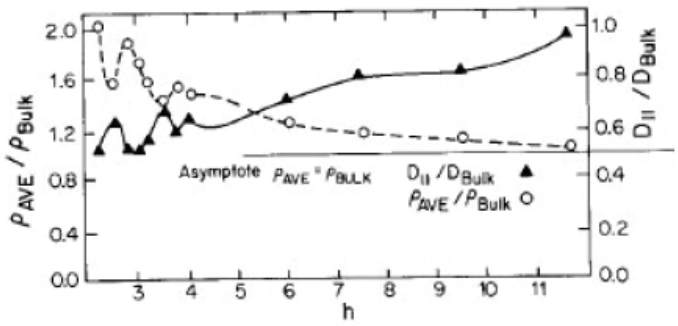

Figure 4: Correlation of the pore-averaged diffusivity parallel to the wall(D_{II}) with the average fluid density. *h* is the pore width (in reduced unit);ρ_{ave}/ρ_{bulk} is the average density of the occupied pore volume divided by the density of the bulk liquid.

The diffusivity on the z direction can not be calculated from the Stokes Einstein relationship as usual but can be evaluated from the mean square displacement $\Delta z^2(t)$ at a short time. Davis et al. evaluated also the comparison of the mean square displacement in the direction normal and parallel to the channel wall. What they calculated is a faster diffusion process on the x-y plane compared to the one on the z direction and as the channel gets higher, the diffusivity increases and tends to the x-y plane value.

Another interesting aspect in confined nanostructures is the possibility for a diffusive process to follow a dynamic different from the normal mode diffusion, which is linear dependence over time of the MSD Mao and Sinnot in 2000 found in carbon nanotubes smaller than 1 nm in diameter the transition from the normal mode to the single file mode, which is expressed as: $\langle r(t)^2 \rangle \propto \Gamma t^{0.5}$. They found smaller molecules such as methane followed normal diffusion dynamic, whether ethane switched towards single file diffusion in with a transition mode (time exponent in the range 0.5-1)[4].

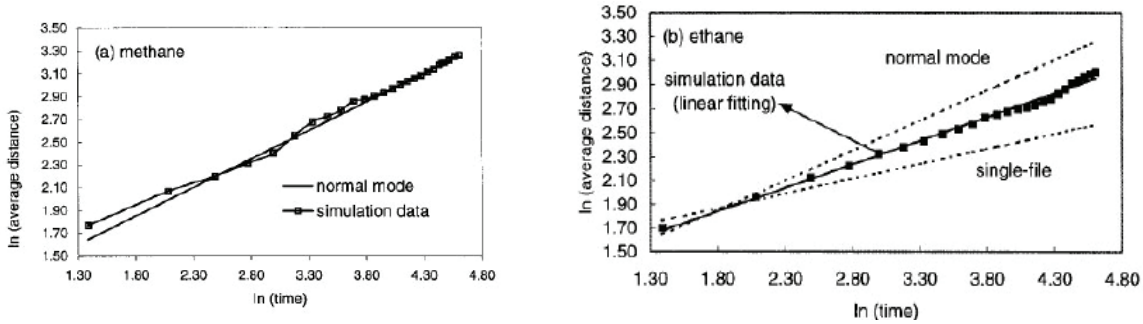

Figure 5: Log-log plot of the mean-square displacement for methane (a).left, ethane (b) right, in a (10, 0) carbon nanotube (diameter: 0.8 nm).

There is an extensive literature also on confined water both on surfaces, cylindrical pores and cavities. The major attention has been paid to the investigation of its static and dynamic properties in respect to the degree of confinement, surface properties and presence of surface charge. Clearly, the geometrical confinement alters the behavior of water from that in the bulk, and the effects of different types of surfaces make this behavior further complicated. Also the presence of charges on a pore surface can influence the density distribution, dipole orientation and the average water dipole moment. The number of hydrogen bonds per molecule decreases in hydrophobic channels as the confinement increases. In hydrophilic channels it does not depend on the pore dimension, but only by taking into account water-water interactions, then the number decreases as well. This is because water molecules loose water-water hydrogen bonds in order to establish bonds

with the wall atoms. As water creates bonds with fix walls, this may result in a reduced mobility. Anyway, pure geometrical confinement was demonstrated to be alone responsible for the reduction in number of hydrogen bonds at the interface. Some dynamic properties of water can indeed give more information about the diffusion transport in nanoconfined structures compared to static information. Martì et al showed that the molecular dipole moment reorientation time is smaller as confinement gets stronger, and that was simulated in different nanotubes dimensions. The confinement tends to speed up molecular reorientation and this can be attributed to the partial breakdown of the tetrahedral hydrogen bond network. While the reorientation time gets smaller, the mean time spent by a molecule of water in its first coordination shell, which is called the residence time, increases with confinement [5].

More interestingly the mean square displacement in the pore axis was found to deviate from that in the bulk in a non strictly size dependent manner. In particular at 8.6A° pore radii the water structure seems to be immobilized in a frozen structure. The normalized to bulk diffusion coefficient of water extrapolated from the MSD reported previously are shown below. Still in a 4 nm diameter tube, diffusion is 20% lower than in bulk[6].

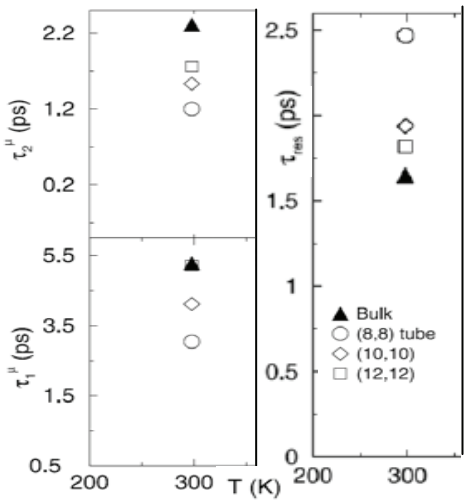

Figure 6: Left: Molecular dipole moment reorientation time τ^{μ}. Right: Residence time τ_{res} of a water molecule in its first coordination shell in different-sized nanotubes.

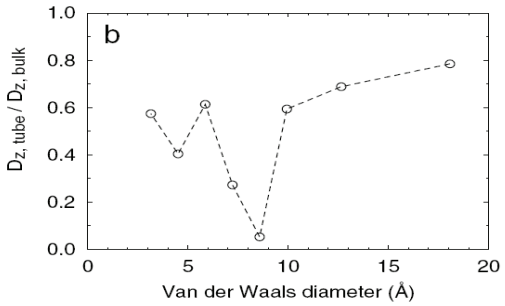

Figure 7 : Axial diffusion coefficient of water normalized to the bulk value 2.69x10-5 cm^2/s

Multiscale modeling

The most accurate method of simulating the dynamics of an atomistic system is to integrate the equation of motion for all atoms in the system. This is the basis of the molecular dynamics (MD) simulation method. The major drawback of this method is that it reproduces every aspect of the atomic motion, which is often far too detailed to allow an understanding of physical processes. Moreover, with current computer processor speeds and memory capacities, the MD method is limited to simulating the dynamics of a few thousand molecules over a few nanoseconds. This renders the MD method inadequate for the simulation of physical processes that occur on the microsecond (or longer) time scale.

Some years ago, Hoogerbrugge and Koelman introduced a new simulation technique, DPD (Dissipative Particle Dynamics), derived from molecular dynamics simulations and lattice gas automata, that effectively opens up the mesoscopic length and time regimes in complex fluids to simulation. The technique achieves this goal by keeping the principle of integrating an equation of motion, but now for a system in which the smallest spatial degrees of freedom are averaged out. The fast motion of the atoms in such a system is averaged over and the remaining structure is represented by a set of 'beads', of given mass and size, that interact via soft potentials with other beads.

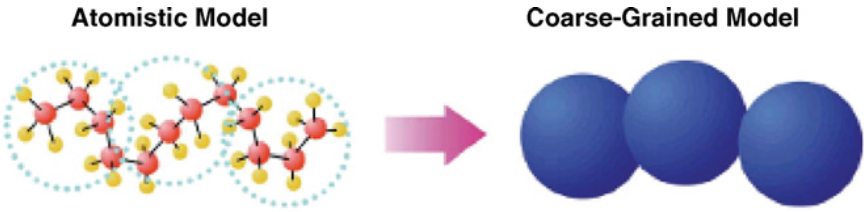

Figure 8: Cartoon of a Coarse grained modeling from an atomistic model

A bead represents a small region of fluid matter and its motion is assumed to be governed by Newton's laws. There are three types of force between pairs of beads, each of which conserves both bead numbers and linear momentum: a harmonic conservative interaction, a dissipative force representing the viscous drag between moving beads (i.e., fluid elements), and a random force to maintain energy input into the system in opposition to the dissipation. All forces are short range with a fixed cutoff radius. Integration of the equations of motion for the beads generates a trajectory through the system's phase space from which all thermodynamic observables (e.g., density fields, order parameters, correlation functions, stress tensor, etc.) may be constructed from suitable averages[7].

The building block parameter of a mesoscale modeling technique is principally the molecule chain. The intra-chain correlations can, in principle, be treated by any suitable model. In practice, a Gaussian chain model is considered because it allows a factorization of the interactions; hence it is computationally very efficient. It can be proved that a Gaussian chain may be used as a statistical model for a real chain; therefore, for each real, atomistic force field model, a Gaussian chain representation with the same response function can be found. In the hypothesis of Gaussian chain, the systems needs parameters to determine the number *n* and the length *a* of the beads (Kuhn segment). To reduce computational time to reasonable limit, the molecular weight of each chain can be scaled by a given numeric factor, for instance 10. The resulting polymer chains are mapped onto Gaussian chains by imposing that both the real and the Gaussian chain have the same mean square end-to-end distance and length of the fully extended chain.

Thus, the number (*n*) and the length (*a*) of the Gaussian chain segments are estimated by the following relationships:

$$a = C_\infty l \tag{1}$$

$$n = \frac{N}{C_\infty} 1 \tag{2}$$

where *N* is the degree of polymerization, *l* the monomer unit length, and C_∞ is the characteristic ratio of an infinite length chain. The characteristic ratio represents the stiffness of the chain and can be evaluated from:

$$C_\infty = \frac{\langle r^2 \rangle_0}{Nl^2}; \tag{3}$$

with $l^2 = \sum_i^N l_i^2$ (4)

where *N* is the number of monomers, *l* the monomer length and $\langle r^2 \rangle_0$ is the mean end-to-end distance. If the chain has *N* monomers with a length *l*, this can be approximated to a freely jointed equivalent chain with a number of segments *n* and a bond length *a*. Thus conditions that must be respected are:

$$\langle r^2 \rangle_0 = C_\infty N l^2 = na^2 \tag{5}$$

$$na = l_{\max} \tag{6}$$

Thus the conditions reported which define both *a* and *n* are found. The value of *N* can be obtained from the molecular weight of the polymer; whereas C_∞ is an intrinsic property of the chain[8].

DPD Theory**:** In the dissipative particle dynamics simulation method [7], a set of particles moves according to Newton's equation of motion and interacts in a dissipative way through simplified force laws. If the mass of all particles is set equal to unity, the time evolution of the positions ($\mathbf{r}_i(t)$) and momentum ($\mathbf{p}_i(t)$) is given by the well-known relationships:

$$\frac{dr_i}{dt} = v_i(t) \tag{7}$$

$$\frac{dv_i}{dt} = f_i(t) \tag{8}$$

where the mass of each particle *i* is set to unity and $\mathbf{r}_i$, $\mathbf{v}_i$, and $\mathbf{f}_i$ are the position vector, velocity, and total force, respectively, acting on particle *i*. The force acting on the particles, which is pair-wise additive, can be decomposed into three elements: a conservative ($\mathbf{F}_{ij}^{C}$), a dissipative ($\mathbf{F}_{ij}^{D}$), and a random ($\mathbf{F}_{ij}^{R}$) force. Accordingly, the effective force $\mathbf{f}_i$ acting on a particle *i* is given by:

$$\mathbf{f}_i = \sum_{i \neq j} (\mathbf{F}_{ij}^{C} + \mathbf{F}_{ij}^{D} + \mathbf{F}_{ij}^{R}) \tag{9}$$

where the sum extends over all particles within a given distance, r_c, from the *i*th particle.

This distance practically constitutes the only length scale in the entire system. Therefore, it is convenient to set the cutoff radius, r_c, as a unit of length (i.e., $r_c = 1$), so that all lengths are measured relative to the particle radius. The conservative force is a soft repulsion, given by

$$\mathbf{F}_{ij}^{C} = \begin{cases} a_{ij}(1 - r_{ij})\hat{\mathbf{r}}_{ij} & (r_{ij} < 1) \\ 0 & (r_{ij} \geq 1) \end{cases} \tag{10}$$

where a_{ij} is the maximum repulsion between particles *i* and *j*, r_{ij} is the magnitude of the particle-particle vector $\mathbf{r}_{ij} = \mathbf{r}_i - \mathbf{r}_j$ (i.e., $r_{ij} = |\mathbf{r}_{ij}|$, and $\hat{\mathbf{r}}_{ij} = \mathbf{r}_{ij} / r_{ij}$ is the unit vector joining particles *i* and *j*. The other two forces, $\mathbf{F}_{ij}^{D}$ and $\mathbf{F}_{ij}^{R}$, are both responsible for the conservation of the total momentum in the system and incorporate the Brownian motion into the larger length scale. They are given by the following expressions:

$$\mathbf{F}_{ij}^{D} = -\gamma \omega^{D}(r_{ij})(\hat{\mathbf{r}}_{ij} \cdot \mathbf{v}_{ij})\hat{\mathbf{r}}_{ij} \tag{11}$$

$$\mathbf{F}_{ij}^{R} = \sigma \omega^{R}(r_{ij})\theta_{ij}\hat{\mathbf{r}}_{ij} \tag{12}$$

where $\mathbf{v}_{ij} = = \mathbf{v}_i = - \mathbf{v}_j$, ω^{D} and ω^{R} are *r*-dependent weight functions tending to zero for $r = r_c$, and θ_{ij} is a randomly fluctuating variable with zero mean and unit variance. Espanol and

Warren have shown that one of the two weight functions can be chosen arbitrarily, thereby fixing the other weight function. However, the weight function and constants should obey:

$$\varpi_{\mathrm{D}}(r_{ij}) = \left[\varpi_{\mathrm{R}}(r_{ij})\right]^2 \tag{13}$$

$$\gamma = \frac{\sigma^2}{2k_{\mathrm{B}}T} \tag{14}$$

where the first equation is the fluctuation-dissipation theorem, k_B is the Boltzmann constant. γ σ ω_R ω_D are yet to be defined [9]. Finally, using a Verlet-type algorithm the simulation is found to be stable and efficient if:

$$3 < \sigma < 8 \qquad \varpi_{\mathrm{D}}(r_{ij}) = \left[\varpi_{\mathrm{R}}(r_{ij})\right]^2 = \begin{cases} \left(1 - \frac{r_{ij}}{r_c}\right)^2 & \text{if } r_{ij} < r_c \\ 0 & \text{else} \end{cases} \tag{15}$$

In the DPD model, individual atoms or molecules are not represented directly by the particle, but they are coarse-grained into beads. These beads represent local “fluid packages” able to move independently. Incorporation of chain molecules simply requires the addition of a harmonic spring force between the beads:

$$\mathbf{F}_{ij}^{\text{spring}} = K\mathbf{r}_{ij} \tag{16}$$

By means of this spring, the beads can interconnect to highly complex topologies. In order to derive information on the mesoscopic scale it is necessary to define the aij: bridging parameters which link the macro world to the mesoscale world. The job is easy in the case of polymers with χ_{AB}>3, where χ_{AB} is the Flory Huggins parameter. In fact it has been demonstrated that:

$\chi_{AB} = (0{,}286 \pm 0{,}002)(a_{AB} - a_{AA})$ In case of DPD ρ= 3

$\chi_{AB} = (0{,}689 \pm 0{,}002)(a_{AB} - a_{AA})$ In case of DPD ρ= 5

From the free energy comparison of a polymer in DPD framework with Flory Huggins theory [10].

Another millstone in DPD technique comes from the study of the compressibility of water in DPD framework. In fact it has been demonstrated that from

$$a_{AA} = \frac{75 k_B T}{\rho} \tag{17}$$

It follows:

$a_{AA}=25$ In case of DPD ρ= 3

$a_{AA}=15$ In case of DPD ρ= 5

Where $k_B T$ is the unit Energy of the DPD system. From this results it follows that in the case of good and poor solvents it can be computed :

$\Delta a = a_{sp} - 1/2(a_{ss}+a_{pp})$ (18)

From eq. 18 we can derive:

Good Solvent: $a_{sp} < 25$ (19)

Poor solvent: $a_{sp} > 25$ (20)

The aij parameters are anyway strictly linked to the chemistry of the system taken into account [10].

In order to match the atomistic simulation model and the mesoscopic system derived it is important to consider the data obtained from the molecular dynamics simulation carried out and evaluate the binding energies, the radial distribution functions and all the parameters which derive directly from the system chemistry [11-14].

Dissipative Particle Dynamics simulation of PEG molecules in nanochannels

In order to compare our single molecule results and derive a model which could provide macroscopic engineering information, we developed a mesoscale model of our experimental system mainly focusing on glass nanoslits of 30 nm height loaded with Peg 20kDaand 5kDa molecules.

MODEL BUILDING

After being sketched, the geometry of the PEG molecule was optimized using the *Compass* force field (FF)[15]. The choice of the *Compass* FF resulted from a compromise between good accuracy and availability of force field parameters for all atom types present in the molecular model. The molecule conformational search was carried out using a well-validated combined molecular mechanics/molecular dynamics simulated annealing (MDSA) protocol,[16] in which the relaxed molecular structure is subjected to five repeated temperature cycles using constant volume/constant temperature (NVT) MD conditions. At the end of each annealing cycle, the structure is again energy minimized, and only the structure corresponding to the minimum energy is used for further modeling. We built 2 different configurations of three PEG chains at 298 K. This was achieved by using the *Amorphous Cell* module of *Materials Studio*, which uses a version of the RIS method [17] for generating polymer chain configurations. In short, the procedure consisted of building and optimizing the polymer constitutive repeating unit (CRU) again using the *Compass* FF, which was then polymerized to a conventional degree of polymerization (DP) equal to 15. Each polymeric structure was then relaxed and subjected to the same MDSA protocol. Each final chain structure was assigned atomic charges using the charge scheme proposed by Li and Goddard [18].

MD SIMULATION INTERACTION AND BINDING ENERGIES.

Resorting to atomistic MD simulations in the NVT ensemble allows the retrieval of important information on the interaction and binding energy values between the different components of our system. The technique basically consists of simulating the interface between the glass substrate and the polymer by building a cell from which the binding energies between all system components can be calculated. According to our procedure, we first separated the two glass layers by 39 Å, as we wanted to keep constant in our

atomistic framework the ratio between the molecule dimension and the channel height. Taking into consideration a nanoslit of channel height 30 nm and first Peg 5kDa, its end-to-end distance is approximately 28nm and then, 28/30 = 0.93. We choose for instance a Peg of 15 cru which has and end to end distance of about 35Å, in order to keep the ratio 0.93 it follows an atomistic channel height H of 39 Å.

height = 39 Å
width = 42,78Å
length = 85,57 Å

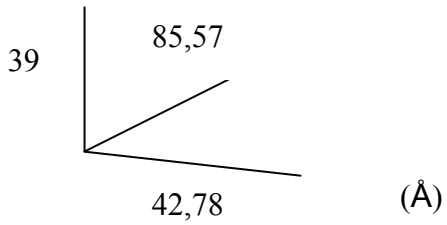

The NVT simulations were performed with the *Materials Studio Disco*V*er* module, using the *Compass* FF and the charge scheme described previously. Each NVT simulation was run at 298 K for 500 ps, applying the Ewald summation method for treating both van der Waals and electrostatic interactions. An integration time step of 1 fs and the Nose´ thermostat (*Q* ratio = 1) were also adopted [19-20]. For the interaction energy calculations ΔE, we started from the total potential energy of the ternary system composed of PEG (Peg), water (w) and silicon (Si) which can be written as:

$$\Delta E_{(Peg+Si+W)} = E_{Peg} + E_w + E_{Si} + E_{(Peg+w)} + E_{(Peg+Si)} + E_{(w+Si)} \quad (21)$$

where the first three terms represent the energy of PEG, water and silicon, (consisting of both valence and nonbonded energy terms) and the last three terms are the interaction energies between each of two component pairs (made up of nonbonded terms only). To calculate the interaction energy ΔE_{Peg+Si} for instance, we first created a system with both Peg molecules and a silicon shit from one of the equilibrated MD trajectory frames and then calculated the potential energy of the system $E_{(Peg+Si)}$. Next, we deleted the silicon sheet molecules, leaving the Peg chains alone, and thus calculated the energy of the Peg molecules (E_{Peg}). Similarly, we deleted the Peg molecules from the system and calculated E_{Si}. Then, the interaction energy ΔE_{Peg+Si} can be calculated from the following equation:

$$\Delta E_{Peg+Si} = E_{(Peg+Si)} - (E_{Peg} + E_{Si}) \quad (22)$$

As the MD frame choice is concerned, we decided to calculate the system energies at 400 ps. We considered these as representative energy values, since every energy component was well equilibrated after approximately 100 ps of simulation. All data collected have then been averaged over the 10 different model systems.

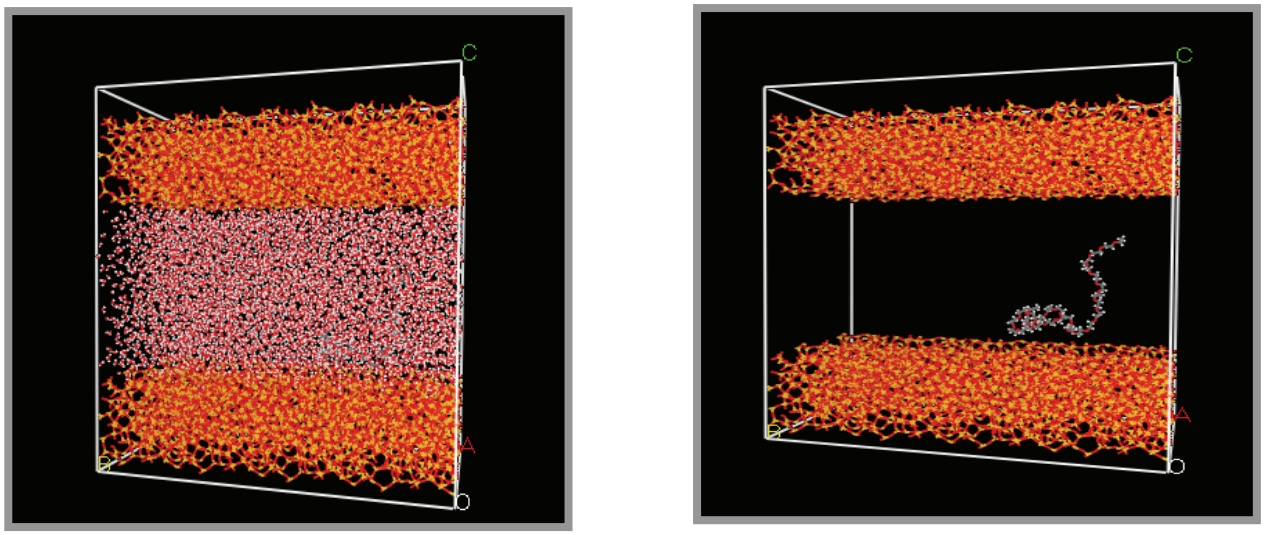

Figure 9: Left: Atomistic simulation of two sheets of Silicon, filled with water molecules and a PEG molecule. Right, without water molecules.

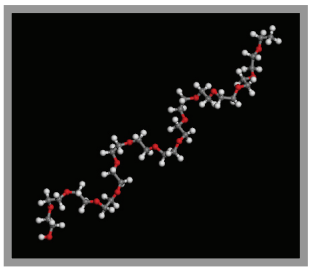

Figure10: Atomistic representation of a PEG molecule

The interaction energies results evaluated from eq 21, 22, at frame 400 ps; (Kcal / mol) are listed below:

E_{Peg} =175,71 (nb 154,6)

E_{Si} = 0 fixed

E_W = -39800,12 (nb -47759,74)

E_{Peg1} = 106,16 (nb 82,93)

E_{Peg2} = 69,57 (nb 71,68)

$E_{(Peg+Si)}$ = 161,6(nb 140,46)

$E_{(Peg+W)}$ = -39841 (nb -47822,73)

$E_{(W+Si)}$ = -40601,49 (nb -48561,12)

$E_{(Peg1+Si)}$ = 103,76 (nb 80,53)

$E_{(Peg1+W)}$ = -39810 (nb -47792,90)

$E_{(Peg2+Si)}$ = 58,06 (nb 60,17)

$E_{(Peg2+W)}$ = -39832,03 (nb -47789,55)

$\Delta E_{Peg+Si} = E_{(Peg+Si)} - (E_{Peg} + E_{Si}) = 161,6 - 175,71 = -14,11$

ΔE_{Peg+W} = E ($_{Peg+W}$) -(E_{Peg} + E_W) = -39841,97 – (175,71-39800,12) = -217

$\Delta E_{Peg1+Si}$ = E ($_{Peg1+Si}$) -(E_{Peg1} + E_{Si}) = 103,76-106,16 = -2,36

ΔE_{Peg1+W} = E ($_{Peg1+W}$) -(E_{Peg1} + E_W) = -39810,04 – (106,16 -39800,12) = -116,08

$\Delta E_{Peg2+Si}$ = E ($_{Peg2+Si}$) -(E_{Peg2} + E_{Si}) = 58,06 – (69,57) = -11,51

ΔE_{Peg2+W} = E ($_{Peg2+W}$) -(E_{Peg2} + E_W) =-39832,07 – (69,57 -39800,12) = -101,52

ΔE_{W+Si} = E ($_{W+Si}$) -(E_w + E_{Si}) = -40601,49 -(-39800,12) = -801,37

DPD SIMULATIONS.

In order to simulate the dynamical behavior of Peg polymers under nanoscopic confinement at a mesoscopic level, we used the DPD simulation tool as implemented in the *Materials Studio* modeling package. In the framework of a multiscale approach to Peg simulation, the interaction parameters needed as input for the mesoscale level DPD calculations have been obtained by a mapping procedure of the binding energy values between different species obtained from simulations at atomistic scale. The first step necessary for the determination of the DPD input parameters generally consists of defining the DPD bead dimensions, thus implicitly defining the characteristic length of the system (*r*c). As illustrated before, the interaction range *r*c sets the basic length scale of the system; in other terms, *r*c can be defined as the side of a cube containing an average number of ρ beads. Therefore,

$$r_c = (\rho V_b)1/3 \quad (23)$$

where V_b is the volume of a bead. Thus, even in a heterogeneous system consisting of several different species, a basic DPD assumption is that all bead types (each representing a single species) are of the same volume, V_b.

Starting with the PEG molecules, we considered them as being made up of all same kinds of beads. Each monomer unit of Peg has a molecular weight of 44.05 Da. We wanted to simulate Peg polymers of 5kDa and 20kDa which have 113 and 455 monomers each. It could be computed with the Connolly algorithm the monomer volume also named as Van der Waals volume [21]. It was found to be 53.17 Å3. Moreover with the Sinthia algorithm we could compute a volume of about 23.31 cm3/mol and a surface of 76.29 Å2. The characteristic ratio for this polymer at 298K was 4.98, therefore we choose 113/4.98=

23 and 455/4.98= 91 beads fro the two molecules. The chosen bead volume had an average value of 266 Å3, that roughly corresponded to that of five single monomers. Once we determined the bead size, and fixed the system density ρ to 3, we could calculate the characteristic dimension of the mesoscopic system (i.e., the cutoff distance (*r*c)) from eq 23, obtaining *r*c = 9.3 Å. As said, this value represents the soft potential cutoff distance but is also the length of one of the unit cells in the DPD simulation box. From the bead volume we could compute also the bead radius rb= 4 Å.

Our DPD system was set in order to respect the most important parameter investigated, which is channel height. In our experimental panel we could take advantage of channels of different heights: 10- 20- 30 nm. We implemented the DPD box unit as to maintain the confinement ratio between molecules size and channel height. Considering as a first case channel height of 30 nm, it was represented in DPD model by 33 units (30nm/9.3Å) then we set the channel box to be constituted of 33X55X84 unit cells in the case of Peg 5kDa and 33X80X100 in the case of Peg 20kDa, and hence characterized by effective dimensions of 30.7nmX51.1nmX78.1nm and 30.7nmX74.4nmX93nm respectively.

MAPPING BRIDGE FROM ATOMISTIC TO DPD

Accordingly, the total number of Peg molecules to be inserted in our DPD box was 6, plus 534 beads of water and 540 beads of silicon which made up 1080 beads in our system.

DPD cell dimensions:

height = 4
width = 5
length = 9

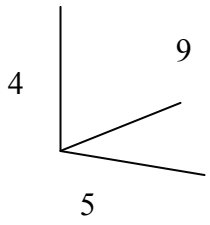

After choosing the bead size, determining system dimensions and bead numbers, we used the binding energies obtained from atomistic MD simulations to calculate the values of the interaction parameters for the DPD simulation. The procedure used to retrieve mesoscale interaction parameters from molecular dynamics binding energies is radically modified from previous methodology based rather to the linkage to the χ parameter in Flory Huggins-type model suggested by Groot and Warren [10] or to the bead size as reported by Maiti and McGrother [12]. In this work, we used an alternative route, in which

the interaction repulsive DPD parameters are coupled to the energy values resulting from the atomistic molecular dynamics simulations. An internal consistency was also established by comparing the density fields obtained by DPD and MD on the same system. Accordingly, the derivation of the conservative repulsion from a lower scale (i.e., atomistic) modeling constitutes a bottom-up, multiscale approach to the simulation of polymers dynamical properties in confined environment. To this purpose, the following combinatorial approach was used to rescale the nonbonded interaction energies listed before. The choice of using only the nonbonded interactions stems from the fact that they represent the most appropriate choice to describe the DPD conservative force (*F*c) as defined by Groot and Warren [10]. As reported in [16] we considered a system made up of single particles *i* and *j*, the total energy of the system is given, in the hypothesis of neglecting the ternary contributions to interaction, by

$$E_{system} = n_{ii}E_{ii} + n_{jj}E_{jj} + n_{ij}E_{ij} + n_{ji}E_{ji} \quad (24)$$

Where each energy term is computed as below:

$$E_{ii} = (E_{nb})^{i} / n_{ii} \quad (25)$$

$$E_{ij} = (E_{nb})^{ij} / 2n_{ij} \quad (26)$$

And where

$$nii = ni(ni-1)/2 \quad (27)$$

is the number of contacts between n_i particles of type i,

$$nij = ni\ nj/\ 2 \quad (28)$$

is the number of contacts between n_i particles of type i and n_j particles of type j. Since the mixed energy terms in eq 25 and 26 and the number of contacts in eq. 28 are the same, the expression for the total system energy in eq 24, becomes

$$E_{system} == n_{ii}E_{ii} + n_{jj}E_{jj} + n_{ij}E_{ij} + 2\ n_{ji}E_{ji} \quad (29)$$

The values of self-interaction energies (E_{ii} and E_{jj}) are easily obtainable dividing the corresponding values reported before by the appropriated number of contacts, while the value of the system total energy (E_{system}) is straightforward derived from the MD simulation. Accordingly, the remaining mixed energy term, E_{ji}, is then obtained applying the previous equation. All the rescaled DPD energies are computed below.

E_{ss}= 0(kcal/mol)

E_{pp}= 154,6/ 15 = 10,3(kcal/mol)
n_{pp}= 6(6-1)/2= 15

E_{ww}= -47759,74/ 142311 = - 0,33(kcal/mol)
n_{ww}= 534(534-1)/2= 142311

E_{pw}= -47822,73 /3204= -15 kcal/mol
n_{pw}= 6x 534/ 2 = 1602

E_{ps}= 140,46 /3240= 0.04 kcal/mol
n_{ps}= 6x 540/ 2 = 1620

E_{sw}= -48561,12 /288360= -0,17kcal/mol
n_{sw}= 540x 534/ 2 = 144180

a_{ww}= 25
a_{pw}= 20

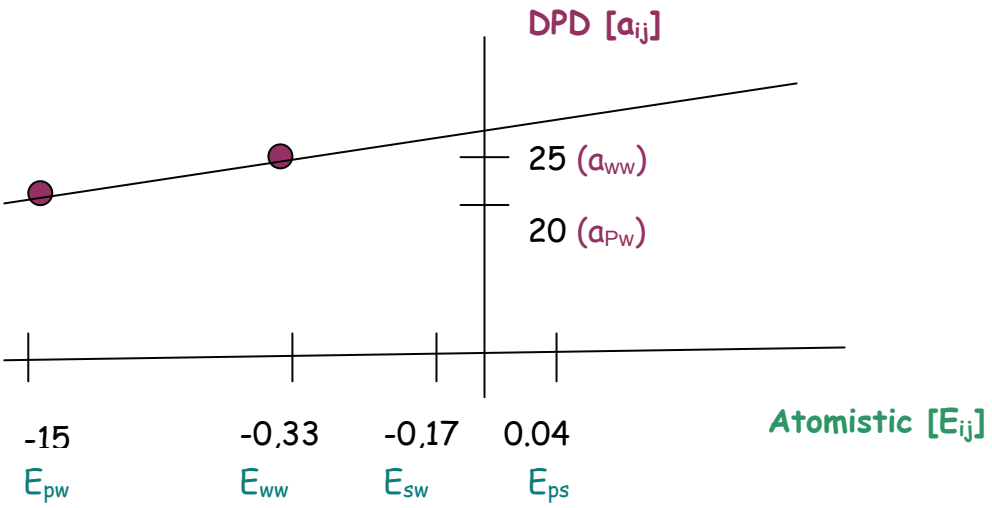

Figure 11: Sketch of method used to bridge atomistic simulation and DPD system

The bead-bead interaction parameter for water-water interaction was set equal to a_{ww}= 25 in agreement with the correct value for a density value of ρ = 3. The value of the Peg-water interaction (i.e., a_{pw}= 20) was decreased to describe both qualitatively and quantitatively the effect of water-Peg interactions as computed from MD smulation. Having fixed these two parameters, their values were then associated with the corresponding values of the DPD energies rescaled from MD simulations. Thus, a_{ww} = 25 corresponds to a DPD rescaled energy value of -0.33, while an energy value of -15 is mapped to a_{pw}= 20.

All of the remaining DPD interaction parameters (a_{ij}) can then easily be derived following this criterion as is shown in graph 11. In the case of Peg-Peg interaction, since we found a positive value in the MD interaction energies evaluation, we set a_{pp}= 28. Finally, for the pair p-s, the parameter a_{ij} was calculated using the scaling law, and set to a value of 26, because of its quite neutral value of rescaled energy. The final set of DPD parameters, obtained from the scaling procedure starting from atomistic MD simulation energies, is reported in the table below:

a_{ij}	W	P	S	Wall
W	25	20	80	300
P	20	28	26	300
S	80	26	3	5

Table 1: a_{ij} parameters used for DPD simulation

We made use of the option available in the DPD commercial software of including a smooth wall in the simulation box perpendicular to the *z*-axis at the origin. A solid flat wall in DPD is usually constructed as an ensemble of locally freezing DPD particles[22]. The frozen particles behave as normal fluid particles but maintain a fixed position and velocity. Therefore, the wall interacts with each bead in the system with a potential of the same form as the bead-bead conservative force. This force is soft and short-ranged, so beads are not strictly forbidden from passing through the barrier. In order to construct the channel surfaces, the (S) beads must have the aij parameters represented in table 1. The values for the interaction with the wall used in the simulations are reported in the last column of the table1.

Snapshots from DPD simulation are shown in figure 12 and 13.

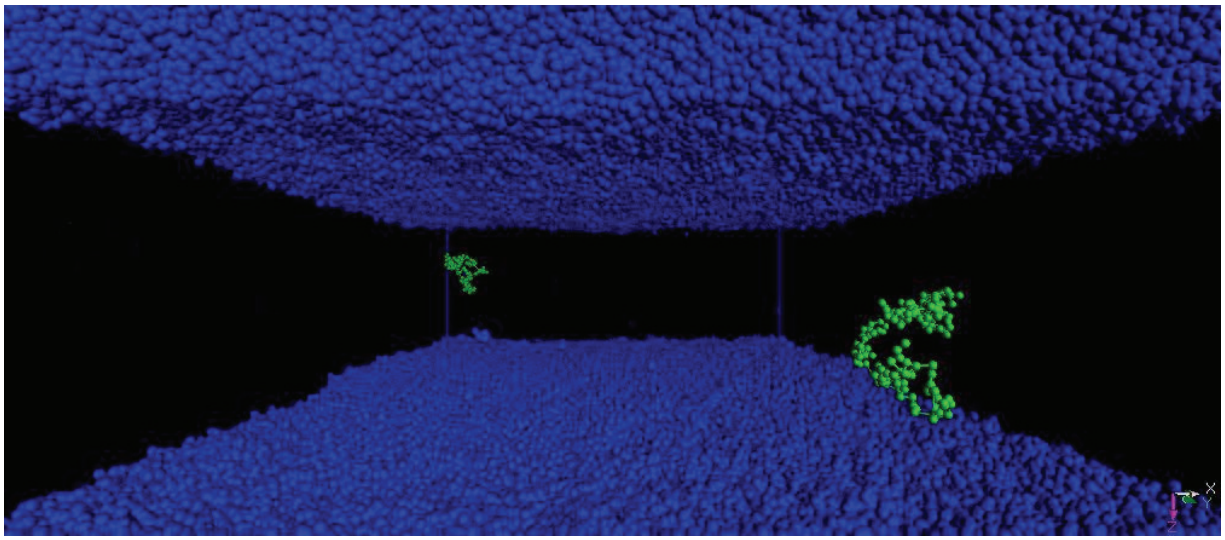

Figure 12: Snapshot A of a DPD simulation of PEG 20kDa in a glass nanoslit of 30 nm height. Blue beads are glass surfaces, green beads are PEG molecules, water is not represented.

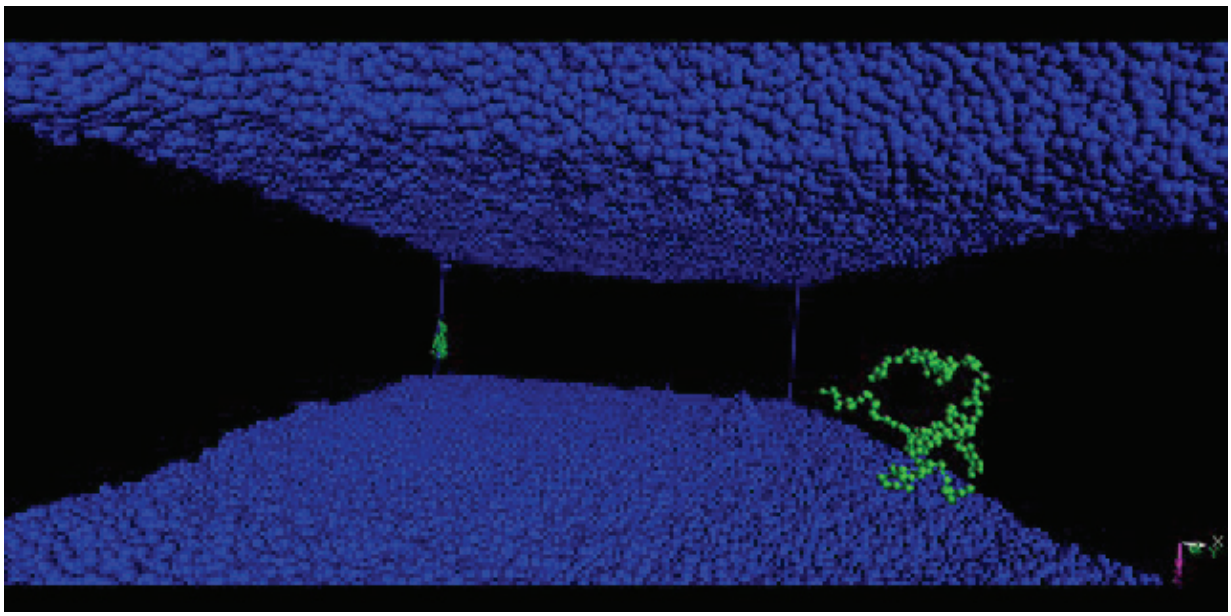

Figure 13: Snapshot B of a DPD simulation of PEG 20kDa in a glass nanoslit of 30 nm height. Blue beads are glass surfaces, green beads are PEG molecules, water is not represented.

As we can see from the snapshot showed, there is good agreement between the atomistic model built and the system morphology in DPD. From the built system we then collected molecular transport parameters on this nano-level. In fact we considered Peg beads motion across x, y and z direction and evaluated any differences caused by morphological anisotropy to be related to channel narrow dimensions.

Conclusions

In this work we developed a Dissipative Particle Dynamics simulation of macromolecules in nanochannels. In particular we modeled PEG molecules of 20kDa in channels of 30 nm height. Once validated our tool could be used for the development of a mesoscale model to predict molecular motion in nanochannels. This model could be advantageous for engineering applications of nanodevices as drug delivery systems.

References

1. Karniadakis G., Ali Beskok, Narayan Aluru, "*Microflows and Nanoflows Fundamentals and Simulation*" Interdisciplinary Applied Mathematics, **29** Editors S.S. Antman J.E. Marsden L. Sirovich, Springer
2. Travis and Gubbins, 2000; Travis, K. P. and Gubbins, K. E. "Poiseuille flow of Lennard-Jones fluids in narrow slit pores" *Journal of Chemical Physics*, **112** (4):1984–1994. (2000).
3. Magda, J. J., Tirrell, M., and Davis, H. T. "Molecular dynamics of narrow, liquid-filled pores". *Journal of Chemical Physics*., **83** (4):1888–1901. (1985).
4. Mao, Z. and Sinnott, S. B. "A computational study of molecular diffusion and dynamic flow through carbon nanotubes". *Journal of Chemical Physics*. B, **104** (19):4618–4624. (2000).
5. Martì, J., Guardia, E., and Gordillo, M. C. "Reorientational motions in sub- and supercritical water under extreme confinement". *Chemical Physics Lett*ers., **365**:536–541. (2002).
6. Mashl, R. J., Joseph, S., Aluru, N. R., and Jakobsson, E. "Anomalously immobilized water: a new water phase induced by confinement in nanotubes" *Nano Letters*., **3**:589–592 (2003).
7. Hoogerbrugge, P. J., Koelman J. M. A., ‘‘Simulating Microscopic Hydrodynamic Phenomena with Dissipative Particle Dynamics" *, Europhysics. Letterrs.* ***19*****,** 155, (1992)
8. Fermeglia M, S Pricl, "Multiscale modeling for polymer systems of industrial interest "*Progress in Organic Coatings* **58** 187–199, (2007)
9. Espanol, P.m and Warren, P "Statistical mechanics of dissipative particle dynamics". *Europhysics. Letters* **30**,191 (1995)
10. Groot, R. D.; Warren, P. B." Dissipative particle dynamics: Bridging the gap between atomistic and mesoscopic simulation" *Journal of Chemical Physics.*, **107**, 4423, (1997)
11. Koelman, J. M. A., and Hoogerbrugge, P. J., ‘‘Dynamic simulations of hard sphere suspensions under steady shear" *Europhysics. Letters.* **21**, 363, (1993)
12. Jianhua Huang, Yongmei Wang, Mohamed Laradji, "Hydrodynamic interaction in polymer solutions simulated with dissipative particle dynamics" *Macromolecules* **39**,5546-5554 (2006)

13. Maiti, A.; McGrother, “Bead–bead interaction parameters in dissipative particle dynamics: Relation to bead-size, solubility parameter, and surface tension” *Journal of Chemical Physics.*, **120**, 1594, (2004)
14. Ortiz, V.,Nielsen, S. O., Discher D. E., Klein M. L., Lipowsky R., Shiloocock J., “Dissipative Particle Dynamics Simulations of Polymerosomes”, *Journal of Physical Chemistry B,* **109**, 17708-17714, 2005
15. Sun, H. “COMPASS: An ab Initio Force-Field Optimized for Condensed-Phase Applications – Overview with Details on Alkane and Benzene Compound” *Journal of Physical Chemistry B **102***, 7338. (1998)
16. Scocchi G. Posocco P., Fermeglia M., Pricl S., “Polymer-Clay Nanocomposites: A Multiscale Molecular Modeling Approach”, *Journal of Physical Chemistry B,* **5:1**, 1-9, 2007
17. Theodorou, D. N.; Suter, U. W. ”Detailed molecular structure of a vinyl polymer glass” *Macromolecules* **18,** 1467 (1985)
18. Li, Y.; Goddard, W. A., III. “Nylon 6 Crystal Structures, Folds, and Lamellae from Theory” *Macromolecules* **35**, 8440. (2002)
19. Ewald, P. P ‘‘Evaluation of optical and electrostatic lattice potentials”. *Ann. Phys.*, **64,** 253. 1921
20. Nose´, S. *Prog. Theor. Phys. Suppl.*, **103**, 1. 1991
21. Connolly, M.,“Computation of molecular volume”. L. *Journal American. Chemical. Society.* **107,** 1118, 1985
22. Visser, D. C.; Hoefsloot, H. C. J.; Iedema, P. D. “Comprehensive boundary method for solid walls in dissipative particle dynamics” *Journal of Computational Physics.* **205**, 626. (2005),

Summary and outlook

Nanomaterials are receiving an increasing scientific and technological interest recently. The presence of pores or channels on the nanomentric range allows a diverse interaction between molecules and material walls which has been demonstrated to have interesting features. In fact, whenever the size of the device approaches molecule's dimensions, generally a deviation from all classic relationships occurs. In particular transport properties of molecules, in terms of diffusivity, are affected by confinement. Fick's laws for diffusion were demonstrated to fail in many experimental cases. Among other applications, nanomaterials employed in the drug delivery gave interesting release kinetics (zero order release).

Which is the reason why such a deviation might occur has not been clarified yet. Of course if a molecule is confined in a molecular small 3D cage its mean square displacement can be as high as the cage dimension. Therefore interesting is to investigate how and why 1D or 2D confinements induce deviations from Brownian motion.

Moreover, being concerned about the application of nanomaterials to the development of drug delivery devices, it is of fundamental importance the understanding of how the nanostructure might change drug molecule diffusion properties within the device.

In this thesis work we addressed this topic and investigated how confinement may affect molecular diffusion properties. We developed our work starting from macroscopic permeability observations of hindered diffusion in nanoporous silicon membranes. The release of biomolecules from nanoporous membranes resulted deeply affected by material microstructure parameters. Hindered diffusion was shown for Dextran 10kDa with a decrease of about four orders of magnitude in the effective diffusion coefficient.

To overcome the limit of macroscopic measurements we diverged our experimental efforts to the investigation of single molecule behavior under confinement. As a single molecule analysis we performed Fluorescence Correlation Spectroscopy (FCS), a well established technique which measures fluorescence intensity fluctuations due to Brownian motion of few fluorochrome molecules in an illuminated volume smaller then a femtonliter. We performed FCS measurements of molecular motion in solid confined geometries of glass nanoslits as small as 10 nm in height. Both small molecules such as Rhodamine6G and high molecular weight molecules such as Dextrans 40 and 70 kDa and Peg 20 kDa

were employed in order to investigate at a single molecule level the influence of size, chemistry and flexibility on confined diffusion. From our results Rhodamine 6G seemed to be quite unaffected from confinement whereas all macromolecules showed a reduction of their diffusion coefficient of almost one order of magnitude with an anomaly parameter approaching, in the case of strong confinement (d/h >1), the single–file limit of 0.5. In particularly Dextran molecules of 70kDa showed no motion in the strong confinement case of d/h = 1.8. More experimental work is needed to develop a complete scenario.

Starting from single molecule observations we also wanted to develop a mesoscopic dynamic model using Dissipative Particle Dynamics (DPD).

Our study provides new experimental data for future improvement of theoretical models of diffusion in confined geometries. The molecular model once validated could be used to predict the macroscopic behavior in terms of physically meaningful parameters that represent the actual dynamics of the system at a nanoscopic level, becoming a meaningful tool to the design of nanodevices for drug delivery applications.

Acknowledgements

I would like to thank first of all my professor Paolo A. Netti, for introducing me to this challenging thesis project.

Then I would like to list all the people who helped me achieving this task in the last three years, each one of them was indispensable. First people in ENEA, starting with dr. Vera La Ferrara whose optimism was fundamental during the very first steps of this project. Then I would like to acknowledge the very nice head of department dr. Girolamo Di Francia, Ivana Nasti for introducing me to the photolithographic techniques, eng. Brigida Alifano for helping with the FIB fabrication and for her friendship.

All the people in my lab at DIMP and especially I would like to thank dr. Filippo Causa for three years of advices. I would like to thank dr. Giuseppe Scherillo for his nice way of asking news and giving help. Then I would like to thank the smiling friendship of eng. Davide Della Volpe, and of dr. Maurizio Ventre who shared some knowledge about English tea and could give very useful advices. Then I would like to thank dr. Angela Guaccio for telling me the very first few words about FCS and for her advices and dr. Vincenzo Guarino for some important tips about doing research. I also have to acknowledge dr. Maria Silvia Panemi for the DPD simulation work and dr. Gigi Sanguigno for the mathematical development of the autocorrelation model and for the many useful discussions until 8.30 pm outside the university.

Then I would like to thank myself for reading on the ConfCorII software the tense ”…developed in collaboration with EMBL Heidelberg..” that made me search and find on the website the special and unique occasion to visit an enthusiastic place where I could enhance my educational and research experience. dr. Rainer Pepperkok must be acknowledged for having accepted my application in EMBL as a visiting student and for introducing me to dr. Malte Wachsmuth and to all the very friendly people in ALMF (Yury, Stefen, Arne) and in his lab (Fatima, Enrica, Carolina, Christian, Simone). I am pleased to acknowledge dr. Malte Wachsmuth in particular for his “Fluctuation Analyser” software. I am very grateful to him for his assistance during my EMBL visiting time. I received a constant guidance from him especially with FCS, autocorrelation analysis and fitting procedures. I would like to thank him for his helpful suggestions, for his friendship and for showing me the Line Scan FCS in DKFZ Heidelberg.

I would like to offer my great thanks to the people in Heidelberg who hosted me and allowed me to spend there more time than I thought: dr. Enrica San Pietro, dr. Alvar Trucco and their amazing dog Kate that used to sit out of my door. Then thanks goes to dr. Daniela Leiti Fabrino, a Brazilian smiling girl who shared her 30 sqm flat with me for two weeks. And then dr. Giovanna Benvenuto for helping me in a difficult situation and for her nice advices.

I offer my thanks to my parents for being always there and my father especially for giving me rides to the university when my cruciate ligament broke. I need to thank my friends and especially Viviana, Simona and Carmelita, because I know they are always there if I need them. I also have to thank my boyfriend Ivano for being patient with me, for his helpful advices and for his care.